

Construction of a low temperature STM and studies of large molecular systems

THIS IS A TEMPORARY TITLE PAGE
It will be replaced for the final print by a version
provided by the service academique.

Thèse n. 6820 2015
présenté le 25 Setembre 2015
à la Faculté des Sciences de Base
laboratoire de sciences à l'échelle nanométrique
programme doctoral en Physique
École Polytechnique Fédérale de Lausanne
pour l'obtention du grade de Docteur ès Sciences
par

Daniel Pablo Rosenblatt



acceptée sur proposition du jury:

Prof. H. N. Ronnow, président du jury
Prof. Klaus Kern, directeur de thèse
Prof. Steven De Feyter, rapporteur
Dr S. Stepanow, rapporteur
Prof. Hugo Dil, rapporteur

Lausanne, EPFL, 2015

"Most people would sooner die than think;
in fact, they do so."
— Bertrand Russell

A mis abuelos,
Samuel y Victoria,
Fanny y Alberto,
Armond y Anne,
con mucho cariño.

Acknowledgements

First and foremost, I would like to thank my thesis director, *Prof. Klaus Kern*, for the opportunity to carry out my research in his labs with the fine group of people he had assembled.

Next I want to thank my supervisor, *Dr. Uta Schlickum*, for her guidance, her trust and the freedom she gave me in the construction and the research. I thank *Dr. Bogdana Borca* for her excellent introduction to STM. I was fortunate that *Sebastian Koslowski* joined me in our subgroup and got caught up in our enthusiasm with the possibilities our experiment offers.

Dr. Markus Etzkorn deserves a special thanks for dedicating his time and experience starting from the construction of the STM through to the scientific projects. He knows to give the right answers when they are due and ask the right questions when they are due.

I was also lucky to collaborate with *Dr. Stephan Rauschenbach* and *Sabine Abb* who naturally became good friends. ES-IBD depositions are much more entraining in their presence, and I got to meet several talented people thanks to the frequent turnover in the ES-IBD lab.

I would also like to thank many more colleagues with whom scientific conversation is always stimulating: *Dr. Markus Ternes*, *Dr. Klaus Kuhnke*, *Dr. Christian Schön*, *Dr. Christian Ast*, *Dr. Peter Wahl*, *Dr. Rico Gurtzer*, *Dr. Kannan Balasubramanian*, *Dr. Hanj Benia*, *Dr. Peter Jacobson* and *Dr. Pablo Merino*.

The construction of the STM would not have been possible without the expert craftsmanship of *Wolfgang Stiepany*, *Peter Andler*, *Marko Memmler* and *Andreas Koch*. I learned the secrets of making an STM head from *Dr. Maximilian Assig*, and myriads of details regarding vacuum, low temperatures, cabling and climbing from *Dr. Eike Oliver Schäfer-Nolte*. The success of the construction relied also on the quality and precision of parts made by the *mechanical workshop* and the *fine mechanical workshop*. An additional acknowledgement is due for *Dr. Christian Ast* for designing a superb STM head.

I owe a great deal of my time in Stuttgart to two wonderful women, *Frau Sabine Birtel* and *Frau Birgit King*, for their efficient and professional handling of schedules and paperwork. Sabine orchestrates our department like a true maestra, while Birgit shields us foreigners from

Acknowledgements

the burden of German bureaucracy.

I thank my former office mates. *Dr. Ivan Pentegov* was my translator and helped me with my first steps in Germany. *Dr. Vivek Pachauri* introduced me to the fascinating Indian subcontinent. *Roberto Urcuyo* taught me everything about football and helped me keep the rust off of my native language.

To my family, who helped me become who I am, you are with me in spirit wherever I go.

More than anyone, I thank *Dr. Judit Guasch* for teaching me chemistry, for her love and support all through this time, and for her constant sunshine.

Stuttgart, August 14, 2015

Daniel Pablo Rosenblatt

Abstract

Several aspects in the exciting field of molecular self assembly are addressed in this thesis. Thanks to the scanning tunnelling microscope (STM), structural, electronic and magnetic properties on surfaces can be studied down to the size of a single atom. In the scope of this thesis I designed and built a STM operating in ultra high vacuum (UHV) and at liquid helium temperature. In Chapter 2 I highlight the design and key features of this system. In particular, I describe the development of ultra high frequency (UHF) cabling under severe design constraints, intended to be used for a state of the art STM time resolved measurement technique [1]. The stability and performance of the instrument are demonstrated by a few benchmark measurements. In addition, the use of an UHV suitcase is described, a tool necessary in order to transfer samples between UHV chambers in the without exposing them to the ambient air.

The arrangement of molecules on surfaces is sensitive to intermolecular interactions, but also to molecule-surface interactions. The surfaces used as support for molecules must therefore be fully characterized and understood from the structural, chemical and electronic points of view. Thanks to the exquisite resolution of STM, the structure and electronic properties of hexagonal boron nitride on a rhodium crystal (h-BN/Rh(111)) are thoroughly investigated. In the experiments described in Chapter 3, work function (WF) variations that occur at the nanometric scale on this layer are investigated. These variations are the key to understanding the arrangement of molecules on this surface [2], yet the magnitude of this variation is disputed [2, 3]. STM offers two ways of measuring the local WF and the two are compared with an additional experiment performed using an atomic force microscope (AFM). The results show how challenging it is to obtain quantitatively accurate results of WF variations at such a small scale. They also provide rich insight about hot electronic states near surfaces called image potential states (IPS), whose lifetimes on nanostructured surfaces has so far received little attention. Furthermore, a new phase of h-BN on rhodium was discovered and a preliminary characterization and assessment of its origin are presented.

STM can provide valuable information for understanding the arrangement as well as the electrical properties of molecules on surfaces. These capabilities are harnessed in Chapter 4 to study large molecules on metallic surfaces, and on thin dielectric surfaces supported by metals. Angiotensin-II (At-II) is a peptide, comprising 8 amino acids, small enough to fit in the nanometric cavities of h-BN/Rh(111). This peptide can be brought to the surface

Acknowledgements

intact and free of solvent thanks to recent advances in electrospray ion-beam deposition (ES-IBD) [4]. On a Cu surface, we observe that the peptides interact strongly with the substrate, and this interaction has a strong influence on their complex arrangements and electronic properties. However, on a single layered sheet of h-BN/Rh(111), the peptides are sufficiently decoupled from the metallic substrate, and their electronic properties are conserved. In a series of preliminary measurements, these electronic properties are studied towards the goal of discriminating between the amino acids the peptide is made of. Additional strategies that may enable peptide sequencing using STM are discussed.

Turning our gaze onto larger molecules, cytochrome-C (CytC) is a protein made of 104 amino acids. On plain metal surfaces, its size and flexibility make the number of conformations available to it enormous [5]. In Chapter 5 this protein is deposited on a nanopatterned surface, forcing the protein to adhere to a square grid with a period of $5nm$. This makes the number of possible conformations manageable. A detailed look at these conformations reveals many details about how the proteins move on the surface and find their place on the grid. For example, it can be inferred that short segments of the protein can diffuse on the surface at room temperature while longer segments are immobilized. The critical length where diffusion begins is used to estimate the diffusion barrier energy. Furthermore, a simplified simulation of the landing process yields a surprisingly good fit to the experimentally observed conformation distribution. This fit confirms several assumptions built-in to the simulation, such as the flexibility of the protein and the negligible role of the identities of the amino acid side chains.

Key words: STM, STS, biomolecules, protein, peptide, h-BN, IPS, FER, self assembly.

Résumé

Cette thèse adresse plusieurs aspects passionnants dans le domaine de l'auto-assemblage moléculaire. Grâce à la microscopie à effet tunnel (STM), les propriétés structurales, électroniques et magnétiques sur des surfaces peuvent être étudiées à l'échelle d'un seul atome. Dans le cadre de cette thèse, j'ai conçu et construit un STM qui fonctionne dans l'ultra vide (UHV) et à la température de l'hélium liquide. Au premier chapitre, je présente la conception et les principales caractéristiques du système. En outre, je décris la conception de câbles pour les très hautes fréquences (UHF) soumis à de sévères contraintes. Ces câbles permettront d'obtenir une résolution temporelle de quelques nanosecondes qui sera achevée grâce à une technique de pointe récemment développée [1]. La stabilité et la performance de l'instrument sont mises en évidence par des mesures tests. L'utilisation d'une valise UHV est aussi décrite. Cet outil est nécessaire pour transférer des échantillons entre des chambres à vide sans les exposer à l'atmosphère.

L'arrangement des molécules sur les surfaces est sensible aux interactions intermoléculaires ainsi qu'aux interactions entre molécules et la surface. Les surfaces utilisées comme support pour les molécules doivent donc être complètement caractérisées et connues du point de vue structurale, électronique et chimique. Grâce à la très haute résolution du STM, la structure et les propriétés électroniques d'une couche de nitrure de bore hexagonal sur un cristal de rhodium (h-BN/Rh (111)) sont analysées avec précision. Dans les expériences décrites au 3ème chapitre, les variations du travail de sortie qui se produisent à l'échelle nanométrique sur cette couche, sont étudiées. Ces variations sont la clé pour comprendre l'arrangement des molécules sur cette surface [2], et l'ampleur de cette variation est encore contestée [2, 3]. Le STM offre deux façons de mesurer le travail de sortie local. Ces deux façons sont comparées entre elles et avec une méthode supplémentaire effectuée utilisant un microscope à force atomique. Les résultats mettent en évidence la difficulté d'obtenir des données précises sur les variations du travail de sortie à une échelle si petite. Ils fournissent également un aperçu sur des états électroniques à proximité de surfaces connus sous le nom "d'états de potentiel image" (IPS), dont la durée de vie sur les surfaces nanostructurées a jusqu'à présent reçu peu d'attention. En outre, une nouvelle phase de h-BN/Rh(111) a été découverte, et une première caractérisation et évaluation de son origine sont présentées.

Le STM peut fournir des informations précieuses pour la compréhension de l'arrangement des molécules sur les surfaces ainsi que sur leurs propriétés électroniques. Ces capacités sont

Acknowledgements

exploitées dans le 4ème chapitre pour étudier de grandes molécules sur une surface métallique ainsi que sur une couche diélectrique mince supportée par un métal. L'angiotensine-II (AT-II) est une peptide, comprenant 8 acides aminés, suffisamment petite pour se loger dans les cavités nanométriques du h-BN/Rh(111). Cette peptide peut être ramenée à la surface intacte et exempte de solvants grâce au progrès récent du dépôt par faisceau d'ions générées par électrospray (ES-IBD) [4]. Sur une surface de Cu, on observe que les peptides interagissent fortement avec le substrat, et cette interaction a une influence importante sur leurs arrangements et sur leurs propriétés électroniques. Cependant, sur une seule couche de h-BN/Rh(111), les peptides sont suffisamment découplées du substrat métallique, et leurs propriétés électroniques sont conservées. Lors d'une série d'expériences préliminaires, ces propriétés électroniques ont été étudiées avec l'objectif de pouvoir différencier les acides aminés composant la peptide. D'autres expériences sont aussi mentionnées qui pourraient permettre de faire la différenciation entre les acides aminés d'une peptide.

En ce qui concerne les grandes molécules, l'assemblage est en général plus compliqué. La Cytochrome-C (CytC) est une protéine composée de 104 acides aminés. Sur des surfaces métalliques, elle peut adopter une variété importante de conformations grâce à sa taille et sa flexibilité [5]. Dans le 5ème chapitre, cette protéine est déposée sur une surface nanostructurée, où les protéines sont obligées de s'arranger sur un réseau carré avec une périodicité de 5 nm. Cela réduit le nombre possible de conformations que les protéines peuvent adopter à un niveau permettant de les étudier individuellement. Des observations détaillées de ces conformations révèlent des détails sur la façon dont les protéines se déplacent sur la surface et trouvent leur place sur le réseau. Par exemple, il est observé que des segments courts de la protéine peuvent diffuser sur la surface pendant que des segments plus longs sont immobilisés. La longueur minimale pour laquelle cette diffusion est possible informe sur la barrière énergétique de diffusion. Une simulation simplifiée du dépôt des protéines sur la surface permet de distinguer les propriétés et les processus pertinents pour comprendre ce phénomène. La simulation réussit à reproduire les résultats expérimentaux, et démontre la flexibilité des protéines et le rôle négligeable que jouent les groupes chimiques des acides aminés.

Mots clefs : STM, STS, biomolécules, protéine, peptide, h-BN, IPS, FER, auto-assemblage.

Contents

| | |
|--|------------|
| Acknowledgements | v |
| Abstract | vii |
| Résumé | ix |
| List of figures | xii |
| List of abbreviations | xv |
| Introduction | 1 |
| 1 Theoretical and Experimental methods | 5 |
| 1.1 Quantum tunnelling | 5 |
| 1.2 Scanning Tunneling Microscopy | 6 |
| 1.3 Tunneling spectroscopy | 7 |
| 1.4 Nanosecond pump-probe experiments with STM | 9 |
| 1.5 Electrospray ion beam deposition | 10 |
| 2 Construction of the STM | 13 |
| 2.1 STM head and STM chamber | 14 |
| 2.2 Preparation chamber and remaining components | 18 |
| 2.3 UHF cabling | 21 |
| 3 Local work function variations of hexagonal boron nitride on metal surfaces | 25 |
| 3.1 Local work function measurement using STM and AFM | 25 |
| 3.2 Electronic properties of hexagonal boron nitride on metal surfaces | 32 |
| 3.3 Local work function variations on h-BN/Rh(111) | 34 |
| 3.4 Effect of lateral localization on FER lifetimes | 52 |
| 3.5 New phase of h-BN/Rh(111) | 56 |
| 4 Towards protein sequencing using STM | 63 |
| 4.1 Angiotensin-II on Cu(111) | 64 |
| 4.2 Angiotensin-II on h-BN | 68 |
| 4.3 Outlook | 71 |
| | xi |

Contents

| | | |
|----------|--|------------|
| 5 | Directed self-assembly of proteins on patterned substrates | 73 |
| 5.1 | Introduction | 73 |
| 5.2 | Experimental procedure and initial observations | 76 |
| 5.3 | Analysis of conformation distribution and discussion | 78 |
| 6 | Summary and Outlook | 91 |
| 6.1 | Prospects for the STM | 91 |
| 6.2 | Local WF variation measurements on h-BN/Rh(111) | 92 |
| 6.3 | Peptide sequencing | 93 |
| 6.4 | Modeling the adsorption of large molecules on nanostructures | 94 |
| | Bibliography | 113 |
| | Curriculum Vitae | 115 |

List of Figures

| | | |
|------|--|----|
| 1.1 | Illustration of quantum tunnelling. | 5 |
| 1.2 | Principle of STM operation. | 7 |
| 1.3 | Electron tunnelling spectroscopy. | 8 |
| 1.4 | STM pump probe experiments | 10 |
| 1.5 | ES-IBD | 11 |
| 2.1 | Chamber outline | 13 |
| 2.2 | STM head | 14 |
| 2.3 | Sample holder | 16 |
| 2.4 | STM performance | 17 |
| 2.5 | Radiation shields and laser path | 18 |
| 2.6 | Vacuum system | 20 |
| 2.7 | SMA connector | 23 |
| 2.8 | Performance of UHF transmission line | 24 |
| 3.1 | Work function variation of Ag/Pt(111) | 27 |
| 3.2 | Illustration of IPS | 29 |
| 3.3 | h-BN/Rh(111) | 33 |
| 3.4 | Local WF map using approach curves | 35 |
| 3.5 | Diagonal tunnelling calculation | 37 |
| 3.6 | Anomalies in approach curve WF maps | 39 |
| 3.7 | dz/dV maps | 40 |
| 3.8 | Eigenstates of a free electron in a circular 2D potential well | 42 |
| 3.9 | Local WF map using FERs | 44 |
| 3.10 | Analysis of FER maps | 45 |
| 3.11 | Analysis of FER peak maps | 47 |
| 3.12 | Local CPD map using KPFM | 49 |
| 3.13 | Analysis of local FER peaks | 53 |
| 3.14 | FERs on h-BN/Cu(111) | 55 |
| 3.15 | Effect of surface dipoles on IPS position | 56 |
| 3.16 | h-BN/Rh(111) images with different tips and SW phase | 57 |
| 3.17 | Atomic resolution images of the SW phase | 58 |
| 3.18 | Spectroscopy on the SW phase | 59 |

List of Figures

| | | |
|-----|---|----|
| 4.1 | Molecular structure of At-II | 64 |
| 4.2 | At-II/Cu(111) overview | 65 |
| 4.3 | Conformations of At-II on Cu(111) after annealing | 67 |
| 4.4 | STM measurements of At-II with functionalized tips | 68 |
| 4.5 | dI/dV measurements on an At-II dimer on Cu(111) | 69 |
| 4.6 | STM measurements of At-II/h-BN/Rh(111) | 70 |
| 4.7 | Spectroscopic measurements of At-II/h-BN/Rh(111) | 71 |
| 4.8 | STM and STS of pentacene on h-BN/Rh(111) | 72 |
| 5.1 | Cytochrome-C | 74 |
| 5.2 | Copper nitride film on Cu(100) | 75 |
| 5.3 | Appearance of a single CytC protein on Cu ₂ N | 77 |
| 5.4 | Diffusion of CytC proteins on Cu ₂ N | 78 |
| 5.5 | Observed distribution of conformations of CytC on Cu ₂ N and curling length. | 79 |
| 5.6 | CytC conformational distribution: observation vs. simulation. | 83 |
| 5.7 | Histograms of values of Δ | 84 |
| 5.8 | Pre-patterning by image charges. | 89 |

List of abbreviations

| | |
|--------|---|
| 2PPE | 2-photon photoemission |
| ACE | Angiotensin-converting enzyme |
| AFM | Atomic force microscope |
| At-II | Angiotensin-II |
| CPD | Contact potential difference |
| CVD | Chemical vapour deposition |
| CytC | Cytochrome-C |
| DFT | Density functional theory |
| E_F | Fermi level |
| ES-IBD | Electrospray ion-beam deposition |
| FER | Field emission resonance |
| FWHM | Full width at half maximum |
| HOMO | Highest occupied molecular orbital |
| IETS | Inelastic electron tunneling spectroscopy |
| IPS | Image potential state |
| KPFM | Kelvin probe force microscopy |
| LDOS | Local density of states |
| LUMO | Lowest unoccupied molecular orbital |
| MBE | Molecular beam epitaxy |
| ML | Monolayer |
| MOF | Metal organic framework |
| MS | Mass spectrometer |
| NEG | Non evaporable getter |
| PLD | Pulsed laser deposition |
| PTFE | Polytetrafluoroethylene |
| PVBA | 4-[trans-2-(pyrid-4-yl-vinyl)] benzoic acid |
| SEM | Scanning electron microscope |
| SMA | Sub-miniature type A (connector) |
| SPM | Scanning probe microscope |
| SR | Semi-rigid (cable) |
| STM | Scanning tunneling microscope |
| STS | Scanning tunneling spectroscopy |
| SW | Spoked wheel |

List of Figures

| | |
|-----|---|
| TEM | Transmission electron microscope |
| UHF | Ultra high frequency |
| UHV | Ultra high vacuum |
| WF | Work function |
| WKB | Wentzel–Kramers–Brillouin (approximation) |

Introduction

The potential benefits of controlling the organization of matter at the nanometre scale have recently gained wide acceptance [6]. By tuning the composition and structure of materials on this scale, materials can be engineered with combinations of optical, chemical, electronic and magnetic properties which cannot be found in any naturally occurring material. An example that seems to be taken out of a science fiction movie, is the ability to cloak an object by enclosing it in a shell made of a metamaterial with an accurately tuned dielectric constant [7]. Fine control of magnetic properties could not only reduce the size of magnetic data bits [8], but might make reality the "magnetic racetrack memory" [9], which would revolutionize the density, speed and efficiency of information storage.

Photolithography is currently the most widespread technology for structuring matter on the nanoscale. It consists of selectively removing/adding material in a pattern defined by a mask. Photolithography can produce millions of features within a single exposure [10], but its resolution is limited by Abbe diffraction to half the wavelength of the radiation used [11]. This makes it unpractical for sub nanometre sized features, where the use of x-ray radiation introduces formidable challenges [11]. Electron beam lithography can reach extremely high resolution [12], but is a serial process, not suitable for mass production [13]. Self assembly is both a parallel process and can achieve sub nanometre resolution [14]. It relies on the organization of pre-existing building blocks into ordered structures through local interactions between the components, with little external direction. Here the challenge shifts to the design of the building blocks and the conditions under which the desired structures will emerge [6]. This requires an excellent acquaintance with the building blocks in terms of their structure, their properties and the interactions between them and their environment.

For example, cavities with tunable sizes, shapes and functionality can be generated in metal organic frameworks (MOFs) [15], structures which are self-assembled by mixing organic linker molecules with metallic cations. These engineered cavities can then be used for gas storage or separation, drug storage and delivery or even for catalysis [16]. A larger range of structures can be achieved by varying the composition and solution concentration of amphiphilic block copolymers [17, 18], including spheres, cylinders, giroids and lamellae. Fibres derived from peptide-amphiphiles have been found to reproduce key properties of the human extracellular matrix, with a significant impact on regenerative medicine [19]. Block copolymers can also be used to control the formation of other materials, such as nanoparticles with tunable sizes

and arrangements in what is called "block copolymer micellar lithography" [20, 21]. Virtually any shape and pattern can be generated by folding strands of DNA. In a technique called DNA origami [22], a single strand of DNA is folded into an arbitrary shape, aided by hundreds of shorter DNA strands used as "staple strands". The most exciting achievements in self assembly are, however, those who bring us closer to molecular size machines, such as artificial muscles [23] and nano-sized motors [24].

2D interfaces provide a tunable platform for supramolecular engineering and self assembly [25, 26]. The same principles and interactions which dominate self assembly in solution are at play here as well, albeit with reduced dimensionality and with the added support, reactivity and periodicity of the substrate. The latter provide additional degrees of control in order to tune the organization of adsorbates [27]. A strong effort has been dedicated to the introduction of tunable porosity to surfaces [28], where it was found that the combination of organic linkers with metallic coordination centres yields highly porous, 2D, metal-organic surface networks [29]. The pores represent suitable trapping sites where molecular species can be trapped and further processes can occur [30]. The mixing of organic species with metallic atoms not only stabilizes interesting and desirable surface network morphologies [31], but the close proximity of these metallic atoms leads to additional new and interesting magnetic [32] and catalytic [33] properties. 2D self assembly thus introduces an additional degree of control, but this comes with an additional player in the game, whose properties and interactions must be as well understood as those of the building blocks.

Organic chemists can produce nearly any combination of atoms for use in self assembly, with very few exceptions [34]. The time and cost required for synthesizing a new molecule vary, however, wildly [35]. Molecules which are not on the catalogue of a chemical company may turn out to be prohibitively expensive to purchase, all the more so when they are acquired as part of a trial and error process, as might happen in self assembly. Synthesizing new molecules is often slow and requires highly skilled research personnel, and the cost is accordingly high. Within the process of testing and optimization of self assembly, the cost and length of the production of a new molecule for each iteration present a bottleneck in the optimization process. The effects of this bottleneck could be eased given a family of molecules with rich functionalities whose members are guaranteed to be synthesized at reasonable cost and time. Deposition of large molecules has been so far limited to solid-liquid interfaces. The cleanest deposition techniques for use in UHV were, for a long time, based on the exposure of a surface to gas-phase molecules either from a gas source, or sublimated from a heated crucible [36]. Larger molecules, however, tend to have lower vapour pressures due to the increased van-der-Waals interactions between them [37]. The only deposition techniques for large molecules on surfaces in vacuum were solvent assisted techniques, such as spin coating and dip coating [38]. Although the bulk of the solvent is eventually drained and evaporated, small amounts of solvent will naturally remain on the substrate and on the solute due to intermolecular interactions [39]. Recent developments in electrospray ion beam deposition (ES-IBD) [40] now make it possible to deposit large molecules while carefully eliminating the solvent in the process. Furthermore, this technique introduces additional controllable parameters such as

the charged state of the molecule and the deposition energy. This technique opens up the way for the introduction of larger molecules into the field of on-surface self-assembly. With the door now open to a broad range of molecules, it can be a hard task to choose where to start.

Proteins and peptides would be a valuable contribution to the UHV on-surface self assembly arsenal of building blocks. Naturally occurring proteins are chains made of combinations of 21 building blocks called the α -amino acids. Under physiological conditions, proteins fold into myriads of complex structures, depending on their amino acid composition. Although most of the structures which proteins fold into are not classified, many repeating structural motifs can be found, the most common being α -helices and β -sheets [41]. The specific conformation that an amino acid sequence will adopt is determined by a delicate balance of many interactions between different parts of the molecule such as hydrogen bonds, steric hindrance, electrostatic interactions between charged side chains, etc. [41]. The large alphabet used to construct proteins (21 letters, compared with only 4 in DNA), the flexibility of the backbone and the rich chemistry of the side chains makes proteins capable of an enormous range of functionalities in the human body and in all living things [41].

Unlike the full class of organic molecules, peptides can be synthesized by a repetitive process of adding one amino acid after the other. This so called solid-phase peptide synthesis (SPPS) [42] earned Robert Bruce Merrifield the Noble prize in chemistry (1984) [43] and revolutionized the field of peptide synthesis. The process allows arbitrary peptides to be synthesized quickly, cheap, with a high yield and therefore are available to scientists on demand from commercial companies. This compared with the synthesis of other classes of organic molecules which, unless commercially available, rely on scientific collaborations with experts leading to a slower development cycle, as mentioned earlier.

The use of peptides as building blocks for surface self assembly comes with the vast body of knowledge regarding these molecules. The chemistry of the side chains is well known as well as the mechanics of the backbone. This is a good starting point for the understanding of their behaviour on solid surfaces in vacuum, but not sufficient for predicting it. The interactions of a molecule with its environment are entirely different on inorganic substrates, in vacuum and on nanostructures, than in physiological conditions. The understanding of the interactions of peptides and proteins with solvent-free surfaces requires high resolution techniques, capable of observing the conformations of single molecules. The STM is an excellent technique for this purpose, as it can provide atomic resolution of many substrates [44] and has been used widely for high resolution observation and manipulation of molecules [45]. Furthermore, STM can probe the electronic properties of adsorbed molecules [46], which are relevant for self assembly [47]. Additional modes of measurement can also be harnessed for the purpose of chemical identification, which will prove more challenging as the molecules used grow in size and complexity. An additional advantage of STM is that it is routinely used to study nanostructured surfaces, the properties of which are decisive when used as templates for directed on-surface self-assembly.

List of Figures

It is therefore likely that with a reasonable experimental and theoretical effort, on-surface self-assembly can gain from a rich, versatile and readily available set of building blocks. These building blocks will then join and augment the current toolbox of molecular on-surface self-assembly. Their on-surface behaviour can further be directed by deposition on surfaces which are pre-patterned by the current state of the art surface science techniques [48]. Additional control can be achieved thanks to the ES-IBD's control of the charged states, deposition energy [49] and by post deposition treatments such as annealing [50]. Together, a high level of control of the events on the surface will bring about new and useful class of materials with engineered physical and chemical properties.

This thesis touches four aspects from the field of on-surface self-assembly. The first chapter introduces theory and methods pertinent to this work. The second chapter describes the construction and properties of a STM with nanosecond time resolution, which is one of the best suited devices to study matter at the nanoscale. The third chapter describes a detailed analysis of a well known nanostructured surface and molecular template, h-BN/Rh(111), which helps shed some light onto a standing controversy regarding local work function variations on this surface. These measurements also reveal evidence of quantum confinement of IPSs [51] and suggest a way to extend their lifetimes. The fourth chapter describes early steps towards the use of STM and scanning tunnelling spectroscopy (STS) to identify the individual amino acids composing a peptide. Amino acid identification is an important step towards understanding the interactions that dominate the arrangement of peptides on surfaces. The fifth chapter describes the directed adsorption of proteins on surfaces introducing two levels of control, namely the charged state of the proteins and the nanometre scale patterning of the surface. It is shown how the behaviour of an extremely large and complex molecule, under the proper conditions, can be rationalized with a simple model.

1 Theoretical and Experimental methods

1.1 Quantum tunnelling

Tunnelling is one of the peculiarities of quantum mechanics, a phenomenon with no classical counterpart [52]. In classical physics, an energetic barrier has the effect of a fence or a wall: a particle may either be on one side or on the other side of the wall, not being able to be *at* the wall prevents the particle from ever crossing from one side to the other. In quantum mechanics, a particle can cross such an energy barrier by tunnelling, although with a very small probability. Quantum tunnelling is not only the mechanism behind natural phenomena such as radioactive decay [52] and spontaneous DNA mutation [53], but also the reason for current leakage in large-scale electronic devices which leads to power drain [54].

How tunnelling is possible within the framework of quantum mechanics can be shown by solving Schrödinger's equation in one dimension with a potential barrier of height V and width d (Figure 1.1). Given a particle represented by a wavefunction with energy $E < V$ placed on the left side of the barrier, the wavefunction on the right side of the barrier will be (within a normalization factor)

$$\psi_R \approx \psi_L \times e^{-\kappa d}. \quad (1.1)$$

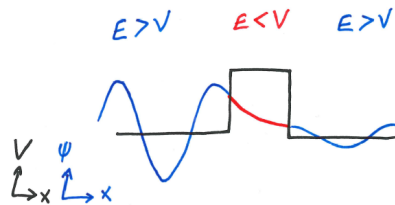


Figure 1.1 – A wavefunction (on the left) that has not sufficient energy to cross the potential barrier will decay exponentially through the barrier but will still have a finite amplitude on the right.

The right hand side of Equation 1.1 shows that the wavefunction decays exponentially within the barrier but does not vanish completely. The decay constant $\kappa = \sqrt{2m(V - E)}/\hbar$ depends also on the particle's mass m and \hbar , which is Planck's constant divided by 2π . This is in contrast to classical physics where the particle's position would be restricted to the left of the barrier.

In solid state physics and electronics, this model is realized by electrons tunnelling between conducting materials through a thin insulating barrier which may be a solid (such as an oxide layer) or a small gap. The insulating barrier must be very thin, on the order of few atomic layers, in order for the currents passing through to be measurable. Such thin solid insulators can be produced using thin film processing technology [55], and in STM, fine control of the tunnelling barrier's dimensions is realized using piezoelectric positioners.

1.2 Scanning Tunneling Microscopy

The STM was invented by Gerd Binnig and Heinrich Rohrer, working in IBM labs Zurich in 1981 [56], an invention which earned them a Nobel prize in 1986¹. STM is based on a principle entirely different than traditional microscopy. In an optical microscope, the image is created by photons scattered off an object, collected and focused using optical elements such as lenses and mirrors. Proximity to the object is not a strict requirement, except for increasing the amount of light collected, and the object only interacts with far field photons². If an optical microscope is analogous to the human eye, the STM can be seen as the microscopic equivalent of reading Braille. In STM the object is brought into close proximity to a sharp metal tip, and interacts with evanescent electrons of the tip.

A STM operating in constant current mode [59] will scan a metal tip across the sample (Figure 1.2), moving laterally by applying a variable voltage to a piezoelectric fine positioner (X and Y signals, see Figure 1.2). The tip is positioned at close proximity to the sample (a few Å) and a voltage is applied between them. The resulting tunnel current is measured and kept constant by continuously adjusting the tip height to compensate for variations in the current. This is done by using the amplified tunnel current as an input signal for a negative feedback loop, the output of which is the voltage applied to a piezoelectric positioner (the Z voltage). The Z voltage is recorded by a computer and STM images are essentially maps of Z .

If the tip is assumed to terminate with a single metallic atom with a radially symmetric (s-wave) electron density, which is constant for all energies, Tersoff and Hamman's approximations [60] yield at zero temperature

$$I = \frac{2\pi eV}{\hbar} \rho_{sample}(E_F) \quad (1.2)$$

where $\rho_{sample}(E_F)$ is the local density of states (LDOS) of the sample evaluated at the centre of the apex atom of the tip. Some current does flow through the neighbouring atoms, but due

¹Together with the inventor of scanning electron microscope (SEM), Ernst Ruska. [57, 58]

²In SEM, the sample interacts with far field electrons.

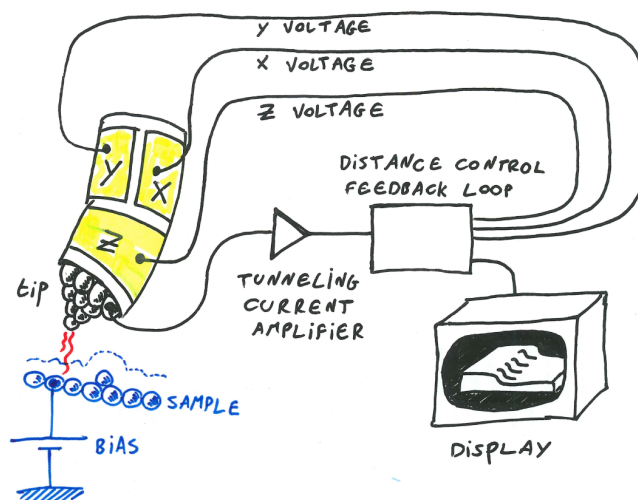


Figure 1.2 – Schematic of the operating principle of STM.

to the exponential decay of the current with distance, 90% of the current flows through the apex atom (for a reasonable tip apex geometry). This strong localization of the tunnel current is the explanation for the exquisite resolution of STM.

According to Figure 1.2, STM topographs should be interpreted as surfaces of constant LDOS, which calls for prudence in their interpretation. On flat surfaces and on flat molecules it is usually straightforward to distinguish topographic from electronic features, and to reach atomic resolution images of the surface. STM provided key information that revealed the structure of the Si(111) 7×7 reconstruction [56]. Examples of mixing topographic and electronic features can be found in the standing electron waves which appear in nanosized structures [61], in sub-surface dopants in semiconductors [62] and in molecules [63]. The electronic information in STM images can nevertheless be valuable and complementary to other techniques which are sensitive only to ionic positions. Additionally, the STM provides atomic resolution measurements without averaging over large domains (as in x-ray diffraction). This makes it ideal for the study of defects on surfaces such as adatoms and step edges [64], which are of paramount importance in chemical reactions taking place on surfaces such as catalysis [65].

1.3 Tunneling spectroscopy

In order to capture all aspects of tunnelling such as the effects of the barrier material properties or bias dependence, a more detailed description of tunnelling is required. Bardeen's treatment [66], based on Fermi's golden rule, estimates the total current by summing over all the quantum states on both sides of the junction

$$I = \frac{2\pi e}{\hbar} \sum_{\mu, \nu} f(E_{\mu}) [1 - f(E_{\nu} + eV)] |M_{\mu\nu}|^2 \delta(E_{\mu} - E_{\nu}), \quad (1.3)$$

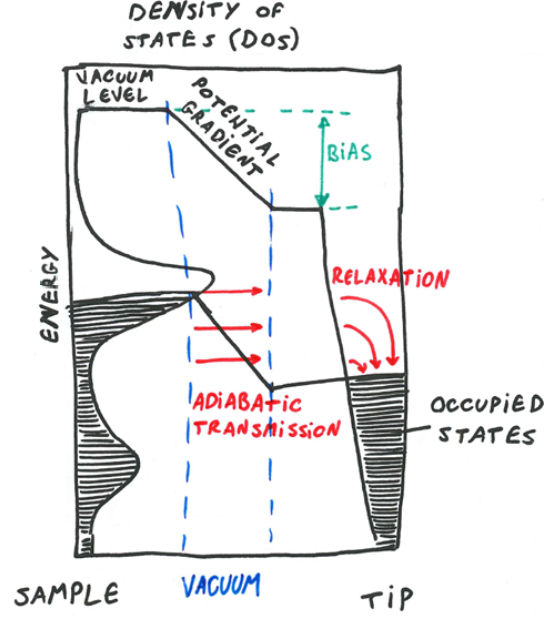


Figure 1.3 – Schematic of electron tunnelling spectroscopy. Elastic tunnelling can only take place from an occupied tip state to an empty state in the sample (dashed arrows). Assuming a constant DOS of the tip, a small bias increment makes new empty sample states accessible for tunnelling. The increase in tunnel current is proportional to the number of newly accessible empty states, which is proportional to the DOS at the bias voltage,

where $f(E)$ is the Fermi distribution function, E_μ and E_ν are the electrochemical potentials on both sides of the barrier and $\delta(E)$ is Dirac's delta function. $M_{\mu\nu}$ is the transition matrix element from state μ to state ν , which is obtained by integration of a current-like operator

$$M_{\mu\nu} = -\frac{\hbar^2}{2m} \int_{\Sigma} (\chi_\nu^* \nabla \psi_\mu - \psi_\mu \nabla \chi_\nu^*) d\mathbf{S} \quad (1.4)$$

where ψ and χ are the sample and tip wavefunctions, respectively.

For the conditions present in STM, certain approximations can be applied to Figure 1.3 and the differential conductivity becomes [66]

$$\frac{dI}{dV}(V) = \frac{2\pi e}{\hbar} \rho_{\text{sample}}(E_F + eV) \rho_{\text{tip}}(E_F) \quad (1.5)$$

where $\rho_{\text{tip}}(E)$ and $\rho_{\text{sample}}(E)$ are the LDOS of the tip and the sample. Since $\rho_{\text{tip}}(E)$ is fairly constant at low voltages, by ramping the voltage while the tip is static the differential conductivity is a direct measure of the LDOS of the sample. dI/dV can be obtained by numerically differentiating an $I(V)$ curve or directly measured using a lock-in technique [67]. The lock-in technique has the advantage of shifting the measurement to higher frequencies, where noises

are reduced (especially $1/f$ noise). Why dI/dV is proportional to the LDOS is also illustrated in Figure 1.3. Since the tunnel current is the sum of tunnelling currents from occupied sample states to empty tip states, the differential conductivity is the incremental current contribution of states at a particular energy, and this contribution is proportional to the density of empty states in the sample. Using dI/dV measurements, a STM can select to scan at a particular energy, allowing it to scan occupied or unoccupied states [67] and directly visualize molecular orbitals [46].

The close proximity of the tip to the surface and fine control the user has over it, make it possible to use the tip as a tool to move and manipulate atoms [61] and molecules [45] on the surface. This technique was used to build a logical gate made of CO molecules on Cu(111) [68], where a cascade of molecular displacements is triggered by the STM tip.

1.4 Nanosecond pump-probe experiments with STM

The time resolution of STM is limited by the bandpass of the powerful current to voltage amplifiers used to amplify the tunnel current. These are commonly around 30 kHz and can reach up to 1 MHz in models designed for speed [69]. This limitation is circumvented in the pump-probe technique [1] by converting high frequency signals in the bias cable (the signal which is not amplified) into a DC signal in the current cable. The technique is effective for a system that can be excited above a threshold voltage, and where the excited and the non-excited states can be distinguished by the tunnel current. If there was no bandwidth limit, the system could be excited using a pump voltage pulse above the threshold, and a smaller voltage would be applied thereafter to track the evolution of the system. In the pump probe technique, the pump pulse is followed by a probe pulse of lower voltage (Figure 1.4). The pump and probe pulses are separated by a variable time delay Δt , during which the system evolves freely. If the delay is extremely short compared with the relaxation time, the system will not have fallen back to the ground state. If the delay is very long, the system will have, with certainty, reached the ground state. In all the intermediate delays the system is probed at intermediate states. The output signal of each pump probe experiment is a tunnel current that is smeared by the low bandpass of the amplifier, and therefore does not follow the instantaneous evolution of the current at the STM junction. However, integrating the output of the amplifier for a long enough period yields a quantity that is proportional to the tunnel current during the probe pulse. By plotting the integrated current vs. the time delay (averaged over thousands of experiments), the transition from the excited to the ground state can be observed and its duration measured. The time resolution then becomes limited by the ability to deliver well shaped voltage pulses to the STM junction, which requires cabling suitable for high frequency transmission. With suitable cabling, time resolution down to 5 ns can be achieved [70], which is suitable for probing magnetic excitations [1] and long lived electronic states [71].

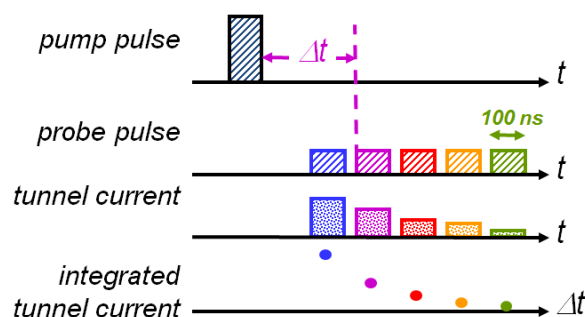


Figure 1.4 – STM pump probe experiments. Principle of an all electrical pump probe STM experiment.

1.5 Electrospray ion beam deposition

The electrospray ion beam was developed by the 2002 Nobel laureate John Fenn [72] as a means to isolate large molecules and bring them into the gas phase. This invention played an important role in the development of proteomics, the analysis of proteins, their composition and their structure. The extraction of isolated, ionized proteins into the gas phase makes them accessible to mass spectrometry which is used to determine their structure (the amino acid sequence) [73]. With an appropriate setup, the gas phase ions can be collected on a solid surface and deposited at controlled energies [4], thus converting electrospray ion beam into a preparatory technique called ES-IBD. In contrast to common deposition techniques in vacuum (such as molecular beam epitaxy (MBE), pulsed laser deposition (PLD) and others), ES-IBD is capable of bringing large molecules intact onto surfaces, including molecules which cannot be sublimated because, when heated, will decompose before sublimating [74].

The ES-IBD chamber used in this work [4] comprises six differentially pumped chambers (see Figure 1.5). A solution which includes the species to be deposited is pushed through a thin steel capillary, whose voltage and temperature are adjustable, into the first of the vacuum chambers. The ions are then collimated and mass selected using ion optics, two rf-quadrupole ion guides and an electrostatic lens. Next the ion beam can be guided into a time-of-flight mass spectrometer for analysis or decelerated onto a target surface.

1.5. Electrospray ion beam deposition

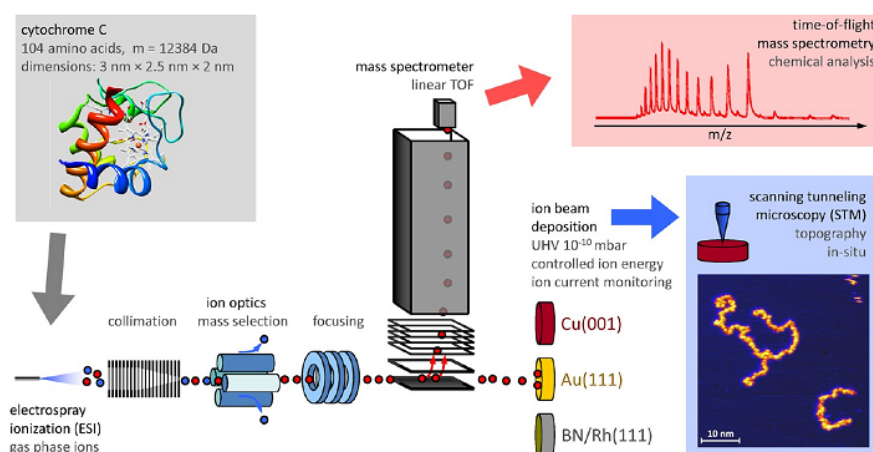


Figure 1.5 – Schematic of the ES-IBD deposition chamber. Reprinted with permission from Z. Deng et al., *Nano Lett.*, 12(5). Copyright 2012 American Chemical Society [5].

2 Construction of the STM

The system described in this chapter was designed to perform novel, state of the art STM techniques and is optimized for STM and STS as it provides UHV, low temperatures, mechanical stability and a low noise electrical environment. The novel all electrical pump probe technique introduced in section 1.4 can be optimized by the use of impedance matched, UHF cabling.

The system (illustrated in Figure 2.1) is divided into a STM and a preparation chamber, separated by an integrated gate valve. In the STM chamber, the STM head is suspended on springs and cooled by a liquid He cryostat. A load lock attached to the preparation chamber allows the introduction of samples, tips and heating filaments without breaking the vacuum. The entire system is attached to an upper frame supported by a set of 4 pneumatic vibration dampers. These dampers rest on a lower frame which is supported by a set of 4 active dampers.

This chapter is arranged as follows. In section 2.1 we describe the STM chamber and the elements within it such as the STM head, the cryostat and the conventional STM wiring. In section 2.2 we describe the preparation chamber, its contents and additional systems such as the UHV pumping system, the vibration insulation system, the load lock and the UHV suitcase.

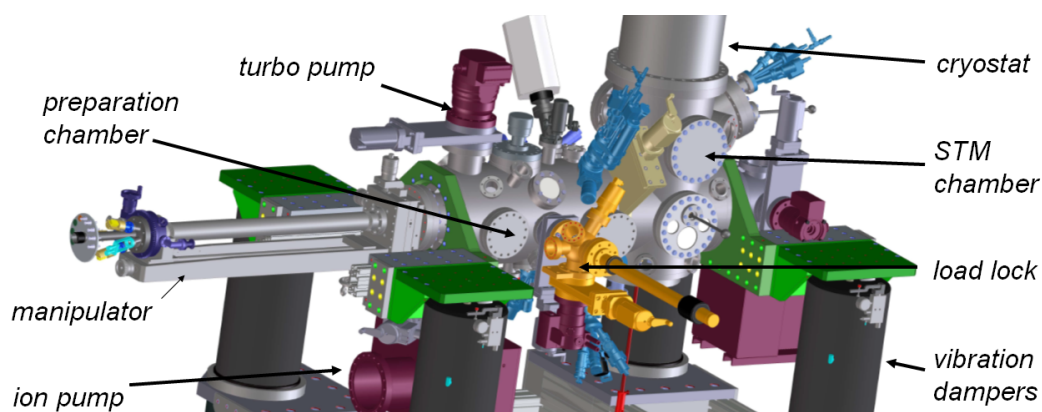


Figure 2.1 – Main components of the STM and preparation chambers.

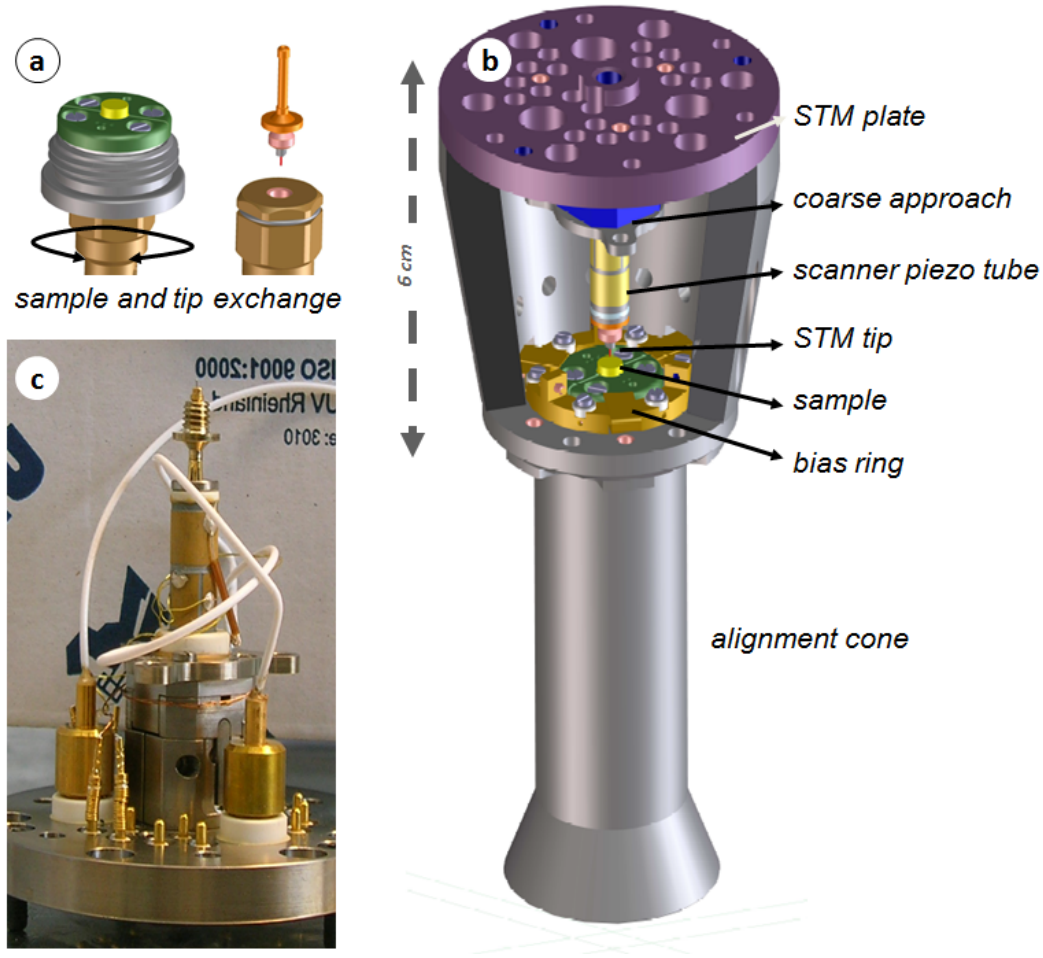


Figure 2.2 – Overview of the STM head. (a) Sample and tip exchange mechanism. (b) CAD model of the STM head. (c) Photograph of an open STM head. The tip holder is extended to reveal the banana plug contact.

Last of all, in section 2.3, we describe the development and characteristics of UHF cabling for nanosecond pump-probe experiments.

2.1 STM head and STM chamber

The STM chamber is a vertical cylinder with a liquid He cryostat mounted on top. Its large radius is determined by the cryostat and its length by the spacial requirements of the STM head (see Figure 2.2) in addition to the springs it is suspended on. A wobble stick at the bottom of the chamber is used to insert the sample into the STM, and a small window next to the wobble stick allows to monitor the transfer. On each side of the STM chamber are two CF150 flanges. The top pair of flanges is reserved for a future implementation of a laser which can be aimed at the sample surface inside the STM. The bottom pair of flanges is fitted with windows and a

wobble stick that opens the radiation shields. An extension to the STM chamber holds an ion pump and a small turbo pump which allow the STM chamber to be pumped independently from the preparation chamber. An additional CF150 flange, positioned at a 50° angle with respect to the chamber's axis, will be used for an evaporator capable of deposition of atoms and molecules onto the sample while the latter is in the STM head. This is a practical solution to immobilize atoms and small molecules that would diffuse and aggregate on the surface if deposited at a higher temperature.

2.1.1 STM head

The STM head is based on the head designed by Ast et al. [?], which offers high stability against vibrations through optimization of the resonance frequencies of its components and through its truncated cone shape. Its modular design makes the STM head easy to fix as it is made of four separable parts (Figure 2.2): the contact plate (or STM plate), the cone (the outer shell), the bias ring and the star assembly (where the tip is mounted). The sample holder is inserted by screwing into an inner thread in the STM head. An alignment cone provides accurate alignment which guarantees safe and reliable sample insertion. The tip is mounted onto a piezoelectric scanner tube which performs the scan and the fine Z motion. The tip is both fixed and contacted using a spring connector (banana plug) which makes tip replacement as easy as unplugging a banana plug. The scanner tube is mounted on an "Attocube" (a slip stick based step motor [69]) which is used for coarse approach and has a motion range of 6 mm . When the sample is screwed in place, it is contacted by three CuBe spring contacts attached to the contact ring. 18 pins and 3 coaxial connectors on the STM plate provide an interface for the electrical signals. The pins and the coaxial connectors are spring loaded and make it possible to detach the entire STM head in-vacuo and remove it for repairs¹. A silicon diode temperature sensor is mounted on the STM plate as well as a heater in order to measure and control its temperature.

The sample holder's unique design (Figure 2.3) can be attributed to the multiple roles it must perform, namely sample clamping, heating contacting and temperature measurement. The sample holder is cylindrical with an outer thread on its exterior, and a hexagonal cavity at its bottom so it can be screwed into place in the STM head. The thread provides strong mechanical as well as thermal contact between the sample holder and the STM head. A hat shaped sample is pressed onto the sample holder by two half-plates, each half plate attached to the sample holder using two screws. The half-plates are made of Pt and PtRh, and are part of a thermocouple circuit which can measure the sample temperature during annealing (range $-40 - 1760^\circ\text{C}$). The sample and the half-plates are insulated against the rest of the sample holder by an Al_2O_3 disk, so that the sample can be placed at a high potential ($\approx 500\text{ V}$) with respect to the manipulator for e-beam annealing.

¹In our setup this option is disabled due to the small size of the openings in the radiation shields.

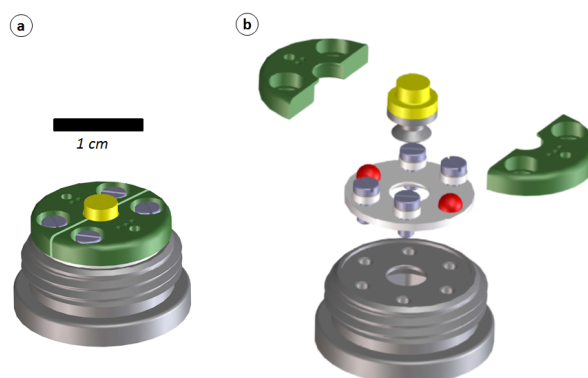


Figure 2.3 – Sample holder. **(a)** Assembled view. **(b)** Exploded view. Yellow - hat shaped single crystal sample. In green - Pt/PtRh half plates, which clamp the sample in place and provide a thermocouple based temperature reading during annealing. White - various Al_2O_3 insulators. Red - ruby half spheres, their role is to align and stabilize the sample without needing additional screws. In grey - molybdenum sample holder body with outer thread and internal hexagonal cavity, tightening screws and (right under the sample) electron collector for e-beam heat distribution.

2.1.2 Wiring

The STM head requires 6 twisted pairs of wires for X, Y (piezo scanner contacts), the Attocube, the heater and the temperature sensor. Tunnel current, bias and Z signals are carried by UHF coaxial cables (described in the next section). The signal wires are divided into two sections: between the feedthrough (at room temperature) and the 4K plate (a plate with electrical connections attached to the bottom of the He cryostat), 0.13 mm Manganin wire is used for its low heat conductivity. From the 4K plate to the STM head, 0.2 mm silver wire is used for its good thermal conductivity. The Attocube wires are an exception because they must have $< 5 \Omega$ resistance in order to reliably transmit voltage pulses to the step motor. The wires used from the 4K plate to the room-temperature feedthrough are therefore 0.2 mm phosphor bronze wires with a total resistance of 5Ω , compared with 75Ω for the Manganin wires.

2.1.3 Performance of the STM

The vibration of the tip-sample junction can be estimated by bringing the tip close to the sample and turning off the feedback loop. Current variations can then be ascribed exclusively to vibration and the width of the current histogram can be used to infer the vibration amplitude. A histogram based on 50000 measurements during 50 seconds is presented in Figure 2.4c, and corresponds to a vibration amplitude of 3 pm. The vibration is mostly at 11 Hz, and it is possible that this vibration can be reduced in the near future thanks to cryostat modifications. Spectroscopic measurements using a lock-in amplifier successfully observed the Cu(111) surface state (Figure 2.4b). Atomic resolution was obtained on the Cu(111) surface (Figure 2.4a) and used to calibrate the piezoelectric coefficients of the scanner.

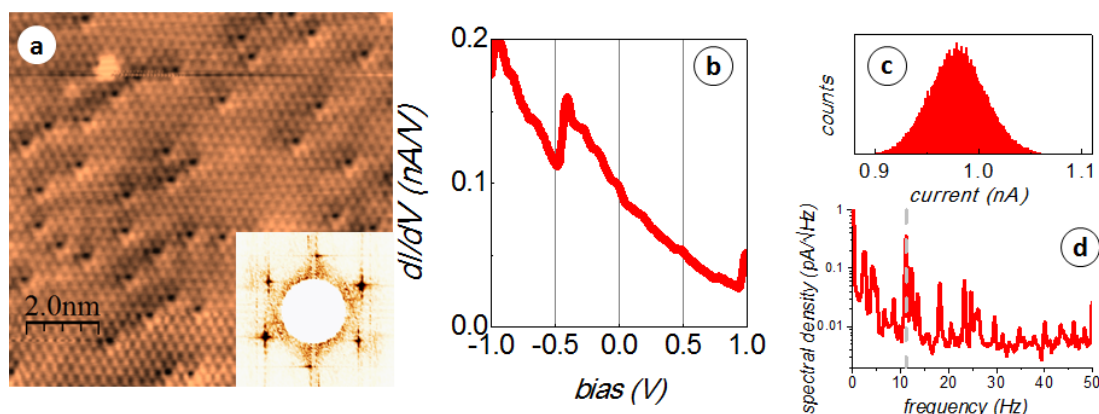


Figure 2.4 – Performance of the STM. **(a)** STM topograph of a Cu(111) surface imaged at $V = +10$ mV, $I = 100$ pA. Atomic resolution is visible in the image and in the 2D Fourier transform in the inset (the central Fourier components were cut out for clarity). The atomic contrast is due to a 2 pm height variation. **(b)** dI/dV spectrum taken on a Cu(111) surface. The characteristic surface state onset at $V = -300$ mV indicates the surface smoothness, cleanliness of the tip and the stability of the STM. **(c)** Current histogram indicates a 3 pm vibration amplitude. The tip was immobilized at $I = 1$ nA and 50000 current measurements were performed during 50 seconds. **(d)** Fourier transform of the current measured during 50 seconds, showing the strongest amplitude at 11 Hz.

2.1.4 Cryogenics

The STM head is cooled to 5.3 K by contact with a liquid He bath cryostat surrounded by a liquid N₂ tank. During measurement the STM head is connected to the cryostat through 3 springs (Figure 2.5), the electrical cables and a cooling braid made of gold fibres. A linear motion mechanism allows the STM to be pulled up until it is pressed against three copper pillars, which provide a better cooling power, a fix the STM head for sample transfer..

The STM head is protected from thermal radiation by two concentric radiation shields (Figure 2.5), one attached to the He dewar and one to the N₂ dewar. The radiation shields are equipped with coupled sliding doors at their bottoms, which can be opened using a wobble stick to let the sample in. The radiation shields are furnished with long oval holes currently covered with copper plates. The plates can be replaced in the future with shutters for in-situ molecule deposition and with windows for shining a laser (Figure 2.5) directly onto the sample.

The success of the cryogenic design can be assessed by a few technical and practical parameters. The base temperature of the STM head is 4.2 K when pressed against the copper pillars and ≈ 5.3 K during operation. The standing time of the cryostat is 4 days. Temperature drift allows overnight measurement in constant height mode without crashing (<3 Å/hour). Samples cool down from room temperature to 4.2 K within 2 hours. Small temperature increases are cooled at a rate of 2 K/min.

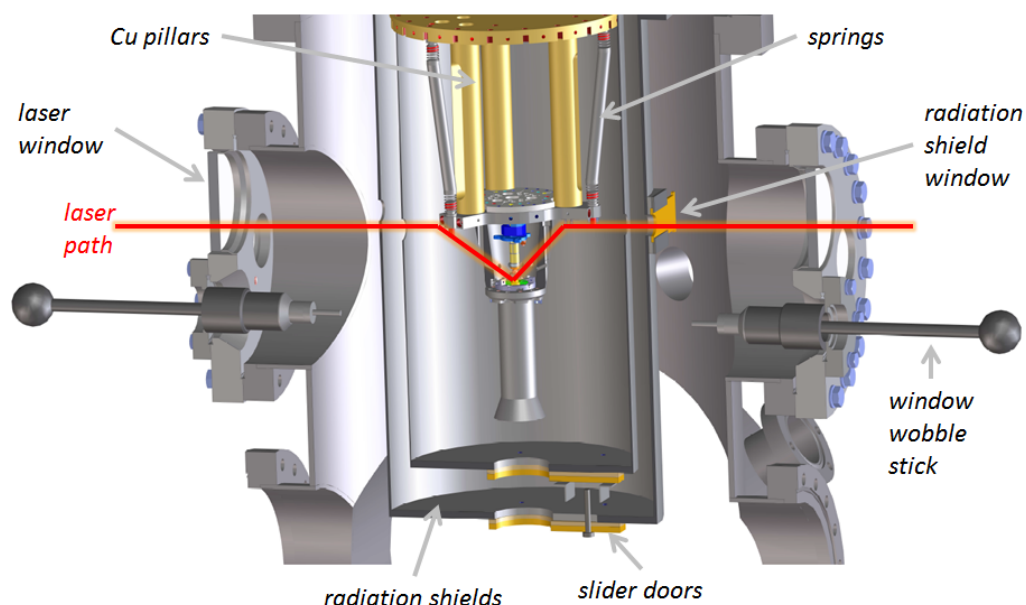


Figure 2.5 – Cut out CAD image of the STM chamber and its internal components.

2.2 Preparation chamber and remaining components

The design of the chamber and the frame is strongly influenced by the use of our home designed, bottom loading STM head [75]. Unlike most STMs, this design requires the use of vertical wobble sticks for sample transfer. The top frame (coloured green in Figure 2.1) must therefore have a particularly small footprint and allow access to the chamber from all directions. The relatively empty space below chamber raises the centre of mass, which is mitigated by the placement of the heaviest elements, the ion pumps, at the bottom. Spreading out the passive dampers contributes simultaneously to the stabilization of the chamber and to the ease of access.

2.2.1 Preparation chamber

The preparation chamber is a horizontal cylinder, with a large manipulator attached to one end and the STM chamber on the other end. The manipulator supports the sample during preparation and can transport it along the chamber's axis. The bottom loaded sample design requires the use of vertical wobble sticks at every point where the sample "changes hands", i.e. at the load lock plane and at the STM position. The preparation chamber is equipped with a quadrupole mass spectrometer (MS) for residual gas analysis. The MS faces the molecular evaporator so it can also be used to characterize the evaporated molecules. Additional evaporators can be placed on the same plane in order to produce combinations of molecules and metals on the surface. Materials with a high enough vapour pressure can be dosed directly through a leak valve or sputtered. The load lock is equipped with its own manipulator that can

carry a sample, a filament for e-beam heating and a tip into the preparation chamber. A UHV suitcase (see Section 2.2.4) can be attached instead of the manipulator in order to transfer samples to and from other UHV systems.

2.2.2 Vibration insulation

Vibration at the tunnel junction is minimized by three stages of vibration insulation (Figure 2.6a). The first stage is a set of 4 active dampers, which sense vibrations and compensate using piezoelectric positioners, efficient in the frequency range of 2 – 60 Hz. The second stage is a set of 4 pneumatic dampers effective in the frequency range of 3 – 30 Hz. The 3rd damping stage is a set of 3 Cu₉₈Be₂ springs on which the STM head is suspended during measurements. According to calculations, the springs are effective for frequencies > 70 Hz. The cryostat was delivered with 3 built in pneumatic dampers to isolate the He stage of the cryostat from the N₂ stage, but they were found ineffective and were removed. The STM head itself is designed to minimize vibrations through optimization of its components' resonance frequencies and overall shape and stiffness [75]. The overall vibration damping is effective enough to allow scanning and distinction of 10 pm features even with the turbo pumps in operation. Vibration in optimal conditions is 3 pm, and is mostly due to a mechanical resonance of the cryostat at 11 Hz. Future modifications of the cryostat may still improve this figure.

2.2.3 Vacuum system

A full scheme of the vacuum system can be found in Figure 2.6b. The preparation chamber is pumped by a large ² turbo pump and a large ion pump. The large turbo pump is backed by a small turbo pump which is backed by a membrane pump. The intermediate turbo pump is needed because the limited H₂ packing ratio of turbo pumps (10000) is insufficient to reach UHV. The ion pump is quipped with a Ti sublimator in order to regenerate the reactive Ti cathode.

During normal operation, the STM chamber is pumped by a 150 l/s ion pump and by the cryostat, acting as a cryopump. When the cryostat is warmed, the STM chamber can be pumped through the preparation chamber or independently through a small turbo pump. The entire system was baked in order to desorb water from the chamber walls, to a base pressure of 4×10^{-10} mbar. The pressure inside the STM was not measured, but it is expected to be about two orders of magnitude lower due to the presence of multiple cold surfaces surrounding it. The load lock is pumped by a small turbo pump and can be pumped within an hour from ambient pressure to 10^{-7} mbar.

²In order to make the text more readable, 300 l/s pumps will be referred to as large and 80 l/s pumps as small.

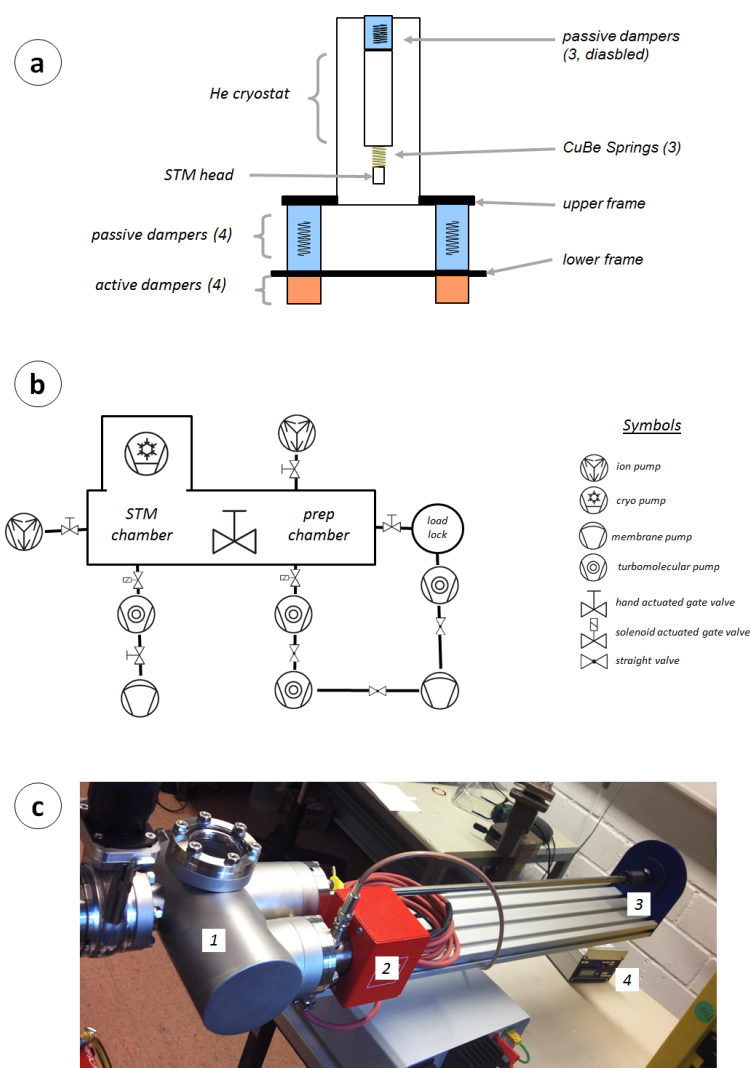


Figure 2.6 – (a) Schematic of the vibration damping system. Passive (pneumatic) elements are coloured blue, active elements are colored in red. (b) Schematic of the vacuum pumping system. (c) UHV suitcase. The suitcase components are 1– suitcase chamber, 2– combined NEG and ion pump, 3– manipulator and support beam, 4– controller including pressure display and batteries.

2.2.4 UHV suitcase

A UHV suitcase is a portable sized UHV chamber which is used to transfer samples between different UHV systems while maintaining low pressure conditions in order to avoid exposure to atmospheric gases and contaminants. The main components of an UHV suitcase (Figure 2.6c) are a pump, a gate valve, a manipulator and a pressure gauge. Some suitcases are limited by the need for a continuous power supply from the grid, while newer models are battery powered and thus portable over long distances. UHV suitcases are pumped by ion pumps, and best results are achieved in combination with a non evaporable getter (NEG) pump made

of a material with very high surface area, such as zeolite. The UHV suitcase used in this work is pumped by a combination of a 100 *l/s* NEG pump and a 20 *l/s* battery powered ion pump. The ion pump is also used as a pressure gauge, as the current of an ion pump is proportional to the pressure. This combination of pumps can reach pressures of 10^{-10} *mbar*.

In a typical experiment, a clean metal surface or a nanopatterned surface is first prepared in the preparation chamber. The sample is then transferred into the UHV suitcase through the load lock, and sealed from the load lock. After the load lock is vented, the UHV suitcase can be removed and attached to the load lock of the ES-IBD system. Once the ES-IBD load lock is pumped, the sample is transferred to a suitable sample stage within the ES-IBD, where the sample is contacted electrically in order to measure the deposition current (in the order of 1 *pA*). Once the deposition is finished, the sample is removed from the sample stage and travels back into the UHV suitcase. The ES-IBD load lock is vented, after which the suitcase is attached to the load lock of the preparation chamber. Once the load lock is pumped, the sample is introduced back to the preparation chamber and from there to the STM, where it is cooled and scanned. The full procedure takes at least 3 hours, most of which is dedicated to pumping and venting load locks. An accurate measurement of the pumping rate of the load lock can be very useful to determine the optimal time to wait before introducing the sample into a chamber, with minimal exposure to residual gases.

2.3 UHF cabling

The time resolution of the technique described in Section 1.4 relies on the ability to transfer well shaped electrical pulses to the STM junction. Typical STM cables are not designed for high frequencies and do not even match the characteristic impedance of high frequency electronics (usually 50 Ω). Very short voltage pulses would thus suffer from distortions and broadening induced along the way to the tunnel junction. A malformed signal at the junction can, to some extent, be corrected by engineering the input signal to compensate for the characteristics of the transmission line. The first paper employing the electrical pump-probe technique [1] obtained well shaped 50 *ns* pulses while a system fitted with the cables described here could reach 5 *ns* pulses [70].

The fabrication of UHF cabling for pump-probe experiments proved to be a challenging task because of the numerous design restrictions:

1. 50 Ω characteristic impedance and UHF transmission up to several *GHz*.
2. UHV compatibility - only low outgassing materials which do not deteriorate at bakeout temperature (80 °C).
3. Top section - low heat conductivity + low temperature compatibility.
4. Lower section - good heat conductivity + low temperature compatibility.
5. Lower section - low vibration transmission, soft and flexible.

The last 4 criteria are common for spring-suspended low temperature STM designs, but criterion number 1 is seldom required in STMs. The poor performance of a commercial low temperature coaxial cable with $40\ \Omega$ impedance can be seen in Figure 2.8 (green). Fortunately, UHF coaxial cables are typically made of UHV and low temperature compatible materials with a Teflon (PTFE) dielectric layer and steel or copper conductors. Suitable connectors are also critical for UHF performance because any variation of the characteristic impedance along the transmission line causes reflection. Here too, sub-miniature version A (SMA) connectors can be found containing only copper, bronze, PTFE and a small amount of silicone.

2.3.1 UHF cabling from room temperature to 4K

The section of cable from the feedthrough to the 4K plate was made of a semi-rigid (SR) stainless-steel coaxial cable, with a silver plated inner conductor. SR cables are the best high frequency cables because the shield is continuous and smooth, unlike coaxial cables where the shield is made of braided fibres. Heat conductivity was minimized by choice of the thinnest cable (1 mm total diameter) and cable materials with low thermal conductivity (PTFE and steel). The contribution of the silver plating to heat conductivity is negligible, while its effect on signal transmission is dramatic. Due to the skin effect [76], AC currents are localized within the skin depth, δ , near the surface of a conductor. The skin depth decreases with frequency ω as

$$\delta = \sqrt{\frac{2\rho}{\omega\mu_r\mu_0}} \quad (2.1)$$

where ρ is the resistivity of the conductor, μ_r and μ_0 are the relative magnetic permeability and the permeability of free space. A $\omega = 1\ \text{GHz}$ signal would in this case be confined to a skin depth of $\delta = 1.6\ \mu\text{m}$, less than the thickness of the silver plating. SMA connectors for this type of cable are commercially available and rated for 18 GHz. The connectors were found to be more stable against torque when glued to the cable with a conductive epoxy, rather than soldered. Our tests confirmed the cables' specifications of UHF signal transmission, with only 8 dB attenuation at 10 GHz (see Figure 2.8, red).

Connecting SR cables directly to feedthroughs is undesirable as the removal of the feedthrough would entail a significant bending of the cable. SR cables were therefore extended with a short piece of common UHF coaxial cable (RG-316) which is more flexible. The lower performance of these cables does not lead to significant attenuation because of the short length used. The electrical feedthroughs contains double sided SMA connectors specified for 10 GHz.

2.3.2 UHF cabling from 4K to STM

The section of cable from the 4K plate to the STM is the most challenging one, and we set out to find the thinnest coaxial cable which would transmit high frequency signals. Unfortunately, the thinnest coaxial cable *with suitable commercial SMA connectors* is 3 mm thick and extremely

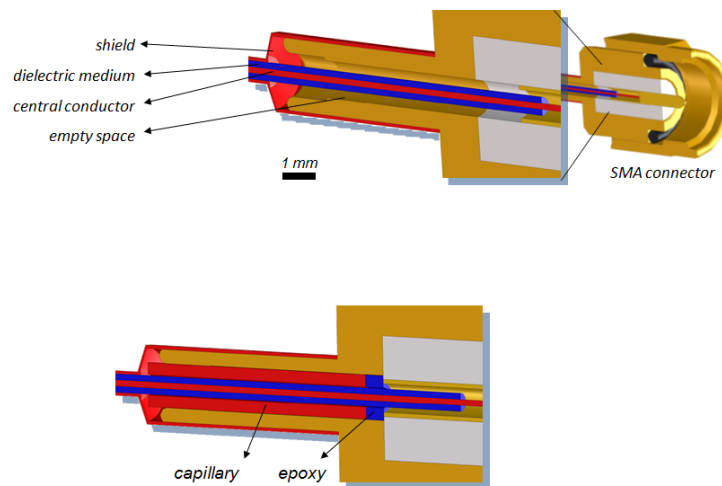


Figure 2.7 – (a) The Cooner cable leaves an empty space inside the SMA connector, leading to structural weakness and contact instability. **(b)** Insertion of a copper capillary coated with a drop of insulating epoxy fills this space, and still maintains the inner pin isolated against the shield.

stiff due to a thick PTFE dielectric and an outer Kapton jacket³. On the other hand, coaxial cables can be found with an outer diameter of merely 0.3 mm, but with poor shielding. A compromise was found in a cable of 1 mm diameter with a full coverage shield and a soft PTFE jacket, made by "Cooner wire".

The cable can be fitted into an SMA connector, but its core is so thin that the space inside the connector remains largely empty. This leads to unreliable electrical contact of the inner pin (Figure 2.7a). It was found we can fill this space and still keep a continuous waveguide by dressing the dielectric of the cable with a copper capillary whose outer diameter fits perfectly inside the neck of the SMA connector, and whose inner diameter fits exactly around the dielectric layer of the cable, providing a continuous value of the characteristic impedance (see Figure 2.7b). The capillary raises yet a new problem: due to the small diameter of the dielectric, the conducting capillary causes a short between the shield of the cable and the inner pin of the connector. The capillary's end was therefore coated with a thin layer of epoxy which insulates the pin against the capillary, but is thin enough so as not to introduce considerable reflection. This solution was found to cause less reflection, and is easier to produce, than the use of a thin PTFE ring between the pin and the capillary. Although an insulator introduces a discontinuity in the characteristic impedance, electromagnetic waves are insensitive to discontinuities which are much smaller than their wavelength, which is 11 mm at 14 GHz. The improved performance of the epoxy drop insulator over the PTFE ring can be understood by the longer discontinuity which the PTFE ring introduces, 0.5 mm, compared with < 0.2 mm for the epoxy drop.

³Kapton, one of the commercial names of polyimide, is 6 times harder than PTFE, with a Young modulus of 3 GPa compared with 0.5 GPa for PTFE.

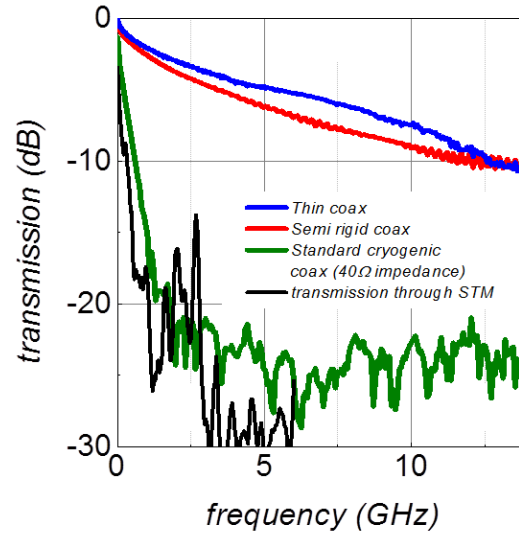


Figure 2.8 – Network analyzer transmission measurements of SR cable (red), soft UHF cable (blue), ordinary cryogenic coax (green) and through the entire STM (black). Transmission through the STM goes down to -10 dB at 300 MHz.

UHF tests with a network analyser showed these cables to be almost as good as the SR cables (Figure 2.8, SR in red and Cooner in blue) and far superior to the commonly found cryogenic coaxial cables which are not $50\ \Omega$ matched. No specifications are available for comparison, as the Cooner cable is not targeted for the communications market.

2.3.3 Performance of the UHF cabling

Although the pump-probe technique only requires one UHF transmission line, two lines are needed for an end-to-end transmission measurement. A third line was installed for redundancy. The transmission through the STM junction can be tested by connecting the network analyser to the I and V connections while the STM tip is indented into a sample (Figure 2.8, black). The result shows a transmission cutoff at 300 MHz, probably due to the impedance mismatch of the home made coaxial connectors on the STM head. In the future the STM head will be fitted with SMA connectors instead. The performance of the cables described here can be estimated thanks to experiments performed in another STM fitted with the cables described here, where pulses of 5 ns were successfully transmitted [70].

3 Local work function variations of hexagonal boron nitride on metal surfaces

The WF is a fundamental property of any metal surface, as it affects the reaction mechanisms and catalysis at the surface [77]. Local variations of WF on a nanopatterned surface can elucidate the distribution of charge on the surface [78]. The distribution of charge can affect the properties of molecules on the surface through lateral electrical fields [2] or by local doping [79]. In return, charge transfer between molecules deposited on a surface affects the local WF [78]. Exact measurements of local WF variations on the nanoscale are experimentally challenging. The scale of few nanometres is too small to resolve using radiation and transport based methods [77]. One example is the WF variations of h-BN/Rh(111), where agreement between theory [3] and experiment [2] is still lacking. Scanning probe microscopy (SPM) techniques routinely provide excellent resolution at the nanometre scale, therefore they are useful in measuring the value of these WF variations [80, 81]. In this chapter we describe three SPM techniques to measure local WF variations on the h-BN/Rh(111) surface. We pursue one of these techniques to estimate the lifetimes of hot electrons in the so called "field emission resonance" (FER) states. In the end of this chapter we explore a new phase of h-BN/Rh(111) and the conditions in which it can be generated.

3.1 Local work function measurement using STM and AFM

The WF of a surface is defined as the thermodynamic work required to remove an electron from the surface into vacuum just outside the surface [82]. The WF is not a property of the material itself but rather of a surface, as different terminations of the same substance can have different WFs. The reason for this is that different terminations vary in charge density, or surface dipole density, properties that affect the electric field near the surface. For example, the work function of Ag is 4.64 eV at the (100) face, 4.52 eV at the (110) face and 4.74 eV at the (111) face [83]. This difference can be rationalized within the jellium model of the electrons in a metal [84]. In this model, the valence electrons are approximated as a negatively charged cloud around a uniform, positively charged static background. At the surface, the ion lattice terminates abruptly and the electron cloud "leaks", to some extent, into the vacuum. This

leakage creates a negatively charged layer just outside the surface, and a positively charged layer just under the surface, due to partial electron depletion. This dipole layer acts as a plate capacitor where the electrical field pushes electrons inwards, thus increasing the WF. Within this model, the density of atoms at the top layer plays an important role: a dense layer of atoms (as in the (111) face of an fcc crystal) means a high density of ions at the surface. The electronic cloud would need to extend further into the vacuum in order to screen this dense ionic background, leading to a larger surface dipole layer and an increased WF.

WF can vary not only between different faces of a material, but can also vary laterally on a surface. For example, Ag deposited on Pt(111) [85] forms a stress relief pattern (see Figure 3.1) which includes three types of areas, each type characterized by a different density of Ag atoms. As in the bulk Ag case, each atom density corresponds to a different local WF. WF variations can also occur when an adlayer exhibits locally varying degrees of charge transfer from the substrate. Such is the case for thin dielectric films, such as NaCl [80], graphene [86] and h-BN [3] supported on metals. In these cases, a small lattice mismatch leads to a varying atomic registry between the dielectric layer and the substrate, which leads to a laterally varying degree of charge transfer to the dielectric, and thus to a varying WF. Adsorption of molecules accompanied with charge transfer will also change the local WF of a surface [87], and WF has even been found to vary along a single molecule due to a varying electron affinity along the molecule [78]. Local WF variations are important because they affect the electronic properties of the surface and can lead to lateral electrical fields with the capacity to trap molecules at particular regions of the surface [2], making it an effective nano-template. It is therefore desirable to map local WF variations at this scale and correlate them with structural properties of the surface [88]. In the following section, we describe three SPM based techniques that combine topography mapping with local WF variation measurement.

It should be mentioned that within the traditional definition of WF mentioned above, "just outside the surface" means in the order of a micron away from the surface, a sufficient distance for electrostatic interaction to be negligible, in order to avoid any effect of the image charge energy on the WF. Within this definition, WF cannot display variations on the nm scale. For this purpose an alternative definition was introduced by Wandelt [77] which defines local WF as "the local surface potential measured from the Fermi level E_F ", which allows a meaningful discussion of WF variations at the nanometre scale.

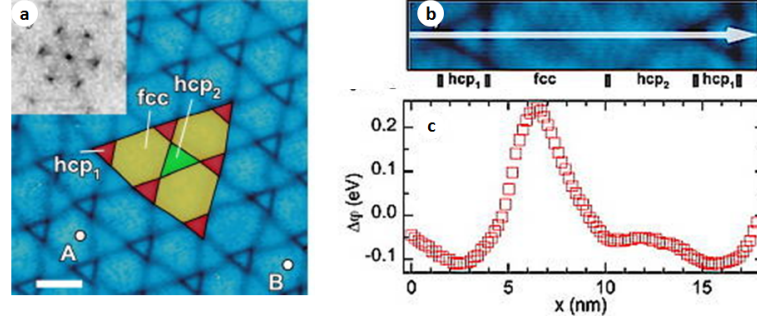


Figure 3.1 – (a) STM topography of the strain relief pattern of Ag/Pt(111). (b) Path along which a WF measurement was performed. (c) WF variation along the path. Figure adapted from [85], copyright (2009) by The American Physical Society.

3.1.1 Probing WF variations using STM approach curves

The exponential decay of the tunnel current, I , with the tip sample distance in a STM, z , can be calculated using the WKB (Wentzel–Kramers–Brillouin) approximation [89]

$$I = A \times \exp\left(-\frac{\sqrt{8m(\Phi - U)}}{\hbar} z\right) \quad (3.1)$$

$$\log(I) = \log(A) - \frac{\sqrt{8m(\Phi - U)}}{\hbar} z \quad (3.2)$$

where Φ is the local WF, U is the bias, \hbar is Planck's constant divide by 2π , m is the electron mass and A is a constant. Defining κ as the linear fit coefficient of $\log(I)$ as a function of z , we obtain

$$\Phi = \frac{\hbar^2 \kappa^2}{8m} + U \quad (3.3)$$

It is important to note that Φ is not the exact work function, but rather the effective barrier height for tunnelling. This value is often regarded as the average of the WFs of the tip and the sample [89]. The local values obtained are therefore not regarded as WF measurements, but since the tip's WF does not change during the measurement, the variations of the local barrier height are identical to variations of the WF. In order to map WF variations and correlate them with structural features, a map is acquired by performing an approach of the tip at each point on a grid while simultaneously recording the values of I and z . The logarithm of I is then fitted to a linear function of z , and the slope yields κ , which is used to calculate a local value of Φ according to Equation 3.3. In $I(z)$ curves, the fit accuracy depends more on the range of currents than on the number of data points, hence it is important to choose the highest possible range of currents. The lowest currents that can be reliably detected (1 – 5 pA in our case) sets the lower limit of this range. The higher boundary of current is limited in theory

Chapter 3. Local work function variations of hexagonal boron nitride on metal surfaces

by the transition from tunnelling to point contact, when $I(z)$ ceases to grow exponentially, at values of few μA . In practice, we set this limit rather by concerns for the stability of the tip and the sample throughout the mapping, to values near 500 pA on clean h-BN and even lower on molecules.

An alternative, faster mode which relies on Equation 3.2, consists of continuously scanning the surface while modulating the tip sample distance with a small amplitude, z_1 , around the tip's altitude, z_0 . The resulting current for

$$z(t) = z_0 + z_1 \cdot \sin(\omega t) \quad (3.4)$$

is

$$I = A \cdot \exp \{-\kappa [z_0 + z_1 \cdot \sin(\omega t)]\}. \quad (3.5)$$

The use of a logarithmic amplifier allows to record directly $\log(I)$, giving rise to a DC component of $\log(I)$ which is proportional to the average position of the tip and an AC component at the frequency ω , I_ω , equal to

$$I_\omega = -\kappa \cdot z_1 \quad (3.6)$$

If the modulation is added at a frequency much higher than the feedback loop response frequency, the modulation will not disturb the topographic measurement. On the downside, in this type of measurement the oscillation amplitude is smaller than the z range used in approach curves, leading to a noisier signal.

3.1.2 Probing WF variations using field emission resonance maps

On the surface of many metals, a projected band gap of the bulk band structure leads to a potential barrier impeding the entrance of electrons into the bulk [90]. An electron hovering near the surface of the metal will however feel the attraction towards the surface due to its own image charge. The combination of the image charge attraction and the projected band gap repulsion leads to an effective potential well which can accommodate a series of unoccupied hydrogen atom like electronic states, lying a few Å above the metal surface (Figure 3.2a) [91]. IPSs have lifetimes in the femtosecond range [92] and energies starting near the vacuum level of the metal. IPSs are delocalized in the surface plane, therefore on a flat surface each IPS

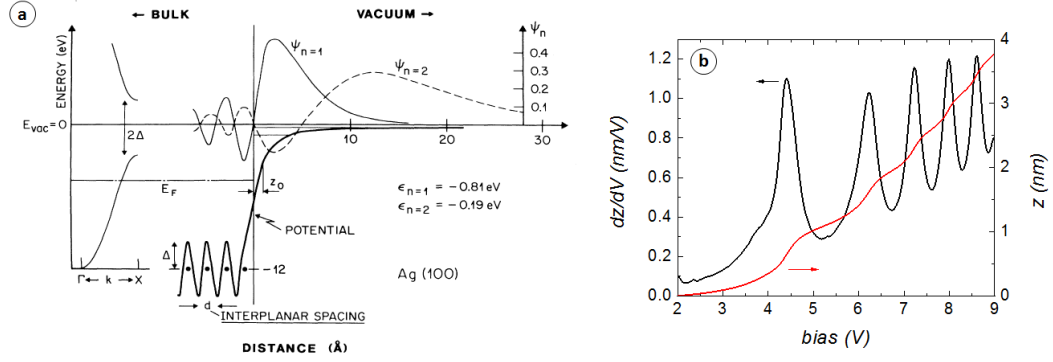


Figure 3.2 – (a) One electron potential for IPSs (bold line) and wavefunction amplitudes of the first two IPSs (thin and dashed lines). On the far left the projected bandgap is depicted. The distance z_0 ($\approx 1 \text{ Å}$) specifies the distance from the surface at which the potential is purely Coulombic (image like). Copyright (1985) by The American Physical Society [93]. (b) STM $z(V)$ and dz/dV spectra taken at constant current (20 pA) on Cu(111). Peaks correspond to FERs.

consists of a full band of a 2D electron gas [91].

IPSs can be probed with inverse photoemission (as they are unoccupied states) [94], and exact lifetimes can be obtained with 2-photon photoelectron spectroscopy (2PPE) [92]. In 2PPE the surface is the target of two photon pulses with different energies separated by a short delay. Ideally, the first pulse is chosen with sufficient energy to excite electrons from the bulk to the IPS. The energy of the second pulse is sufficient to push electrons in the IPSs above the vacuum level, but insufficient to excite electrons from the bulk to the IPS. Emitted electrons are then detected only if the second pulse was emitted before the electrons decay back into bulk states. By varying the delay between the two pulses, the decay process can be monitored and the exponential decay constant calculated [92]. Angle resolved 2PPE also enables momentum resolved lifetime measurements. Such measurements on Cu(100) [95] have shown that the lifetime of IPSs is inversely proportional to the in-plane momentum due to intraband elastic scattering.

STM can access IPSs using dz/dV spectroscopy. dz/dV spectroscopy is performed by ramping the voltage while keeping I constant, and recording the z value throughout. When the voltage reaches the energy of an IPS, the tip will retract quickly, typically $2 - 3 \text{ Å}$ per IPS. The energy values of these retractions can be clearly seen in dz/dV curves, for example in Figure 3.2b. The dI/dV signal will often be simultaneously recorded and yield the same peaks. When probed with STM, IPS are subjected to strong electric fields which cause a Stark shift that distorts the energy spacing of the IPSs [96]. In this text we follow the convention that IPS refers to the unperturbed states while the dz/dV peaks that mark the detection of Stark shifted IPSs are referred to as FERs [96].

Because of their distance from the surface, FERs are weakly coupled to the surface and their energies are determined with respect to the vacuum level, and so variations in the energy of FERs are related with variations of local WF [80]. Because the Stark shift is stronger for higher biases, WF variations are ascribed according to the variation of the first FER. This technique is not suitable for use on molecules because they are unstable at such high biases. STM measurements of FERs, unlike radiation based techniques, have the advantage of probing FERs at a specific position, and thus not broadened by summation over different structures [97]. It has been noted however by S. Crampin [96] that the FER lifetimes observed by STM on Cu(100) are shorter than those observed by 2PPE, due to various reasons. Crampin argued that the electrical field in the tunnel junction pushes the FERs towards the bulk, thus increasing the spatial overlap between the FER and the bulk. In addition, FERs have a decay channel that is not available to IPSs - into the tip, which further reduces their lifetimes. Pascual et al. [98] found that the variation of electrical field in the tunnel junction further contributes to the peak broadening. An additional cause for FER broadening is that it is probed with a fermionic system at finite temperature, leading to thermal broadening of the tip's DOS of 1.4 meV at 5 K .

Because of their quantization in the z -axis and their free electron like behaviour in the surface plane, FERs offer an interesting playground for understanding the behaviour of electrons in complex potential landscapes. These landscapes can reproduce those observed in bulk crystals: (i) a potential discontinuity, such as a step edge, (ii) a small patch of attractive potential, or a quantum dot and (iii) a periodic potential. FERs are scattered at step edges [64]. Near the step edge, the standing wave patterns of the scattered FERs can be observed using dI/dV maps. These maps can further be used to deduce the wavelength, and thus the momentum, of FERs as a function of energy [64]. If a small island is surrounded by a large surface with a different WF, FER electrons experience an energy barrier at the edges of the island. The FERs on the island become laterally confined and well described by the “particle in a box” potential [99, 100, 101, 102], giving rise to quantized modes inside the island. When observed by STS, the FER peaks are split into several quantized modes [100, 101, 102, 103]. Here too, dI/dV maps can resolve the standing wave patterns of the laterally quantized states, although not all standing waves are observable by STS [103]. These quantized states on top of the island have also been observed to mix with a FER of the surrounding surface, which causes an energy shift and significantly extends the probability density of these states beyond the island [103]. These mixed states are observed in dI/dV maps as rings surrounding the island, as their coupling with the STM tip is maximal around the island. STS has proven advantageous in the study of FERs on isolated structures, thanks to its local measurement capabilities. The standing wave patterns of FERs on small graphene patches on Ir were imaged by STM on different island sizes [101], whereas 2PPE measurements on the same system failed to distinguish the splitting of the IPS into quantized states, probably due to the distribution of island sizes [104].

Periodic modulations of the WF lead to deviations from the free-electron-like parabolic dispersion [105, 106, 107, 108, 86, 109, 110, 111, 112]. A weak potential may increase the effective mass of the free electron like states [105]. A stronger potential modulation can cause band

folding and the opening of a bandgap, when the delocalized FERs react to the potential in the way expected for Bloch states [113, 106, 114, 109, 110, 112]. An even stronger potential leads to full localization of the FERs [106]. The various effects of localization are, however, difficult to distinguish in STS as the momentum is not measured directly.

3.1.3 Kelvin probe force microscopy

An AFM is based on a similar principle as the STM, except the signal used to control the distance between tip and sample is not a current but a force. The force is detected through the deflection of the AFM cantilever or, in non-contact AFM, by the frequency shift of the oscillation. The AFM tip, having a different work function than the sample it is scanning, will experience electrostatic forces originating from dipole layers formed on the substrate and on the tip as a consequence of the difference in work functions, called the contact potential difference (CPD) [115]. When using a conductive AFM tip, the electrostatic force can be compensated for when the bias applied to the AFM tip compensates the CPD [116]. For the measurement, the AFM tip oscillates at a frequency ω and the potential difference between tip and sample is

$$V = (V_{DC} - V_{CPD}) + V_{AC} \cdot \sin(\omega t) \quad (3.7)$$

where V_{DC} is the DC bias applied to the tip, V_{CPD} is the CPD and V_{AC} can be externally applied or induced by the tip oscillation. The electrostatic force on the tip can be found by differentiating the energy with respect to the tip-sample distance z , using the formula for the energy of a plate capacitor

$$F = \frac{1}{2} \frac{dC}{dz} V^2 \quad (3.8)$$

where C is the capacitance between the tip and the sample and V is the potential difference between the two. Substituting V with Equation 3.7 yields a force with a DC component and a component at frequency ω

$$F_\omega = \frac{dC}{dz} (V_{DC} - V_{CPD}) V_{AC} \cdot \sin(\omega t) \quad (3.9)$$

F_ω can therefore be used to measure the CPD as it becomes zero when the DC bias equals the CPD. Mapping the CPD in this way is called Kelvin probe force microscopy, or KPFM. Accurate values of WF can be determined if the tip is "calibrated" by measuring the CPD on a surface of

known WF. Even in the absence of an exact calibration, CPD variations measured on a surface allow one to determine WF variations, as the WF of the tip is constant during the measurement and variations arise only due to variations of the local WF of the surface.

3.2 Electronic properties of hexagonal boron nitride on metal surfaces

The discovery of graphene by Konstantin Novoselov and Andre Geim [117] did not only award them the Noble prize in physics in 2010, but unleashed a fury of research into the fabrication and properties of 2D materials. Graphene was quickly found to have extraordinary properties such as extremely high mobility (up to $200000\text{ cm}^2/(Vs)$ [118]), a record breaking Young's modulus of $Y = 1\text{ TPa}$ [119] and an unusual electronic structure making it appealing for photonic and optoelectronic applications [120]. These unusual properties, and the possibility of synthesizing stable two dimensional layers only one atom thick, inspired others to seek more 2D materials. One of the most promising materials in that respect is h-BN, which forms an unusually stable hexagonal network, similar to graphene. h-BN and graphene are similar not only in their symmetry and lattice constant [121], but also in the interlayer spacing of multilayers [122]. Due to these similarities, h-BN is sometimes referred to as "white graphene". Unlike graphene, an h-BN monolayer is an insulator with excellent dielectric properties, and thus can be used as a dielectric layer between conductive monolayers [123, 124]. Placing graphene on top of h-BN achieved an effective decoupling from the substrate and a Moiré pattern that allowed measurements of Hofstadter's butterfly [125, 126]. By stacking different combinations of 2D materials, new functionalities can be achieved that are not present in the individual layers [127, 128].

h-BN has nevertheless many useful properties of its own. Thanks to its graphite-like multilayer structure, it is considered a non conductive lubricant [129]. Its lower electrical conductivity and chemical reactivity make it preferable over graphite as an insulating and chemically inert lubricant. Single layers of h-BN can be prepared by chemical vapour deposition (CVD) on a variety of transition metal surfaces (Ni [130], Ir [131], Pd [132], Ag [133], Pt [132], Cu [134] and Rh [135]), where they often exhibit Moiré superstructures due to small mismatches with the metals' lattice constants. On Rh(111) the result is a strongly corrugated sheet of h-BN with modulated electronic properties, and a useful capacity of trapping molecules in nanosized cavities [136].

3.2.1 Structure, preparation and properties of h-BN on Rh(111)

Single layered h-BN on Rh(111) was prepared by CVD of borazine (Figure 3.3a) $\text{ga}, (\text{HBNH})_3$, on a Rh(111) surface heated to 800°C . At this temperature a full monolayer (ML) requires an exposure of 110 L . The clean Rh surface for our experiments was prepared by repeatedly sputtering a single crystal of Rh with $1\text{ }\mu\text{A}$ of Ar^+ ions at 1 kV for 20 min and annealing to

3.2. Electronic properties of hexagonal boron nitride on metal surfaces

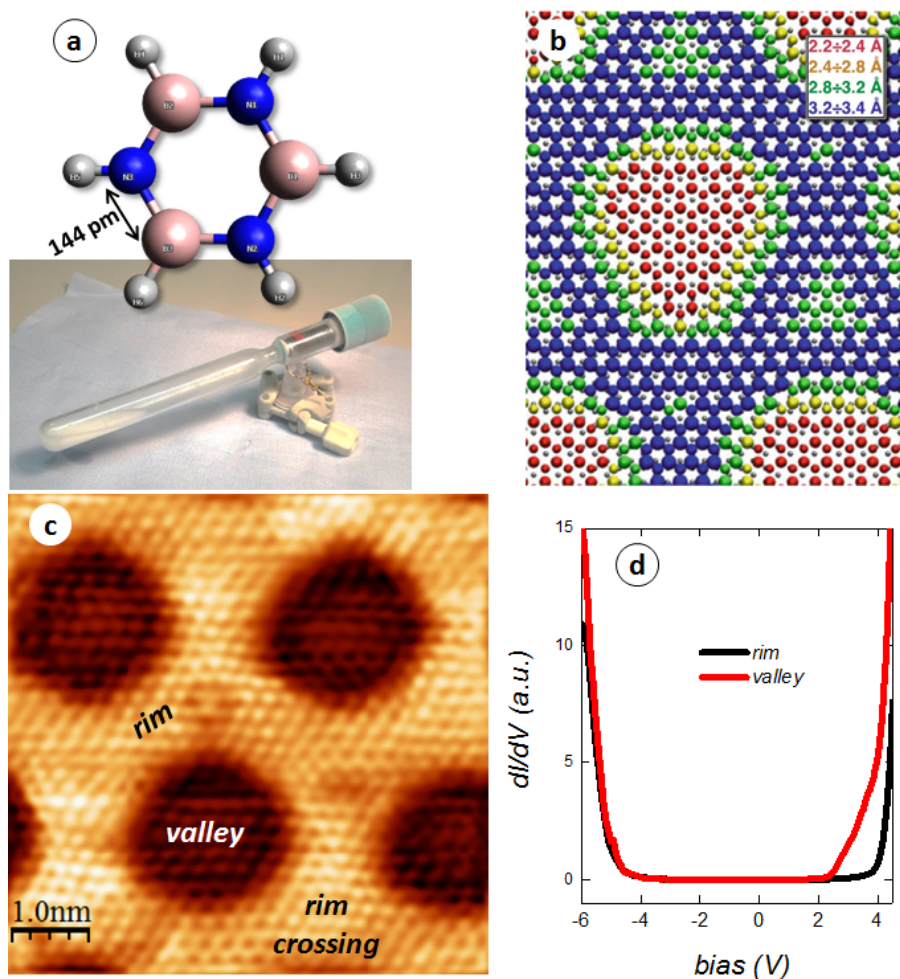


Figure 3.3 – (a) Borazine, $(\text{HBNH})_3$, the precursor molecule for h-BN formation. Atoms are colour coded according to elements with N in blue, B in red and H in white. Below the molecular structure is a photo of a vial of liquid borazine. (b) Atomic overlay of h-BN/Rh(111) calculated by DFT. Atoms are colour coded according to their distance from the top layer of Rh (the Rh atoms in grey). Image adapted from [3], copyright (2013) by Springer. (c) Atomic resolution STM image of h-BN/Rh(111). $V = -2 \text{ V}$, $I = 10 \text{ pA}$. (d) dI/dV spectra taken on a valley and a rim.

800°C for 5 min . In order to create a depletion layer free of native carbon contaminants, the sample was submitted, before the preparation of h-BN, to one hour of hot sputtering at 830°C with $1 \mu\text{A}$ of Ar^+ ions.

h-BN forms a corrugated sheet whose height above the Rh varies between $2.2 - 3.4 \text{ \AA}$, with a hexagonal Moiré superstructure, resulting from the lattice mismatch between the h-BN and the top Rh layer (Figure 3.3a) [135]. According to density functional theory (DFT) calculations [3], the Moiré structure consists of quasi hexagonal valleys which are lowered towards the Rh surface. Inside the valleys, the B-N bonds are stretched (145 pm) in order to improve their

registry, with the N on top of Rh atoms. Between the valleys the h-BN sheet curls away from the surface and forms rims, where B-N bonds are slightly compressed (143 pm). The single layered h-BN is an insulator with bandgap of around 5 eV at the rims and 7 eV at the valleys (Figure 3.3d). The Moiré structure is clearly visible in STM images (Figure 3.3c). The valleys are imaged as deeper because the increased coupling to the Rh partially depletes the conduction electrons in that region, while on the rims the Rh is undisturbed. h-BN/Rh(111) has proven to be an effective decoupling layer, allowing molecules and clusters deposited on it to retain their electronic properties [137]. Compared with other decoupling layers, it offers the advantage of a trapping potential [2], which prevents the deposited species from aggregating on the surface after deposition, and allows to address isolated species with STM.

3.3 Local work function variations on h-BN/Rh(111)

In this work we discuss local WF variations on h-BN/Rh(111) using three techniques: approach curve maps, FER maps and KPFM maps. The three methods are compared with respect to their capacity to resolve small variations of WF on nanometre sized structures, and provide an estimate of the WF variation on h-BN/Rh(111).

3.3.1 Approach curve maps

For these experiments we define a grid of points on the surface, and at each point of the grid the STM tip approaches the surface while simultaneously recording the I and z . The curves are analysed using a Matlab scrip which extracts for each curve three parameters: the linear coefficient of the $\log I(z)$ fit, referred to as κ in Equation 3.3, the starting value of z (which generates a topographic image) and R^2 , a measures of the goodness of the fit. The last parameter is useful in detecting events such as a tip change, which may change the WF of the tip midway through the map.

The three parameters are then visualized as in Figure 3.4. The WF map is calculated using Equation 3.5 and based on the local values of κ (Figure 3.4a). It is visibly well correlated with the topography (Figure 3.4b), with valleys showing a significantly lower work function than the rims. The map of R^2 (Figure 3.4c) shows the fit is successful at all points of the map, with a minimal value of 0.9999, indicating there were no tip changes during the acquisition of the map. The R^2 map shows a slight tendency for better fits on the rims. This might arise from the reduced density of conduction electrons at the valleys, leading to a higher contribution of d-electrons to the tunnel current. If two types of electrons with different decay lengths contribute to the tunnel current, then the $I(z)$ curve is effectively a sum of two exponentials, leading to a slight reduction in the goodness of the fit to a single exponential. This effect, however, is very small and has no effect on the accuracy of the values extracted from the curves.

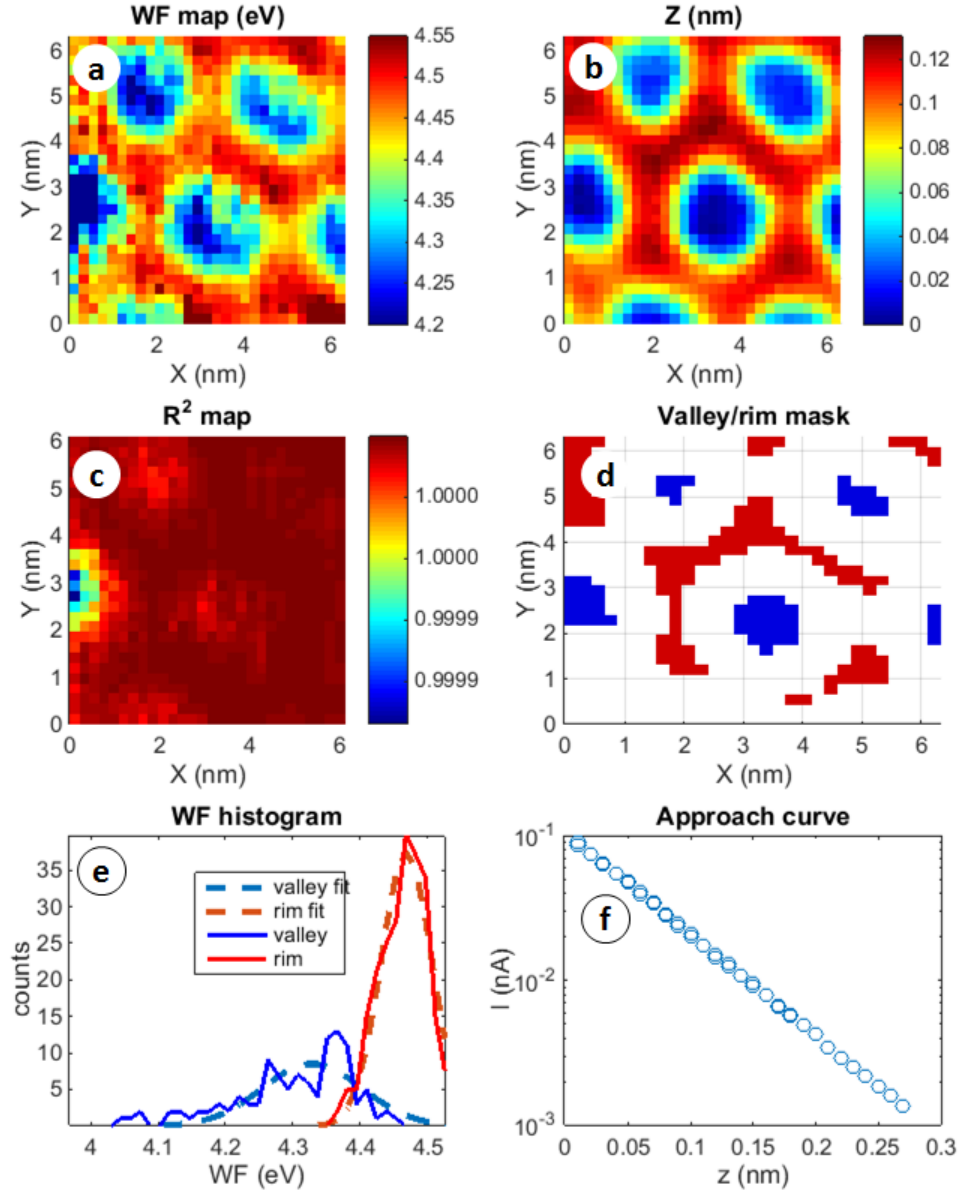


Figure 3.4 – Results obtained from an approach curve map. **(a)** Local apparent WF map. **(b)** STM topography, $V = -2$ V, $I = 20$ pA. **(c)** R^2 map. **(d)** Map of the mask used to distinguish between rims (red) and valleys (blue). **(e)** Histogram of apparent WF values measured on rims (red) and on valleys (blue) and corresponding fits to Gaussian curves. **(f)** Representative approach curve on a semi-logarithmic scale. The slope represents the parameter κ from Equation 3.5, and the same equation is used to calculate the local WF which is mapped in (a).

In order to obtain WF estimates for rims and valleys separately, we need to distinguish between valleys and rims. This was done by defining a lower threshold for the topographic map, below which a pixel is classified as belonging to a valley, and an upper limit, above which a pixel

is classified as belonging to a rim. The thresholds were set so that only pixels which clearly belong to either a valley or a rim are counted. Figure 3.4d shows which pixels were classified as valleys (blue) and as rims (red). Using this classification, the WF values corresponding to valleys and to rims were collected separately and the histograms of WF values for valleys and rims are presented in Figure 3.4e. Each curve was fitted to a Gaussian curve in order to determine the centre of the distribution and the variance.

The fitting to the histograms yields a WF of 4.32 ± 0.08 eV for the valleys and 4.47 ± 0.03 eV for rims. The WF variation between valleys and rims is therefore 150 ± 80 meV. The large spread of WF values at the valleys is caused by two factors: variations inside the valleys and variations between valleys. An apparent WF variation inside the valleys can be seen in Figure 3.4a, where for all the valleys the apparent WF increases towards the top right side of the valley. This is caused by an asymmetric tip artefact whose details are discussed later. The variation of WF between the valleys raises the question whether the valleys are in fact all identical. Small variations in valley shape can be seen in STM topographs (see Figures 3.4b). These differences of the shapes of valleys in STM topographs can arise from sub-surface defects or contaminants.

The aforementioned factors will increase the spread of the observed WF values, but are not systematically biased. Diagonal tunnelling is a factor that adds a systematic error to the observed values of local WF in the valleys. When an approach curve is measured in a valley, the rim contributes a small amount of the tunnel current. This diagonal current smooths out differences in WF, as it arrives from areas with a higher local WF. Diagonal tunnelling is also possible in the opposite scenario, with the tip on top of a rim, but accounts for a much smaller fraction of the total current, as will be shown. In order to assess the relative contribution of the diagonal current at a distance x from the centre of a valley (or from a rim crossing), a schematic of the topography of a single valley was generated using Matlab (Figure 3.5a). The tip was modelled as a single sphere of 134 pm radius, the metallic radius of a Rh atom [138]. Following tip preparations on the bare Rh surface, it is likely that the tip apex is made of Rh. The tunnel current was assumed to decay exponentially with the absolute distance between the tip and each substrate point. The decay constant of the tunnel current was taken as an average from the approach curves, equal 2.8 \AA^{-1} . The relative contributions of tunnelling current from the valley and from the rim were evaluated for different positions of the tip (viewed from the top in Figure 3.5b and from the side in Figure 3.5c). Figure 3.5d shows, in red, the percentage of the current coming from the rim, as a function of the lateral tip distance from the centre of the valley. A contribution of 6% can already make a significant impact on the observed WF, as this is approximately the WF variation as a percentage of the total WF. With at least 10% of the tunnel current incoming from the rim, the local WF in the valley cannot be accurately measured anywhere in the valley. Furthermore, the further the tip is from the valley centre, the greater the observed WF is biased towards the rim's WF. Similarly, the red curve in Figure 3.5d shows the percentage of the current coming from the valley, as a function of the tip distance from the rim crossing. The rim crossing has a patch of about 6 \AA where the WF can be accurately measured. This striking difference is due to the increased vertical distance between the tip and the rim in this case, due to the lower apparent height of the valleys.

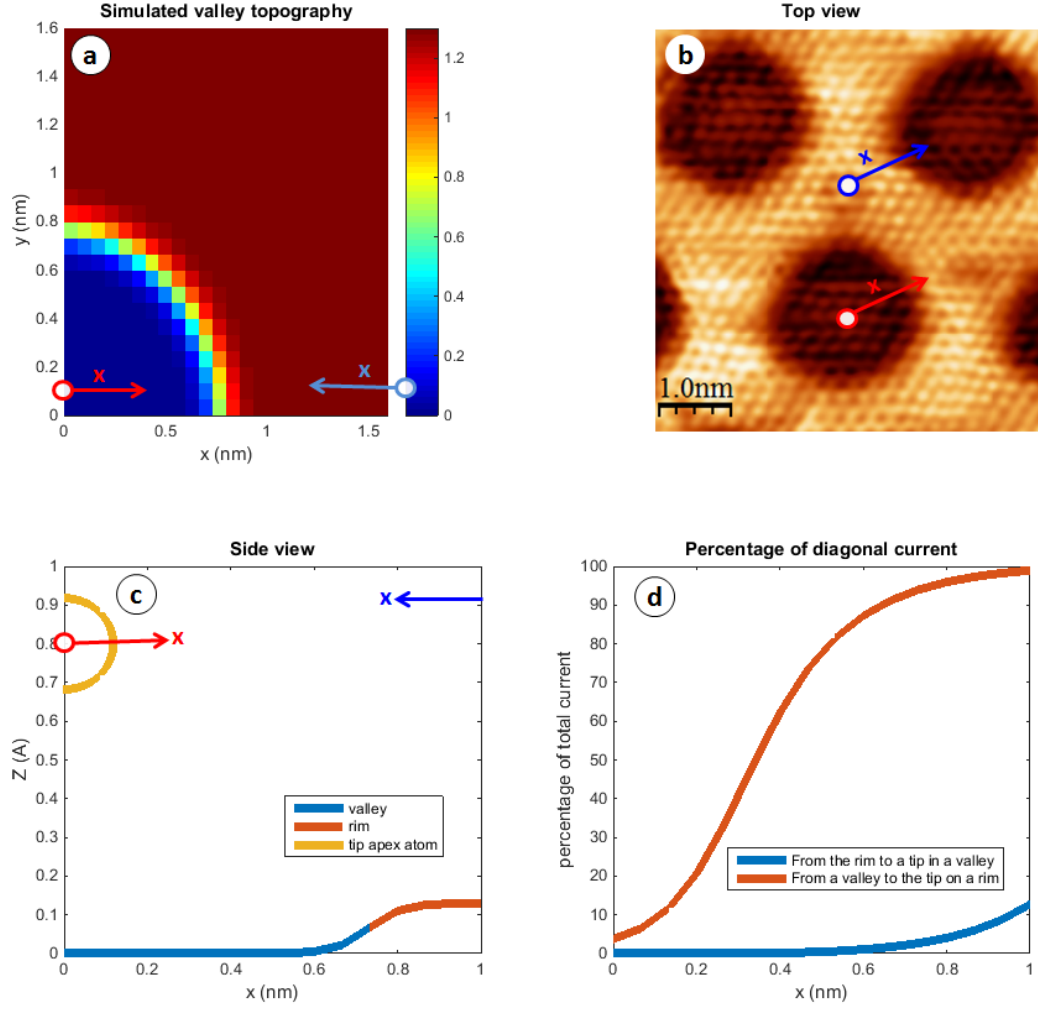


Figure 3.5 – (a) Top view of the simulated valley. Arrows indicate the simulated direction of motion of the tip when moving away from the centre of a valley (blue) and away from a rim crossing (red). **(b)** STM image of h-BN/Rh(111). $V = -2$ V, $i = 10$ pA. Arrows indicate the simulated direction of motion of the tip. **(c)** Side view of the simulated tip and h-BN substrate. The yellow circle represents the apex atom of the tip (the radius of 134 pm corresponds to the metallic radius of Rh [ref]). Arrows indicate the simulated direction of motion of the tip. **(d)** Results of the simulation. Red curve shows the percentage of current incoming from the rim when the tip is on top of a valley, blue curve shows the percentage of current incoming from a valley when the tip is on top of a rim.

The effect of diagonal tunnelling can thus blur WF variations observed in the valleys, even when considering the exponential decay of the tunnel current. Specifically, this leads to a gradual, rather than abrupt, decrease of the observed WF towards the centre of the valley, and the absence of a WF plateau at the bottom of the valley. Moreover, if we consider the finite size of the tip, the WF measured at any point in a valley will be biased towards higher WFs. The

small effect that the valleys have on measurements performed at rims allows WF plateaus on the rims with a narrower distribution of observed WFs (see Figure 3.4e). The final conclusion is that the WF difference between valleys and rims obtained using approach curves is an underestimate. A more accurate estimate may be obtained by a more complete calculation, considering the exact current contributions from distant points in the interpretation of the data.

Anomalies in approach curve maps

Repeated measurements at different areas show that WF maps based on approach curves are susceptible to two kinds of anomalies: topographically "invisible" adsorbates and asymmetric tip artefacts. Invisible adsorbates are adsorbates that manifest themselves in STM topographs by a very small contribution to the apparent height. For example, CO molecules adsorbed on Cu(111) are imaged as depressions with an apparent depth of 10 *pm* [63]. Due to the absence of molecular electronic states available for tunnelling, their presence only affects the scan through their influence on the local DOS of the substrate or the a variation of the local tunnel barrier. Such small variations of contrast are easily visible on the flat surface of Cu(111), but hard to discern in a topographic map of h-BN/Rh(111) due to the 1.3 Å corrugation of the Moiré pattern. Their presence will often lead to some degree of charge transfer from the substrate or to it, depending on the electron affinity of the adsorbate and its interaction with the substrate. Even a small amount of charge transfer leads considerable local WF variations [139] that makes them evident in some WF maps. In Figure 3.6a a few adsorbates are highlighted, which are not visible in the topographic image (Figure 3.6b). Some of the adsorbates cause a WF variation of over 1 *eV*. The second anomaly is caused by tip asymmetry: when the substrate being probed has some degree of corrugation, the tip that is probing it will probe the surface with different facets of the tip (see illustration in Figure 3.6e), depending on the local directional gradient of the surface. This effect is evident by the resemblance of the observed local WF map in Figure 3.6c to the directional gradient of the STM topograph of the same area in Figure 3.6d. This artifact is always present to some extent, but tip shaping can bring the additional contrast to tolerable levels. The strange shape of the tip in this case is already visible in the topographic image (Figures 3.6f).

We conclude that WF mapping using approach curves yields a higher WF on rims than on valleys. The best estimate for the WF difference obtained by this method is 150 ± 80 *meV*, although this should be considered as a lower bound due to the effects of diagonal tunnelling.

3.3.2 FER maps

FERs can be observed by STS as peaks in dz/dV spectra taken at constant current. However, not every peak at a high positive bias corresponds to a FER [88]. The lowest peak observed in the dz/dV spectrum taken on h-BN/Rh(111) (Figure 3.7a) is not a FER but an interface state, localized between the h-BN and the Rh surface. This assignment is likely due to the

3.3. Local work function variations on h-BN/Rh(111)

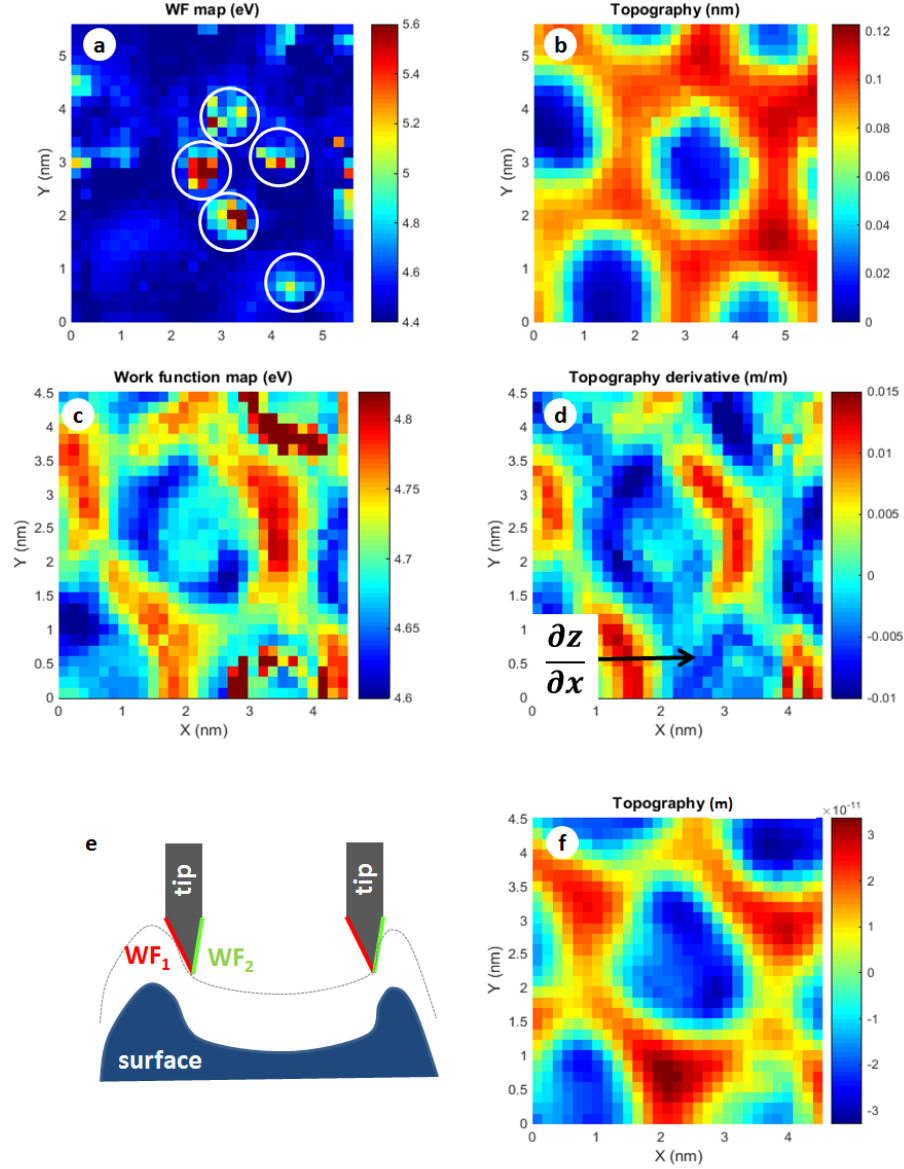


Figure 3.6 – Anomalies in approach curve WF maps. **(a)** Apparent WF map. The strong localized variations in WF (white circles) correspond to adsorbates that are not visible in the STM topograph. **(b)** STM topography corresponding to (a), $V = -2$ V, $I = 10$ pA. **(c)** Apparent WF map taken with a highly asymmetric tip. **(d)** Directional gradient calculated based on (b). Black arrow indicates the direction of the gradient. **(e)** Schematic of asymmetric tip on a corrugated surface. The tip has two facets with different WFs. Both facets contribute to the tunnel current but the ratio varies according to the local directional gradient. **(f)** STM topography corresponding to (c), $V = -2$ V, $I = 10$ pA.

similarities between this peak and the one observed in graphene/Ru(0001) [88]. Its shape is smoother than the FER peaks and it varies very little (30 meV for h-BN/Rh(111)) between

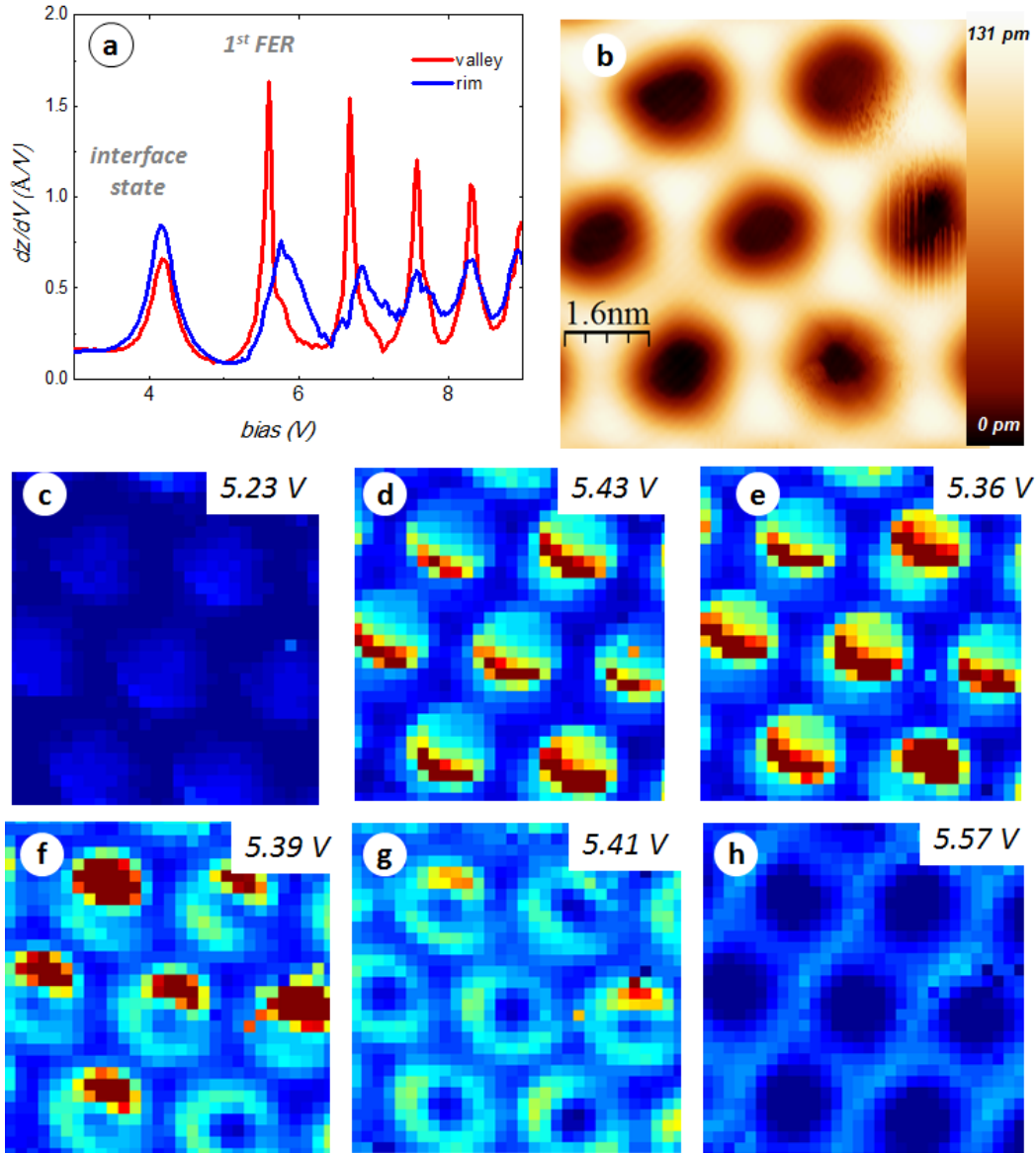


Figure 3.7 – (a) Representative dz/dV curves for a valley and a rim. (b) STM topography at the same area, $V = -2$ V, $I = 10$ pA. (c-h) energy cuts from the grid of spectra. An apparent WF variation inside the valleys is attributed to a tip asymmetry artefact.

valleys and rims. The small variation that is observed is not due to WF differences, it is rather the effect of the proximity of the adlayer to the metal. In the graphene/Ru(0001) system, the proximity of the graphene layer to the Ru substrate increases the energy of the interface state [88], therefore this peak is found at slightly higher energies where the graphene is closer to the metal. Similarly, the interface state of h-BN/Rh(111) is found at a slightly lower energy on the rims than on the valleys. Therefore, we address the second peak of the dz/dV spectra as the first FER.

To map FERs, a grid of points is defined on an area of h-BN (depicted in Figure 3.7b), and at each point of the grid the bias is ramped between 5.2 – 5.6 V (spanning the first FER) while keeping the current constant ($I = 20 \text{ pA}$) using a feedback loop. The dz/dV curves spanning the first FER are arranged in a matrix and used to produce a dz/dV map for each bias value. The maps are assembled into movies where they are displayed at a gradually increasing bias, and a few snap shots from such a movie are displayed in Figure 3.7a-f. An immediately striking feature of these movies is the appearance of a front of FER peaks "moving along the valleys" from the bottom left towards the top right of the valleys in Figure 3.7c-h. This is merely a more dramatic manifestation of the asymmetric tip artefact already observed in the approach curve maps. The sharpness and intensity of the FER peaks inside the valleys makes it possible to better quantify this artefact in this measurement. Assuming that the WF is constant inside each valley, the apparent WF variation in the valley constitutes an estimate of about 30 meV for this artefact (see Figure 3.7e and f). At higher voltages (Figure 3.7f and (g) rings appear around the valleys, and at a higher bias (Figure 3.7h) the rims brighten up uniformly.

FER standing waves inside valleys

The observation of a FER peak at a higher bias on the rims than on the valleys can be expected from the previously found lower WF in the valleys [2]. The appearance of rings around the valley centres (Figure 3.7e and (f) suggests that the potential well, experienced by FER electrons at the valleys due to their lower work function, is deep enough to sustain a second standing wave mode. A circular potential well can sustain several electron eigenstates, similar to the beats of a drum [140]. The states can be described by two quantum numbers n and m , and the resulting wavefunction $\psi(n, m)$ is

$$\psi(n, m) \propto J_m\left(\frac{r}{r_m^n}\right) \cdot \sin(m\phi) \quad (3.10)$$

which is the product of J_m , the m th Bessel function in the radial direction (r), truncated at its n th zero (r_m^n is the n th zero of the m th Bessel function), multiplied by a sinus function in ϕ , the azimuthal coordinate. n is similar to the principal quantum number in the hydrogen atom problem [140], describing the number of nodes in the radial axis (including the perimeter). m is similar to the angular momentum in the hydrogen atom problem, and describes the number of nodes in the azimuthal dimension. The $n = 1, m = 0$, or (0,1) mode, is the mode with the lowest energy in this system (plotted in Figure 3.8a). It is characterized by a single maximum at the centre of the well and no nodal diameters. This mode can be identified as the dominant, sharp dz/dV peak observed in Figure 3.7e inside the valleys and peaking at their centre. A zoom-in of a dz/dV map of one of the valleys at a voltage corresponding for the (0,1) mode is also shown in Figure 3.8b. Due to the sharpness of this peak and to a small spread of the peak position inside the valley, there is no single bias voltage where this state is observed across the entire valley. Instead, a "wavefront" corresponding to this state travels

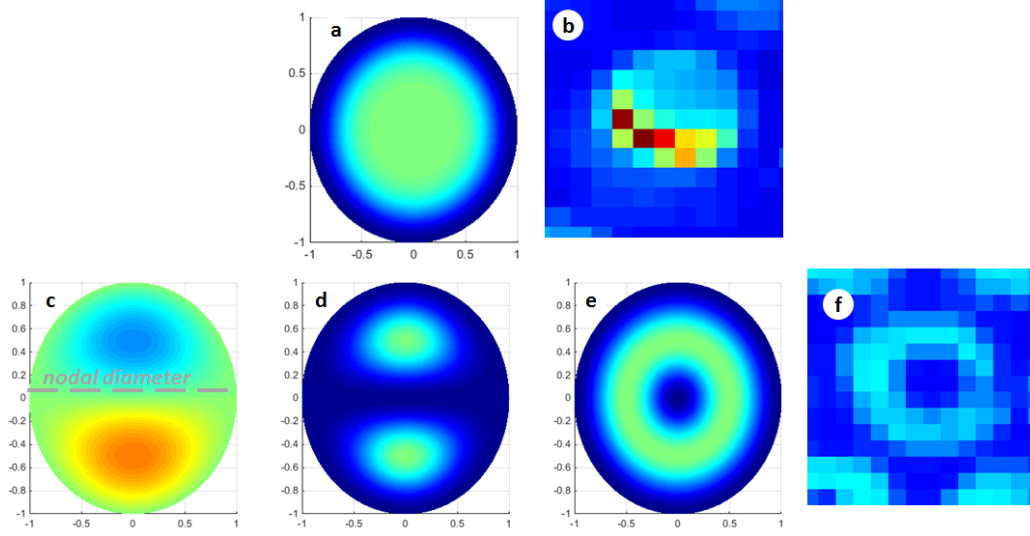


Figure 3.8 – Eigenstates of a free electron in a circular 2D potential well. **(a)** Amplitude of the (0,1) mode of a free electron in a circular 2D potential well. **(b)** Zoom-in from Figure 3.7e. A dz/dV map of a single valley ($3.2 \times 3.2 \text{ nm}$) at $V = 5.36 \text{ V}$, $I = 10 \text{ pA}$. The bright (red) points correspond to the peaks of the (0,1) mode. **(c)** Amplitude of the (1,1) mode of a free electron in a circular 2D potential well. The nodal diameter is marked with a dashed line. **(d)** Squared amplitude (or probability density) of the (1,1) mode. **(e)** Squared amplitude of the (1,1) mode, averaged over all possible orientations of the nodal diameter. **(f)** Zoom-in from Figure 3.7g. A dz/dV map of a single valley ($3.2 \times 3.2 \text{ nm}$) at $V = 5.41 \text{ V}$, $I = 10 \text{ pA}$. The bright (turquoise) ring corresponds to the peaks of the (1,1) mode.

across the valley over a bias range of 30 mV . The next standing wave mode in a disc is the (1,1) mode, with two peaks of opposite sign at the opposite sides of the disc, and a nodal diameter (Figure 3.8c). The squared amplitude of this mode (which corresponds to the probability density) shows two peaks, as in Figure 3.8d. However, this is not how we should expect this mode to look like in this experiment. When tunnelling into the FER states of the valley, each tunnelling electron may tunnel into a state with a different nodal diameter, as they are all energetically equivalent. The pattern we should expect to see is the (1,1) mode averaged over all the possible orientations of the nodal diameter. This averaging turns the nodal diameter into a single nodal point at the centre, plotted in Figure 3.8e¹. This state is the origin of the rings observed in the dz/dV maps such as Figures 3.7g. A zoom-in of one valley from this image is presented in Figure 3.8f.

The existence of two standing wave modes of the first FER inside the valleys of h-BN explains why two peaks are observed in dz/dV spectra measured inside the valleys (Figure 3.9a, red and green curves). The observation of two peaks in spectra taken on the rims can be explained as due to the spillover of FER states. It has been observed that laterally localized FER states

¹This azimuthal averaging is also the reason why only circular nodes are observed in the famous quantum corrals first observed by Crommie et al. [61], provided that the corral is circular.

are measurable when the tip is up to 1 nm away from the structure which gives rise to the FER [101, 102]. This observation is important for the assignment of peaks to states. In a naive assignment, the FER peak position is determined using the point of highest intensity in each dz/dV spectrum. This naive assignment gives the peak position map in Figure 3.9c. In this map the areas with the lowest peak positions are well correlated with the positions of the valleys in the topographic image of the same area (Figure 3.9d²). The valleys are surrounded by rings, $\approx 6.5\text{ \AA}$ in width, with slightly higher peak positions. A few patches, at a safe distance from the valleys, show a significantly elevated peak position. In order to understand the influence of the valley FERs on measurements performed on the rim, we turn to a more detailed analysis of the dz/dV spectra.

Fitting procedure and results

Each dz/dV spectrum was fitted to the sum of two Gaussian functions. The fitting procedure was successful for most spectra, but yielded poor results on the extremely sharp peaks observed at the valleys, with $R^2 < 0.8$ at these positions (see Figure 3.10a). Therefore, for all the curves where $R^2 < 0.8$, the lower peak position was determined to be the position of the maximal value of the dz/dV spectrum. Henceforth we refer to the peak centred at a lower bias as "the lower peak" and the peak centred at higher bias as "the higher peak". Figures 3.10b and c show maps of the lower peak bias and the higher peak bias in the dz/dV spectra, respectively.

The lower peak map (Figure 3.10b) shows the lower peak position slightly decreases in energy when moving from the valley's center towards the peripheral region of the valley, while the rims present a significantly elevated and uniform peak position. According to the interpretation presented earlier, the low peak positions observed on the valleys ($V < 5.4\text{ V}$) correspond to the (0,1) FER mode of the valley. This mode is too far away to be observed when the tip is on the rim, therefore the lowest peak observed on the rim is the (1,1) mode, with peaks at $5.5\text{ V} > V > 5.4\text{ V}$. The decrease of the (0,1) mode's energy towards the valley's periphery by up to 40 meV can be explained by a reduced Stark shift of this mode. The (0,1) mode is less affected by the electrical field of the STM tip when the tip is away from the centre of the valley, therefore its energy is lower. This hypothesis is based on the gradual decrease of the peak position towards the valley's periphery (Figure 3.10b). The (1,1) peak is similarly observed at an energy reduced by 40 meV when it is measured by a tip positioned on the rim (Figure 3.9a). The energy at which the (1,1) mode is observed is similar whether the tip is in the centre or the periphery of a valley (Figure 3.9a), reflecting the close proximity of the tip to this state in both cases. In Figure 3.10c, the higher peak position is highest on the rims ($V > 5.5\text{ V}$), lower at the peripheral region of the valleys, and noisy at the centres of the valleys, due to the poor success of the fitting routine with these spectra. In this map, the peak position measured on the rims represents the FER states of the rims, while the peak position measured at the peripheral region of the valleys represents the (1,1) mode of the valleys.

²The colour palette was inverted because the image, scanned at $V = +5.4\text{ V}$, presents a contrast inverted compared to STM images taken at low bias.

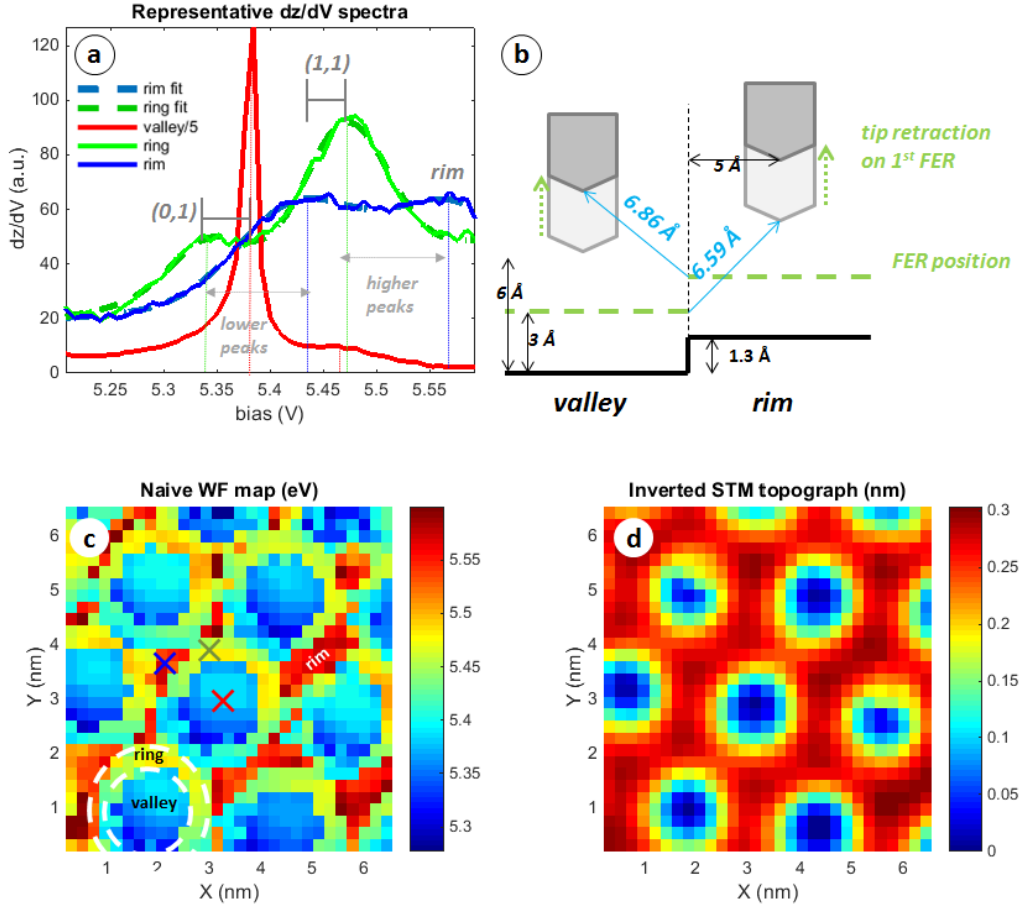


Figure 3.9 – (a) Selected dz/dV spectra taken at a valley, a ring and a rim. The positions where the spectra were taken are marked with corresponding color in c. The spectrum measured in the valley is divided by 5 for clarity. Fits to a sum of two Gaussians are in dashed lines. (b) Schematic of tip position and relevant dimensions during the acquisition of a dz/dV curve. c) Map of first FER peak position. (d) STM topograph of the same area. z values were inverted for clarity. $V = +5.45$ V, $I = 20$ pA.

Having concluded the assignment of peaks to FER states, we proceed to classification of valleys and rims. We note that rim regions present an elevated FER peak position (red patches in Figure 3.10c) of above 5.5 V, clearly distinguishable from their surroundings. We therefore use a modified selection algorithm to distinguish between valleys and rims. In addition to the topographic criterion, we demand that the higher peak appear at above 5.5 V for rim pixels. The resulting selection mask is presented in Figure 3.11a. The histogram of peak positions derived separately from valleys and from rims is presented in Figure 3.11b. The histograms are fitted to Gaussian functions (dashed lines in Figure 3.11b). The gap between the peaks of the Gaussians provides an estimate of the work function difference between valleys and rims of 195 ± 30 meV.

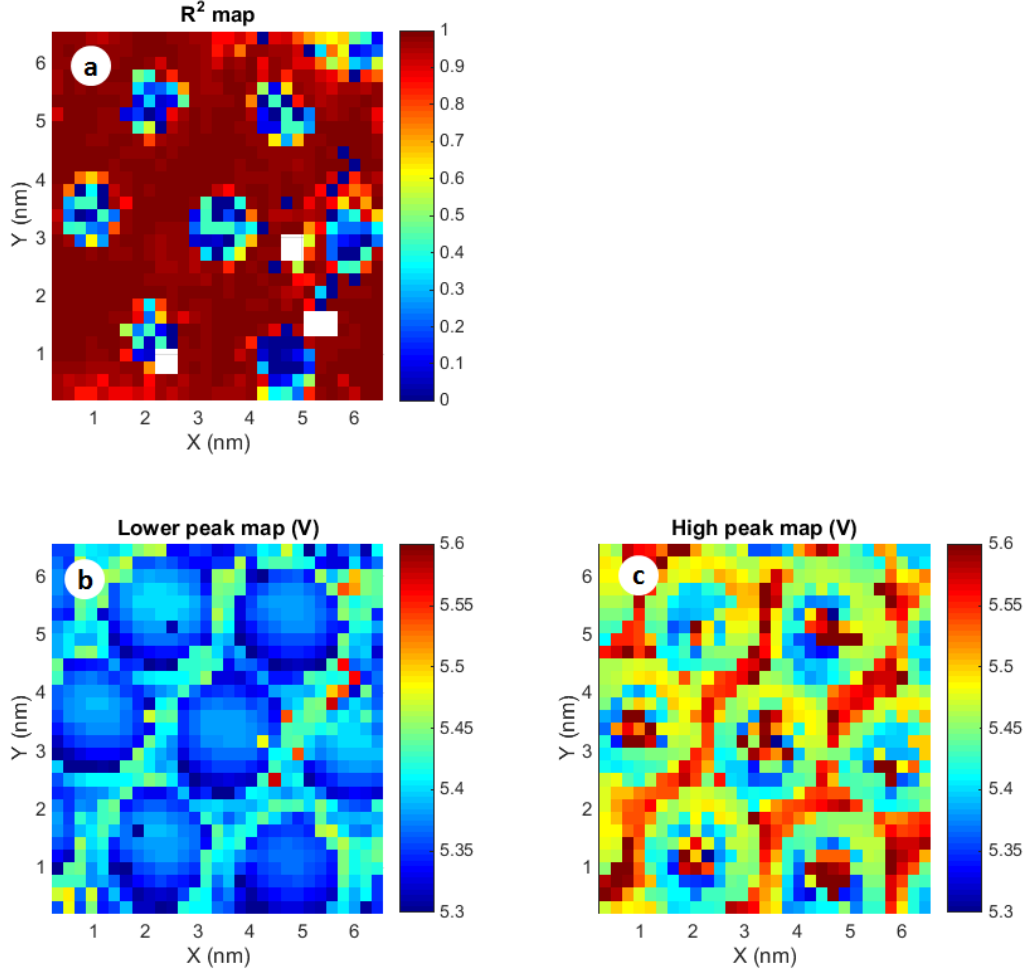


Figure 3.10 – (a) Map of R^2 . (b) Map of lower energy peak position. (c) Map of higher energy peak position.

So far, the observation of two peaks in each spectrum has required an explanation and an additional effort in the analysis of the data. We can, however, "turn this lemon into lemonade" and use it to our advantage. The analysis we did in the previous section is akin to evaluating the difference between two random variables by subtracting their averages. The fact that in every spectrum we have two peaks means that we can do the subtraction for every individual spectrum, rather than for the averages. We thus neutralize artefacts that shift the two peaks by the same amount, such as tip asymmetry. We can do this by plotting a two dimensional histogram of FER peak positions, where the colour of a point at (V_{low}, V_{high}) corresponds to the number of spectra that present the lower FER peak at V_{low} and the higher peak at V_{high} (Figure 3.11c). For valley spectra we expect

$$V_{high} = V_{low} + \frac{1}{e} \left(E_{(1,1)}^{valley} - E_{(0,1)}^{valley} \right) \quad (3.11)$$

Chapter 3. Local work function variations of hexagonal boron nitride on metal surfaces

where $E_{(1,1)}^{valley}$ and $E_{(0,1)}^{valley}$ are the energies of the (1,1) and (0,1) modes of the valley. Similarly, for spectra measured on the rims we expect

$$V_{high} = V_{low} + \frac{1}{e} (E^{rim} - E_{(1,1)}^{valley}) \quad (3.12)$$

where E^{rim} is the energy of the FER states on the rim. Equations 3.11 and 3.12 indicate that, for each population of points, V_{high} can be fitted to V_{low} by a linear fit with slope 1, and the intercept will give the difference between the two peak, free of artefacts related to tip asymmetry. The section of the 2D histogram in Figure 3.11c below the dashed white line corresponds to valley positions. The values of V_{low} were averaged for each value of V_{high} , giving a curve plotted in blue in Figure 3.11d. This curve was fitted to a linear function with slope 1, and the intercept of the linear fit for these points gives the energy difference between the (1,1) and the (0,1) modes of the valley, $115 \pm 10 \text{ meV}$. The top part of the plot includes the spectra taken on the rims, and the intercept of the similarly fitted linear curve gives the energy difference between the (1,1) mode of the valleys and the FER peak on the rims, $143 \pm 10 \text{ meV}$. The WF difference between the rims and the valleys can be estimated by summing the two, yielding an estimate of $258 \pm 14 \text{ meV}$.

Discussion

dz/dV mapping at the voltage range on the lowest FER shows that the potential well inside the valleys can sustain the (1,1) standing wave mode of the FER electrons in addition to the ground state (0,1). Due to the small distance between valleys and the small potential corrugation, it is most likely that the FER states in neighbouring valleys are sufficiently coupled that these states form a quasi-free electron like band. Such coupling between partially localized IPSs has been observed in Fe Phthalocyanine molecules (FePc) on Ag(111) [114] and in graphene/Ru(0001) [109]. Angle resolved 2PPE measurements could determine the energy-momentum dependence in these bands, the effective mass and whether band folding occurs.

Relying on our assignment of the peaks, fitting each spectrum to a sum of two Gaussians allows one to analyse the map in two ways. One way is to fit the histograms of peak positions on valleys and on rims separately, yielding a difference in peak position of $195 \pm 30 \text{ mV}$. This result is in qualitative agreement with previous measurements [2] and with the results of the approach curve map. It yields a higher value than the approach curve maps, which is a good sign as we know that the approach curve maps yield an underestimate of the WF variation. However, a 2D histogram of peak positions reveals linear trends, indicating a constant difference between the two peak positions. The difference is found to be $115 \pm 10 \text{ mV}$ in the valleys and $143 \pm 10 \text{ meV}$ on the rims, which suggests a WF difference of $258 \pm 14 \text{ meV}$ (the difference between the lowest FER in the valleys and the lowest FER on the rims). The drawback of the first method is that it is more sensitive to a biased sample, for example if a few valleys presented a relatively high peak position this would distort the histogram and thus the

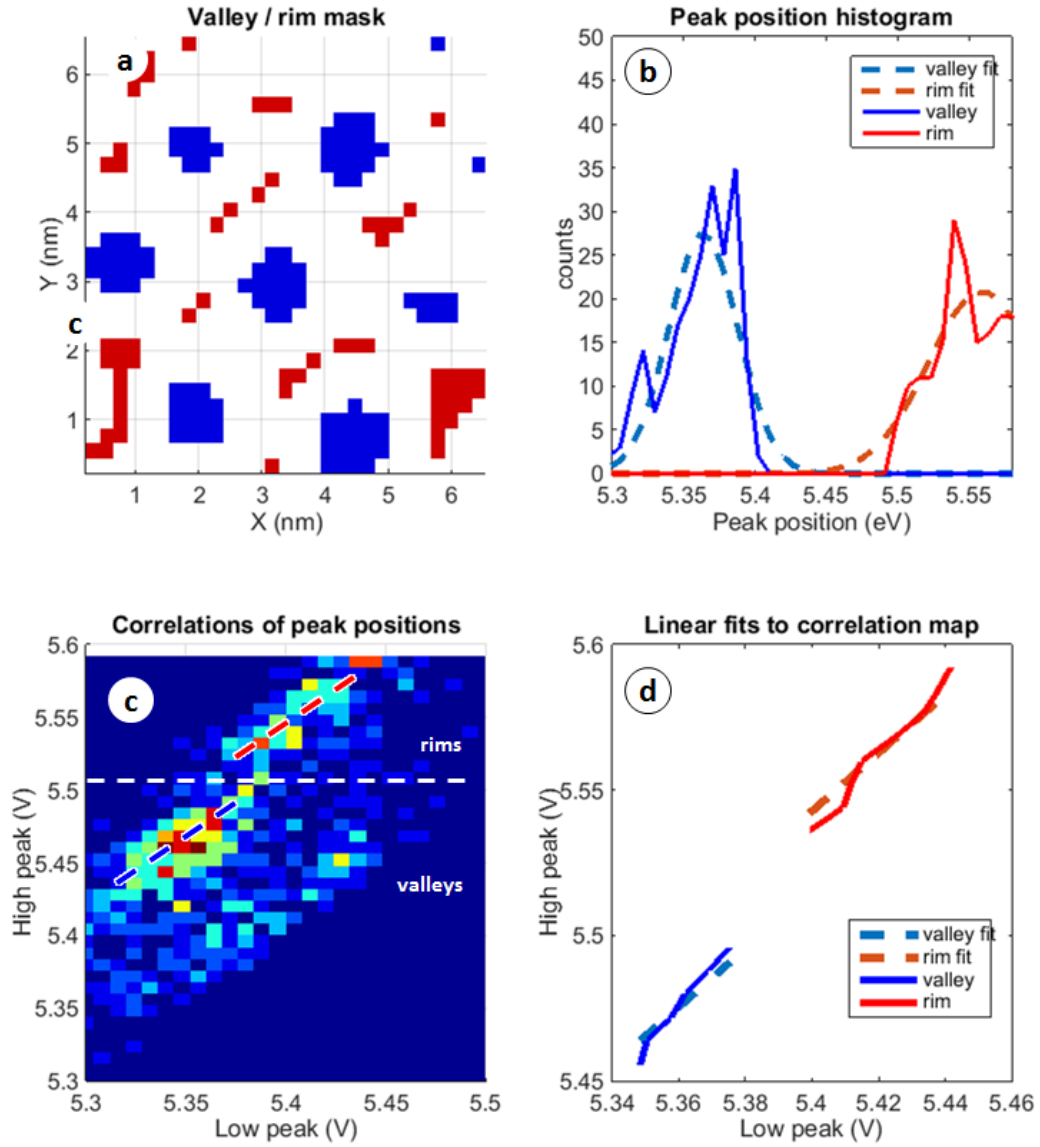


Figure 3.11 – (a) Mask used to distinguish between valleys and rims. (b) Histogram of peak positions for dz/dV spectra measured on valleys (blue solid line) and rims (red solid line). Corresponding Gaussian fits are in dashed lines. (c) 2D histogram of FER peak positions. The colour of a point at (V_x, V_y) corresponds to the number of spectra that present the lower FER peak at V_x and the higher peak at V_y . (d) Weighted average per row (from (c)) fitted to linear functions with slope 1. Pore positions in solid blue line and rims in solid red line. Fits are presented in dashed lines of corresponding colours.

WF difference estimate. In the second method, on the other hand, the separation of peaks is evaluated for each spectrum individually. This analysis is made possible thanks to the spillover, and shows how an unexpected experimental complication can turn to our advantage using

the proper analysis.

An alternative hypothesis as to the origin of the ring shaped states should also be mentioned. While measuring FER states on Li islands on Cu(100), Stepanow et al. [103] observed that some of the resonances displayed a circular shape while other a ring shape. The ring-shaped resonances were ascribed to states arising from the mixture of (0,3) standing wave modes of the Li islands with FER states of the Cu. As a result of this mixing, these resonances appear at slightly reduced energies with respect to their corresponding Cu surface states. In our case, the ring shaped resonances may be the result of the mixing between the (0,3) states of the valley and the FER band on the rims. The difficulty with this explanation is that it requires the (0,3) state of the valley to be found approximately 115 *meV* from the (0,1) state, as opposed to nearly 1 *V* in [103]. Since the structures discussed in this case are smaller, the energy gap between the (0,1) and the (0,3) states should be even larger.

3.3.3 KPFM maps

The third technique applied is KPFM. We defined a grid of points on the surface, and at each point the tip position is stabilized by tunnel current feedback. At this position, the bias is ramped from -2 *V* to -0.5 *V* and the frequency shift (proportional to the oscillating component of the force experienced by the cantilever) is recorded. A few of these curves are shown in Figure 3.12a. The data is analysed using a Matlab script which performs a second degree polynomial fit for each curve and extracts the maximum of the $F_\omega(V)$ curve. Additional forces create an offset of the entire curve therefore $F_\omega(V_{CPD})$ does not equal zero at $V_{DC} = V_{CPD}$, as in Equation 3.9, but rather has a maximum at V_{CPD} .

In this map only a small area was scanned, containing one valley and one rim junction. A zoom out of the area is presented in Figure 3.12b, where the grid of measurements is indicated. The measured CPD map (Figure 3.12c) presents values that vary by 70 ± 10 *meV*. The topographic image (Figure 3.12d) is somewhat distorted due to piezo creep during the acquisition of the map, but areas of high WF roughly correspond to areas of high topographic altitude, qualitatively in agreement with the approach curve maps and the FER maps. Unfortunately, KPFM cannot reach the lateral resolution of STM techniques because it relies on long range interactions (electrostatic forces). The result is a weighted average over the size of the tip, typically 10 – 20 *nm*, leading to an underestimation of the WF difference by a factor which depends on the tip size, the lateral scale of WF variations and on the oscillation amplitude [141]. We can nevertheless distinguish the areas of higher WF from areas of lower WF.

3.3.4 Discussion

STM based local WF variation mapping techniques can help resolve the current discrepancy between the previously published experiments and DFT calculations [3], which will now be described in detail. SPM based measurements could be expected to provide a high resolution

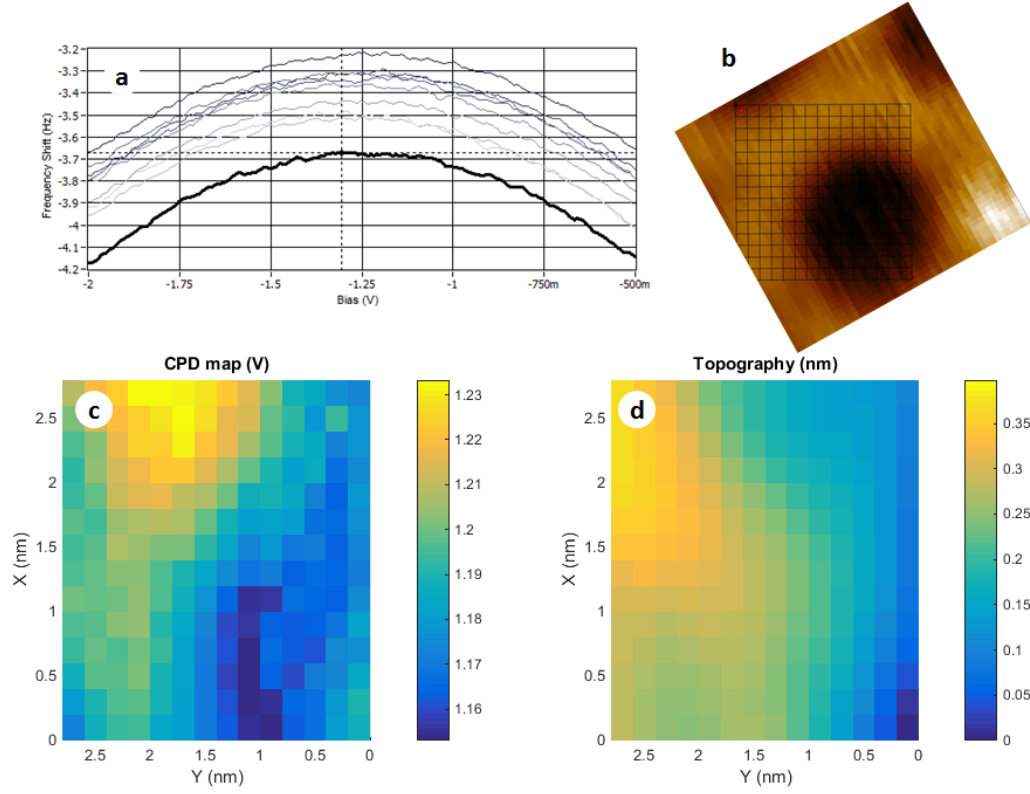


Figure 3.12 – (a) Examples of frequency shift vs. bias plots. (b) STM topograph of the area, the grid used for the KPFM map is indicated. , $V = +50 \text{ mV}$, $I = 50 \text{ pA}$. (c) Local CPD map measured at 1.2 K. Oscillation amplitude is 50 pm. (d) STM topography measured during KPFM mapping, $V = -2 \text{ V}$, $I = 50 \text{ pA}$.

measurement of local WF variations. KPFM performed at low temperature yields a result of 70 meV, significantly lower than all other techniques. KPFM cannot provide the resolution required in this experiment due to the use of the tip as a capacitor, not as a tunnelling probe. Surprisingly, even tunnelling based techniques, such as approach curve mapping, yields a WF variation underestimate of 150 meV. This is due to the combination of the strong electronic corrugation of h-BN/Rh(111), small lateral dimensions of the WF variation pattern and small WF variations (6 – 10% of the WF). Specifically, in the approach curve mapping technique, the diagonal tunnelling current, that accounts for 10% of the current, leads to smearing and a WF difference underestimate of unknown magnitude. However, in the FER mapping technique diagonal tunnelling can be turned into an advantage, allowing to compare peak positions in every single spectrum and not only comparing peak position averages. Consequently, this technique yields a WF variation of $258 \pm 14 \text{ meV}$, the same result as the one observed by Dil *et al.* using photoemission [2], detailed in Table 3.1.

Chapter 3. Local work function variations of hexagonal boron nitride on metal surfaces

Table 3.1 summarizes local work function variations of h-BN/Rh(111) predicted using DFT [3, 2], measured using photoemission of adsorbed Xe [2], KPFM at room temperature [141] and the results of the present work.

| Method | WF variation | Reference | Comments |
|---------------------------|--------------------------|--------------|---|
| Approach curves | $150 \pm 80 \text{ meV}$ | present work | Underestimate due to diagonal tunnelling. 5 K. |
| FER peaks | $258 \pm 14 \text{ meV}$ | present work | Best estimate provided by peak position correlation map. 5 K. |
| KPFM | $70 \pm 10 \text{ meV}$ | present work | 1.2 K. |
| Adsorbed Xe photoemission | 310 meV | [2] | 260 meV when taking into account final state screening. 63 K. |
| DFT | 300 meV | [2] | 1×15 Rh slab |
| DFT | 500 meV | [2] | $12 \times 12 \times 3$ Rh slab |
| DFT (revPBE) | 760 meV | [3] | $6 \times 6 \times 7$ Rh slab |
| DFT (revPBE) | 450 meV | [3] | $12 \times 12 \times 7$ Rh slab |
| KPFM | 16 meV | [141] | Room temperature. |

Table 3.1 – Calculated and measured WF variation of h-BN/Rh(111) in these experiments and in previously reported ones.

KPFM maps on h-BN/Rh(111) were performed by Koch et al. [141] at room temperature, obtaining a WF variation of $\approx 16 \text{ meV}$. One reason for this small value is, as in our KPFM measurements, averaging over a few Moiré unit cells due to the size of the AFM tip. Additional factors of the underestimate are the increased temperature and the oscillation amplitude of 10 nm , which further contribute to the averaging effect.

Dil et al. [2] describe adsorbed Xe photoemission experiments in which Xe was adsorbed onto a cooled h-BN/Rh(111) surface at 63 K. Since Xe adsorbs weakly to the h-BN, its distance makes for a very weak electronic coupling to the substrate therefore its electronic states are pinned to the vacuum level rather than to the Fermi energy. The photoemission experiment showed that two work functions were present on the surface, separated by 310 meV . Based on DFT, the higher work function was assigned to the rims and the lower one to the valleys. However, Dil et al. suggest that correcting these results for final-state screening would bring the estimated WF difference to 260 meV . This result is in excellent agreement with the result obtained from FER maps of $258 \pm 14 \text{ meV}$, and substantially lower than the ones predicted by DFT in the same paper.

The DFT calculations reported in [2] were not conclusive as they yielded different results depending on the unit cell that was used. One calculation was performed with a lateral unit cell of 12×12 Rh atoms, including the full Moiré pattern, but due to the lateral extension of this unit cell only 3 layers of Rh were included. This calculation yielded WF variations of 500 meV . In the second calculation, the lateral unit cell included a smaller area but contained 15 layers of Rh. Since this cell is too small to reproduce the full Moiré pattern, the sheet of h-BN was

artificially placed at the distance, registry and B-N bond length corresponding to rims and valleys respectively. This calculation yielded a WF variation of 300 *meV* between rims and valleys.

It is interesting to compare these results to similar calculations performed later by Gomez-Díaz et al. [3] using a revised Perdew–Burke–Ernzerhof functional (or revPBE) and dispersion forces. As in [2], the WF variations were compared between a full Moiré unit cell and a reduced Rh slab with an artificially positioned h-BN sheet. In this case the full Moiré slab produced a WF variation of 450 *meV* compared with the reduced slabs, which produced a WF difference of 760 *meV*. The absence of a clear trend with respect to the number of Rh layers indicates that it is not the deeper layers of Rh which affect the WF variation. The discrepancies might be due to the exact altitude and positioning of the N and B atoms with respect to the underlying Rh atoms. This lays a heavy burden on DFT of accurately accounting for dispersion forces which dominate in this system of a loosely bound layer. It is for this reason that accurate and reliable experimental results are needed. We have shown that, contrary to expectations, the precision of approach curve mapping suffers from diagonal tunnelling in this highly corrugated system. In the FER mapping technique, on the other hand, the same effect can be harnessed to overcome the effects of averaging over biased samples. This method gives a WF variation estimate of 258 ± 14 *meV*, in good agreement with measurements based on photoemission.

3.4 Effect of lateral localization on FER lifetimes

An interesting observation from the FER maps is that FER peaks in dz/dV are not only shifted in energy between valleys and rims, but also significantly more intense and narrow inside the valleys. Figure 3.13 shows an analysis of a FER map with higher energetic and lateral resolution than Figure 3.9. Figure 3.13a is a map of FER peak position, which shows the same characteristics observed in Figure 3.9a. Figure 3.13b shows the peak intensity at each point of the grid (the maximal value of the dz/dV curve). It shows how the intensity of the FER peak is over 10 times higher inside the valleys than outside. Three representative dz/dV curves are plotted in Figure 3.13d. The full width at half maximum (FWHM) of each peak was calculated by counting the number of points per curve whose intensity is higher than half the maximal intensity of the curve. The result, plotted in Figure 3.13c, shows how the peak width drops from the range of 270 meV on the rims down to below 50 meV inside the valley. Fitting the red curve displayed in Figure 3.13d yields a width of 8 meV . Defining the peak width as Γ and using the equation [98]

$$\tau_{FER} = \frac{\hbar}{2\Gamma} \quad (3.13)$$

this peak width corresponds to an upper bound of $\tau_{FER} = 250$ fs for the lifetimes of FERs in valleys. FER lifetimes observed in STM are known to be half or less compared to the unperturbed lifetimes of IPSs, due to the strong electrical fields present in the tunnel junction [96] and to the changing geometry of the tunnel junction during the measurement [98]. The unperturbed lifetimes of IPSs inside the valleys can therefore be expected to be twice longer than the lifetimes of IPSs measured on flat h-BN layers on Ni(111) [142].

FER lifetimes in h-BN/Cu(111) and analogous systems

In order to question the generality of extended FER lifetimes in laterally confined FERs, we performed the same experiment on a similar system consisting of a monolayer of h-BN on Cu(111). STM measurements of this layer at +3 V (see [143] and Figure 3.14a) have shown various Moiré patterns with variable unit cell sizes varying between 5 – 15 nm on different h-BN domains. DFT calculations suggest [144] that the corrugation observed in STM images is entirely due to local WF variations, the brighter areas corresponding to regions where the bias voltage matches the first FER. According to these calculations, the h-BN layer is geometrically flat, but the amount of charge transfer varies with the local registry between the h-BN layer and the substrate. The different Moiré patterns are due to the different possible orientations of the h-BN layer with respect to the metallic substrate. WF variations on this layer have been observed by STM techniques [81], however variations in intensity and width were not discussed.

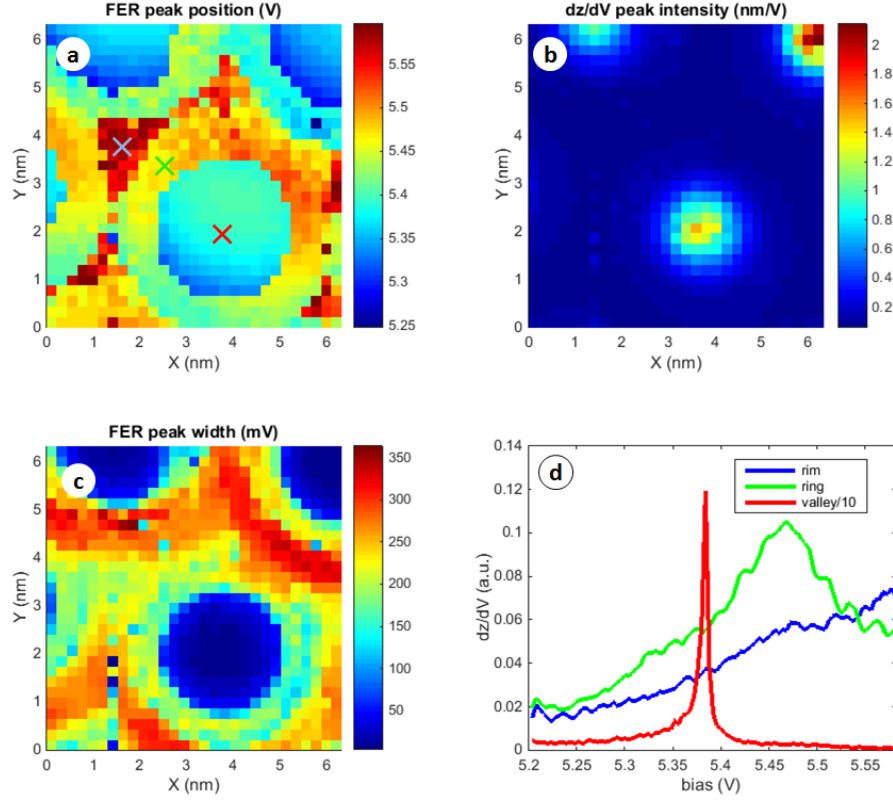


Figure 3.13 – (a) FER peak position map. (b) FER peak intensity map. (c) Map of FER peak width. Although the FER peak position map suggests an irregular tip, this is the only dataset where the energy resolution is sufficient to estimate the widths of the sharpest peaks, with a minimal width of 8 *meV*, corresponding to a lifetime of 250 *fs*. (d) Representative dz/dV spectra taken on a valley, a ring and a rim. The spectrum measured in the valley is divided by 10 for clarity. The positions where the spectra were taken are indicated in (a).

Figure 3.14b shows multiple dz/dV spectra taken along a path which crosses several valleys (the path is represented in the inset). Representative spectra are shown in Figure 3.14c. The trends observed in h-BN/Rh(111) are observed here as well: FER peaks on valleys are 250 *meV* lower in energy than on rims. The peak width is smaller inside the valley (250 *meV*) than on the rim (500 *meV*), and the intensity is 30% lower on the rims. FERs measured on the bare Cu(111) surface are even broader (700 *meV*), higher in energy (600 *meV* higher than on the valleys) and less intense (50% lower than on valleys). Compared with other systems where WF variations occur on the nanometre scale, similar trends can be observed in NaCl/Ag(100) [145], h-BN/Ir(111) [111], FeO/Pt(111) [107], and gr/Ru(0001) [88], all of which exhibit a Moiré pattern due to lattice mismatch between the underlying metal and the dielectric film on top. In the following we discuss some properties of FERs that might account for the observed trends.

Discussion

In the examples given above ([145, 111, 107, 88]), FERs are confined into periodic structures because the electron potential in these arrays is lower than on the surrounding areas. FERs on the rims are partially confined to the rim network because scattering into the valleys is possible only through an inelastic process. The rims, however, provide an extended network for the FERs to propagate and can therefore sustain delocalized states, while in the valleys there is a stronger tendency for localization. As a result, FER peaks measured at valleys are not broadened due to summation over momenta and moreover, the states observed in the valleys have zero momentum and therefore the longest lifetimes. We therefore propose that quantum confinement in the lateral directions is the main reason for the increased lifetime observed inside the valleys of h-BN/Rh(111) and the additional mentioned systems [145, 111, 107, 88]. The effects of FER localization have been previously considered in the context of its effect on the FER energy [97] and the appearance of standing waves [102]. Lifetimes have only been addressed by 2PPE.

Two systems bearing similarities to h-BN/Rh(111) have been studied with 2PPE and can provide some insight: h-BN/Ni(111) [142] and graphene/Ru(0001) [109]. Lifetimes of IPSs on h-BN/Ni(111) of 261 fs were measured by Muntweiler et al. [142]. They are attributed to the fact that the lowered WF of the h-BN covered Ni brings the first IPS to the centre of the surface projected bandgap, thus decreasing the IPS coupling with the bulk. The dielectric layer seems however to play an additional role in decoupling IPSs from the bulk, as long lifetimes (155 fs) have also been observed on heptane layers on Ag(111) [146]. A corrugated dielectric thin film on top of a metal can be found in graphene/Ru(0001), which has also been studied with 2PPE by Armbrust et al. [109]. The corrugation of this layer is reversed with respect to h-BN/Rh(111): the graphene sheet forms a chicken-wire shaped network of valleys, which surround less strongly bound graphene hills. Surprisingly, the IPS band localized on top of the hills shows a shorter lifetime of 11 fs compared with 16 fs of the band delocalized on the valleys. The *reduced* lifetime in the localized hills is ascribed to the different binding energies of these states with respect to their local vacuum levels. Due to the corrugation of graphene on Ru(0001), the IPSs at the hills find themselves *under* the sheet of graphene, and pushed downwards towards the metal, by the graphene. Such an effect would not be expected in h-BN/Rh(111) as the localized states occur under the lower regions of the dielectric sheet. Regardless of the effects of localization, the order of magnitude difference between the lifetimes of IPSs on h-BN/Ni(111) and graphene/Ru(0001) is noteworthy.

The prolonged lifetime may however be explained by an alternative mechanism related to the overlap between the FER wavefunction and the bulk. In all the systems mentioned above as displaying similar trends [145, 111, 107, 88], the FER energy inside the valleys was observed to be lower than on the rims. The lower energy is the result of a dipole layer pointing towards the surface (a schematic of this idea is presented in Figure 3.15). The electrical field associated with this dipole works to push electrons outwards. A FER present inside a valley would therefore experience a stronger force pushing outwards, and its centre of mass would therefore lie

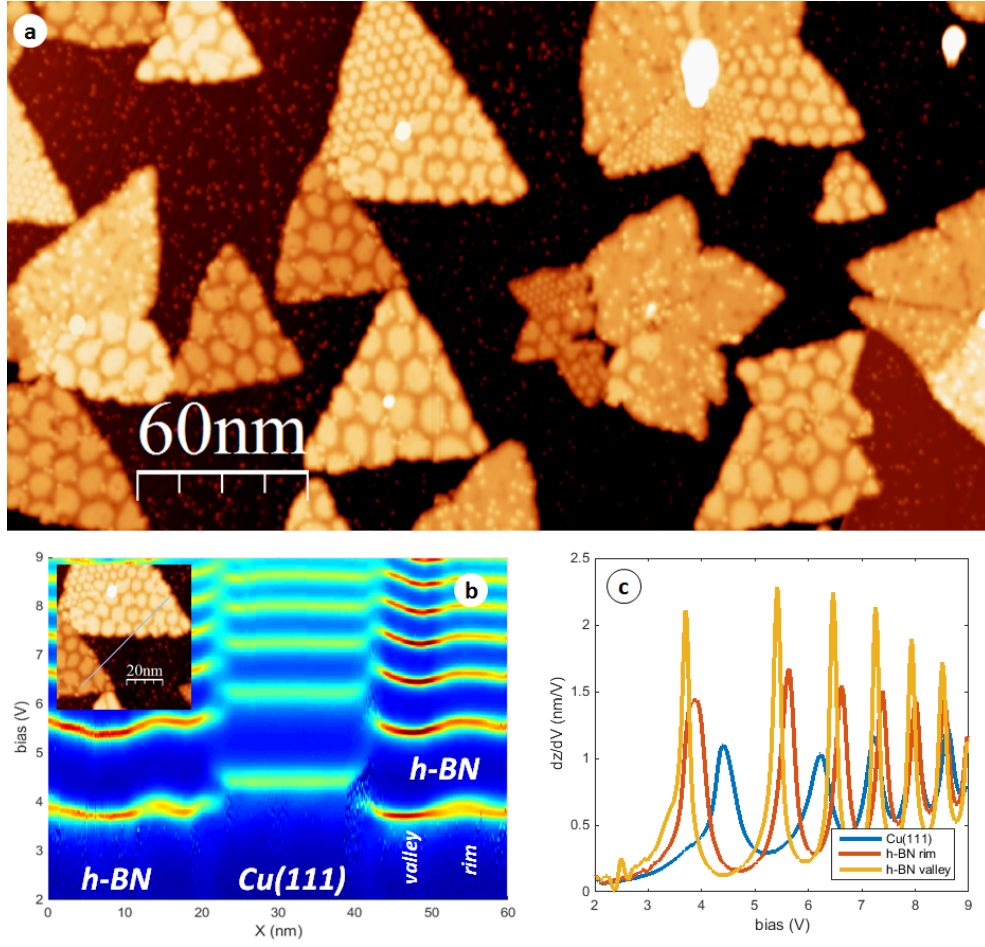


Figure 3.14 – (a) STM topograph of h-BN/Cu(111). $V = +4$ V, $I = 40$ pA. (b) dz/dV spectra taken along a path. The path is marked in the inset. (c) Representative dz/dV spectra on bare Cu(111) (blue), on a rim (red) and on a valley (yellow). The energy broadening at the valley (200 meV) corresponds to an apparent lifetime of $\tau_{FER} = 9$ fs.

further away from the surface compared with a FER on a rim. An outwards pushed FER would have less overlap with the bulk and thus an attenuated decay channel into the bulk [96]. The present hypothesis correlates the FER peak position directly with FER broadening, without turning to additional properties of the FERs (such as localization). However, WF variations can be observed on Ag/Pt(111) [85] without any significant variation of FER width (see Figure 3.1b). In this case, a Ag bilayer adopts a periodic stress relief pattern with no region that can support an extended network of IPSs. This counter-example supports the claim that localization is likely to be the main reason for the difference in FER lifetime rather than surface dipoles.

In conclusion, the lifetimes of FERs on h-BN/Rh(111) are measured and compared with other laterally confined FERs on ultrathin dielectric sheets on metals. 2PPE is an excellent tool to study the energies, lifetimes and effective masses of IPSs, however the absence of nanometre

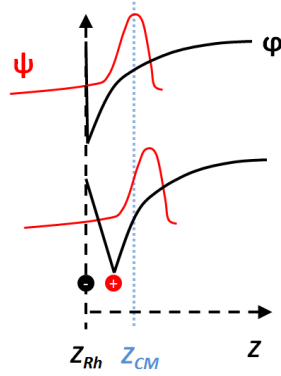


Figure 3.15 – Effect of surface dipoles on the position of IPSs and their overlap with the bulk. The black lines indicate the electron potential in the absence of surface dipoles (top) and in the presence of surface dipoles pointing inwards (bottom). The electrical field pushes electrons towards the vacuum, distancing the IPS' centre of mass (Z_{CM}) from the surface (Z_{Rh}).

scale resolution introduces difficulties in ascribing peaks to structural features [142, 109]. Although STM perturbs the IPSs and reduces their lifetimes [96], the spatial resolution provides valuable, locally resolved spectra, complementary to 2PPE. In spite of the experimental broadening factors, the lifetimes observed here are on par with those found by 2PPE on other flat h-BN layers on Ni(111). By controlling the lifetimes of FERs it would be exciting to enter the regime where the FER lifetime exceeds the tunnelling rate ($\approx 10 \text{ ns}^{-1}$) and leads to a Coulomb blockade, which could be observed by the current dependence of $z(V)$ curves. At a high enough current setting (where $I > e\tau_{FER}^{-1}$), the FER cannot transmit the full current and the tip will settle closer to the surface in order to obtain the missing current by tunnelling directly to the metal. This will be observed as a significant reduction of the Δz associated with the FER step in the $z(V)$ curve, and could be the basis for a nanometric current limiter (a nano-fuse).

3.5 New phase of h-BN/Rh(111)

When imaging h-BN/Rh(111) using STM, three common patterns (depicted in Figure 3.16) may be observed, depending on the tip. Clean metallic tips will image the h-BN as a hexagonal chicken-wire like grid (Figure 3.16a). With certain functionalized tips it will appear as a densely packed array of rings, usually with atomic resolution (Figure 3.16b). With differently functionalized tips, the h-BN occasionally seems like a nanomesh made of two grids with circular holes stacked one on top of each other (Figure 3.16c). Occasionally, a triangular superstructure with a periodicity of 3 nm is observed next to the h-BN (Figure 3.16d). This structure can be identified as graphene [147], which is the result of the segregation of carbon contaminants from the bulk during annealing. It is therefore surprising that on this well studied system we have observed a periodic pattern which does not match any of the previously known phases, which for now we call "spoked wheel" pattern, or SW, and is presented in Figure 3.16e. In this

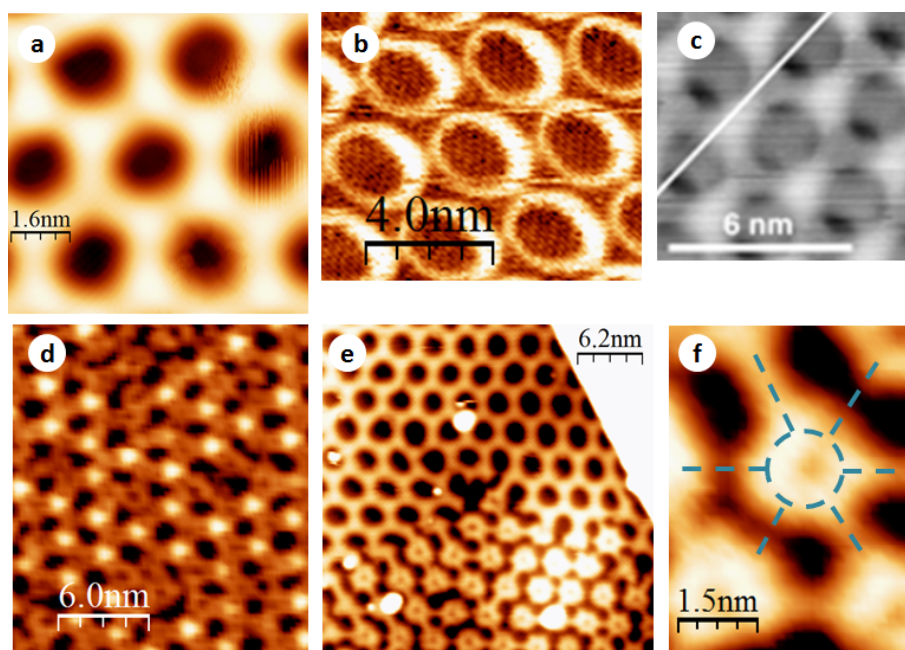


Figure 3.16 – Typical STM topographs of h-BN/Rh(111), graphene/Rh(111) and SW phase. **(a)** h-BN/Rh(111) imaged with a metallic tip. $V = -1$ V, $I = 10$ pA. **(b)** h-BN/Rh(111) imaged by a functionalized tip. $V = -2$ V, $I = 100$ pA. **(c)** h-BN/Rh(111) imaged by a functionalized tip. From M. Corso et al., Science, 303(5655), 2004. Reprinted with permission from AAAS. **(d)** Graphene on Rh(111). $V = -2$ V, $I = 10$ pA. **(e)** Co-existence of regular h-BN with the SW phase. $V = -1$ V, $I = 10$ pA. **(f)** Zoom-in on a unit cell of the SW phase. $V = -2$ V, $I = 10$ pA.

image, the observation of the two phases side by side proves that the SW is not the normal phase imaged with a bad tip. The central ring and the spokes of this structure are indicated in Figure 3.17f.

Figure 3.16e presents a terrace where a regular h-BN domain is juxtaposed with a SW domain. The SW pattern is made of star-shaped objects, roughly 1.3 nm in diameter, packed in a hexagonal lattice with a period of 3.2 nm. Each pair of nearest neighbour stars is connected by a spoke. The unit cell size and symmetry is identical to the regular h-BN domain. Figure 3.17a shows an area where a small domain of regular h-BN is embedded within a SW domain with no notable domain boundary. The same area was imaged using a functionalized tip which provides atomic resolution (Figure 3.17b). The atomic resolution is confirmed by the nearest neighbour distance which is 240 pm on the regular h-BN, close to the known unit cell length of graphitic h-BN of 250 pm [121].

A close observation of Figure 3.17a reveals that the regular pattern evolves smoothly in to the SW pattern, without an apparent barrier or a change of the superstructure. An atomic resolution image of the same region (Figure 3.17b) shows that the atomic periodicity structure of the SW phase is in-phase with the regular h-BN. The rounded valleys of the regular h-BN

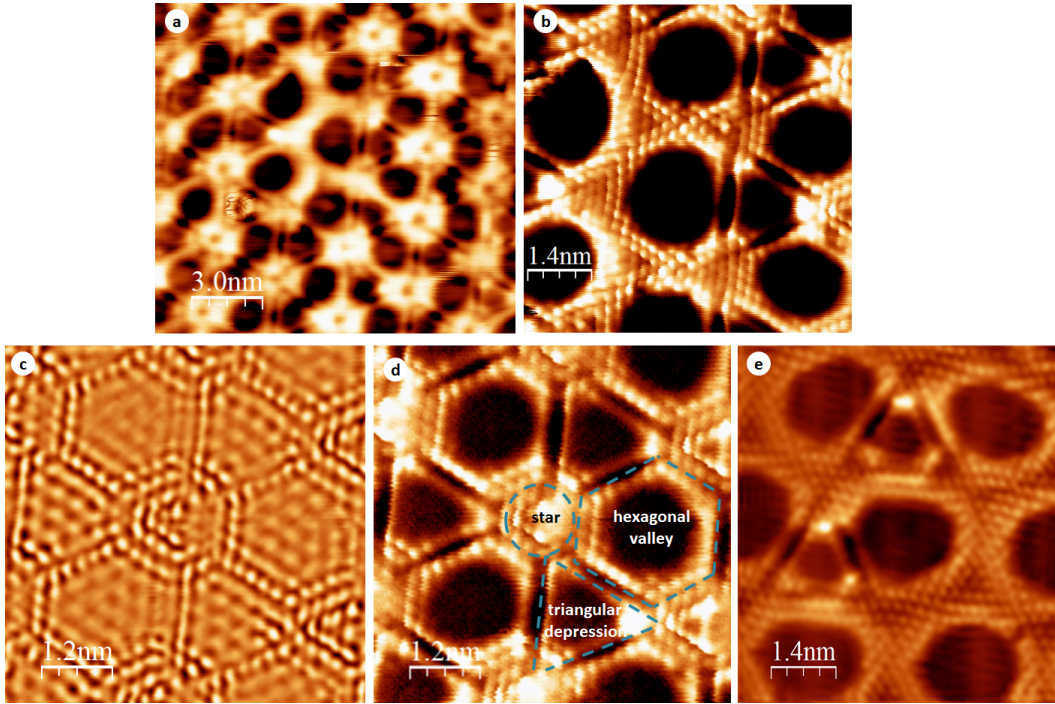


Figure 3.17 – (a) Small domain of regular h-BN is embedded within a SW domain. $V = -0.5 \text{ V}$, $I = 5 \text{ pA}$. (b) Zoom-in of a), imaged at constant height. $V = -5 \text{ mV}$. (c) Fourier filtered, atomic resolution image of the SW phase. (d) Constant height image of the SW phase with atomic resolution. $V = -5 \text{ mV}$. (e) Constant height image of defects in the normal h-BN layer, reminiscent of the triangular pores of the SW phase. $V = -5 \text{ mV}$.

evolve into the slightly smaller hexagonal valleys of the SW pattern (the nomenclature used to describe the SW phase is indicated in Figure 3.17d). Half of the rim crossings of regular h-BN evolve into triangular depressions and the other half into stars, reducing the symmetry of the SW from D_6 to D_3 . With the atomic resolution each spoke, of width 820 pm , is split into two spokes which are 200 pm wide and separated by 550 pm . The spokes can alternatively be described not as lines connecting the stars, but as the borders of the hexagonal valleys and the triangular depressions (Figure 3.17c and d). Additional evidence of the relations between the two patterns can be found in Figure 3.17c, where defects in the rim crossings of the regular h-BN look identical to the triangular valleys of the SW phase. The inclusion of small areas of the SW phase within the regular phase and vice versa suggests a low interfacial energy.

In the regular phase the atoms are positioned in a quasi-hexagonal array, slightly deformed due to the corrugation of the h-BN sheet (see Figure 3.17b). On the spoked wheel phase however the atomic positions are ordered in a hexagonal grid with less deformation. This is particularly evident in Figure 3.17d where the low Fourier coefficients were filtered out of the image, which provides a better image of the atoms at the edges of the hexagons and triangles (the dimmer peaks within the polygons are Fourier filtering artefacts not to be mistaken for atoms). The

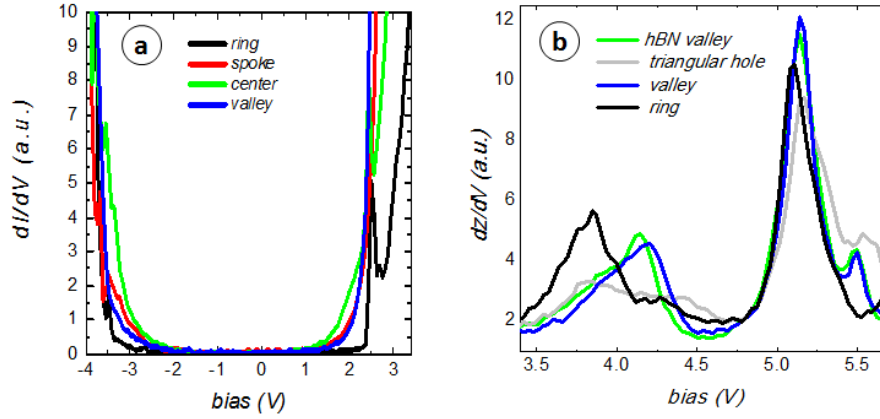


Figure 3.18 – (a) dI/dV spectra taken at various points on the SW phase. (b) dz/dV spectra taken at various points on the SW phase. Only the interface state and the first FER were included for clarity.

average atomic distance between nears neighbour atoms in Figure 3.17d is 240 pm with a standard deviation of 20 pm , very similar to that on the regular h-BN. Due to the limitations of STM, it is not straightforward to determine that what appears to be a depression in an STM image is indeed a hole, and that a bright spot is a protrusion, therefore we approach these distinctions with due care. Due to the continuity of the superstructure between the two phases we assign the large hexagonal depressions to areas of h-BN which are closer to the Rh(111) surface, as in the regular h-BN. We know that on one sub-lattice of rim crossings (the stars of the SW phase) the h-BN atoms are present (they are not holes in the sheet) thanks to the observation of atomic resolution at these positions. As for the triangular depressions, the atoms surrounding them are visible but it is not clear whether there are h-BN atoms within these triangles, other atoms or whether these are holes in the h-BN sheet. After describing the spectroscopic observations of Figure 3.18, we will examine potential explanation for the full set of measurements.

dI/dV spectra and dz/dV spectra were measured at different parts of the SW phase are presented in Figure 3.18. These measurements are however preliminary, and have not yet been reproduced with different tips. dI/dV spectra measured at a constant height (Figure 3.18a) show that the insulating character of the layer is conserved at all positions. The observed bandgaps vary between 4.7 V at the star centre, 5.1 V on the spokes, 5.3 V in the valleys and 5.9 V on the rings. These values are similar to the ones found on the regular h-BN (Figure 3.3d). A preliminary analysis of the dz/dV spectra in Figure 3.18b, shows that the triangular holes present a strongly modified interface state. Perhaps it is gone altogether, and the small peaks are due to diagonal tunneling from neighbouring areas. The first FER is observed at similar bias values on all positions. Additional experiments are still needed to confirm the shapes presented are not tip-related.

Additional experiments were performed in order to pinpoint the source of the SW phase. As the quality of the borazine precursor was suspected, h-BN was prepared with batches of borazine kept in different vials, yielding the same results. The clean Rh(111) crystal was scanned and found free of significant contamination. One factor was found to affect the abundance of the SW domains. Once the sample was submitted to a hot sputtering of an hour ($T = 830^\circ\text{C}$, sputter voltage $V = 1\text{ kV}$, Ar pressure $p = 10^{-6}\text{ mbar}$), the abundance of the SW phase was strongly reduced. Repeated preparations of h-BN caused the abundance of the SW phase to increase gradually, while hot sputterings caused an abrupt reduction in the coverage of the SW phase. The main effect of the hot sputtering is to sputter away carbon atoms which diffuse to the surface during the heating [148]. The sputtering of surface carbons creates a depletion layer where carbon atoms are found in reduced density than in the bulk. The thickness of this depletion layer depends on the annealing temperature and the sputtering rate. Afterwards, the sputtering that is part of sample preparation gradually removes the depletion layer, leading to an increasing segregation of carbon to the surface with each preparation cycle.

We now turn to consider the possible origin and structure of the spoked wheel phase in conjunction with the observations. Rotated domains of h-BN are not likely as they would entail a superstructure lattice parameter different than the regular h-BN, as in the case of rotated h-BN domains on Cu(111). In addition, rotated domains would have nucleated separately and leave many broken B-N bonds. There is however no evidence of separate nucleation sites or any visible feature separating the two phases. The unavoidable presence of carbon on the surface, due to segregation from the bulk, has often manifest itself as graphene domains which exhibit a distinct triangular pattern [147]. Graphene formation under the h-BN sheet would have raised the SW phase with respect to the regular phase. Inclusion of carbon into the h-BN sheet is unlikely, due to the partially ionic character of the B-N bonds [149].

The effects observed after hot sputtering suggest that the source of the SW phase is related to the presence of carbon. One way in which carbon might manifest itself is by getting trapped under the rim crossings. Sputtered Ar atoms have been shown to get trapped under the rim crossings of h-BN/Rh(111) [150] and to appear as raised "nano-tents" in STM images. The nano-tents were imaged as protrusions and have a slight preference for one sub-lattice of rim crossings, where boron atoms are on Rh top sites and nitrogen atoms at hcp sites. Such trapping is also possible for carbon atoms, and they would not necessarily be imaged as protrusions, this would depend on how the carbon atoms would interact with the underlying Rh. Alternatively, the presence of carbon clusters on the surface during h-BN growth might impede that growth and leave holes in the h-BN sheet. The triangle is the lowest energy shape of a large defect in h-BN, as was observed using transmission electron microscopy (TEM) following 100 keV electron bombardment [151]. The triangular depressions observed in STM might really be triangular holes, caused by and filled with clusters of carbon atoms. The presence of atoms or clusters under the other sublattice of rim crossings is also supported by the reduced area of the valleys in the SW phase. DFT calculations have shown that the valleys have a significant contribution to the adsorption energy of the h-BN sheet [3]. Reducing the area of the valleys would be energetically unfavourable, unless the presence of additional

species under the rims would force parts of the sheet away from the Rh substrate.

In summary, new ordered phase of h-BN on Rh(111) was found, although we have not yet been able to clarify its exact origin. The new phase will be studied further in order to understand its composition, structure and whether it could provide additional functionality to the regular h-BN sheet. An ordered array of holes in h-BN (if this is the case) would provide a well ordered grid of reactive sites that could be used as a template for molecule and metal immobilization. We therefore contemplate identifying the presence of a contaminant using XPS and finding how the preparation parameters affect the presence of the SW phase.

4 Towards protein sequencing using STM

In order to add peptides to the catalogue of building blocks for vacuum on-surface self-assembly, a good understanding of the interactions that dominate their behaviour on surfaces in vacuum is required. The interactions that are known to dominate their behaviour in solution (hydrogen bonds, polar interactions, electrostatic interactions etc.) [41] are a good start, but conditions on the surface are quite different. For one, the absence of water removes one of the main forces that dominates peptide self-assembly in solution [41]. In addition, the peptides are partially confined to a 2-dimensional plane, are in close proximity to the surface ions and electrons, and are affected by the symmetries of the surface lattice [152]. To understand how all of these interactions affect the self assembly process, it is necessary to first study how the conformations of individual peptides are affected by interactions with the surface. STM provides a powerful tool to study the conformations of individual molecules and molecule assemblies on surfaces [152]. However, peptides pose a challenge to this technique as they lack the properties that make other molecules, such as phthalocyanines [153] and porphyrins [154], suitable for STM: a highly symmetrical, flat and stiff structure. The flexibility and low symmetry of peptides makes it difficult to identify features in STM images with the known structure of the peptide. It is therefore vital to identify the positions of amino acids in STM images of peptides in order to understand how the interactions between the peptides and the substrate lead to the conformations they adopt. Fortunately, STM offers additional modes of operation that can provide complementary information to the topography. For example, guanine, one of the bases from which DNA is composed, was discriminated from the other bases in DNA strands thanks to a distinctive peak in STS [155]. Alternatively, the use of functionalized STM tips has provided enhanced resolution on pentacene and naphthalocyanine molecules adsorbed on a bilayer of NaCl grown on Cu(111) [156]. In this chapter we present first attempts to harness STS and tip-functionalized STM in order to extract such complementary information, towards the final goal of full on-surface peptide sequencing.

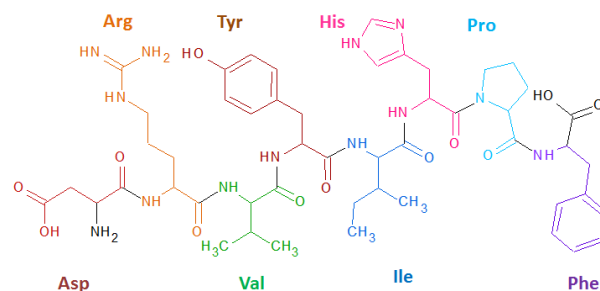


Figure 4.1 – Molecular structure of At-II. The names of the amino acids are indicated next to the corresponding side chains.

4.1 Angiotensin-II on Cu(111)

At-II (Figure 4.1) is a peptide with an important role in the regulation of blood pressure [157]. It is part of the renin-angiotensin system [158], which is a major target for drugs that lower blood pressure. When renal blood flow is reduced, kidney cells secrete renin into the bloodstream. Renin then carries out the conversion of angiotensinogen released by the liver to angiotensin-I. Angiotensin-I is subsequently converted to At-II by the enzyme angiotensin-converting enzyme (ACE) found in the lungs. At-II causes blood vessels to constrict, resulting in increased blood pressure. At-II contains 8 amino acids (Asp-Arg-Val-Tyr-Ile-His-Pro-Phe) and has a molecular weight of 1046.18 Da [159]. We used At-II because of its relatively small size and the ability to obtain isolated peptides by slightly annealing At-II peptides deposited on Cu(111) [160].

Cu(111) surfaces were prepared by sputtering a Cu(111) crystal with Ar^+ ions at 1 kV for 20 min, followed by annealing at 530 C during 5 min. The sample was then moved to the ES-IBD chamber via an UHV suitcase where At-II was deposited in the +2 charged state, with a total charge of 29 pAh. The sample was then transported back to the STM chamber via the UHV suitcase and imaged at 5.3 K in the STM.

Figure 4.2a shows a large area scan of the resulting sample, with a coverage of 0.2 ML. Many of the observed features show variable shapes and sizes, corresponding to self assembled structures made of several molecules. Smaller structures can be found with specific and repetitive shapes. The overall appearance is similar to previously observed STM images of this system [160]. The most common repeating structure observed is depicted in Figure 4.2b, with a C_2 symmetry and dimensions that would correspond to a partially folded At-II dimer (2.4 nm length and 1.2 nm width per peptide). Two ball-and-stick models of At-II molecules are presented in Figure 4.2c in order to emphasize the similarity of their size to the size of the dimer. These dimers are found in three different orientations rotated by 120° with respect to each other, The different orientations are indicated by coloured lines in Figure 4.2a and d.

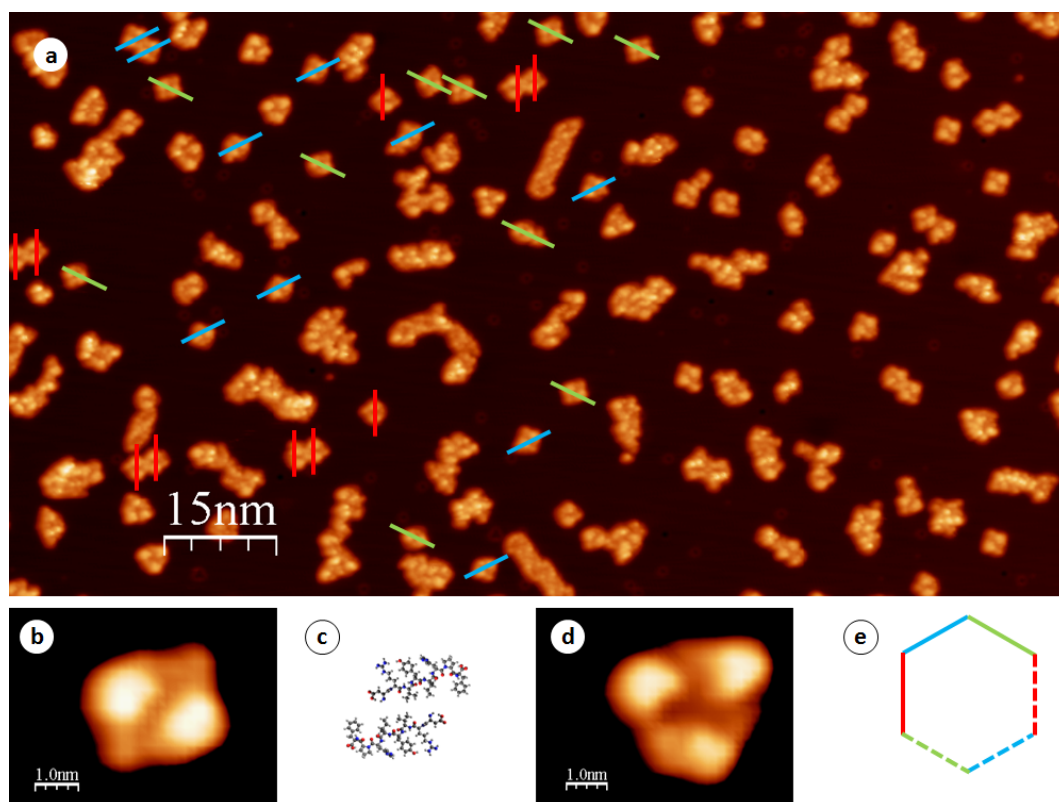


Figure 4.2 – At-II/Cu(111) overview. **(a)** Overview scan of At-II on a Cu(111) surface. Orientations of dimers are indicated by lines of different colours. $V = +1$ V, $I = 100$ pA. **(b)** Zoom in on dimer, $V = +1$ V, $I = 100$ pA. **(c)** Ball-and-stick model of two At-II peptides, to scale with the zoom-ins. **(d)** Zoom in on trimer, $V = +1$ V, $I = 100$ pA. **(e)** Comparison of the orientations of the dimers shows that they are rotated 120° with respect to each other.

This observation indicates a significant interaction with the substrate that leads to a preferred registry with respect to the top layer of Cu. Triangular structures with dimensions corresponding to trimers are also common, although with less reproducible shapes (Figure 4.2d).

Annealing the sample at 40 C for 2 min changes the topographic appearance of the At-II structures. After annealing, dimers are nearly impossible to find. Small regular structures appear (Figure 4.3a) which we identify as monomers according to their size. Trimers are found in larger numbers after annealing (Figure 4.3b), with three different recurring shapes. The appearance of trimers after annealing can be understood as a more stable energetic configuration that is only achieved by crossing a certain reaction barrier. The appearance of monomers is more surprising, as the peptides are deposited as monomers, and if the monomer were a stable conformation, one would expect to see it immediately after the deposition. This question is still a matter for ongoing research, and it is possible that the monomer reacts and binds to a mobile Cu adatom through coordination bonds and thus achieves a configuration more stable than the dimer conformation. The monomers are found

in six different orientations rotated by 60° , once again indicating a preferred registry with respect to the top Cu layer. Only one chirality of the monomer was observed, an observation that we associate with the chiral properties of peptides in general. Most amino acids have a chiral structure [41] (except for glycine), and are found in nature only in the L enantiomer. Proteins exhibit chirality also at the supramolecular level, for example, the α -helix is a very common structural motif in proteins [41], which occurs naturally mostly as a right handed helix [41].

Three varieties of trimers are observed after annealing, depicted in Figure 4.3b, and are denominated types A, B and C. Trimer A has a triangular shape with pronounced lobes at the corners and a small depression at the centre. It has a C_3 symmetry that is due the inhomogeneity along the edges, and it is found in two distinct orientations rotated by 60° with respect to each other. Trimer B is shaped like a triangle with trimmed corners. The entire contour of the shape is raised with respect to the centre, leaving a "Y" shaped depression at the centre. Three pairs of lobes are arranged in a chiral pattern around the centre, each pair arranged like the blade of a fan. Trimer B has an overall C_3 symmetry and is also found in two distinct orientations rotated by 60° with respect to each other. Trimer C has the overall aspect of three "L" shaped objects, each with a protrusion at the joint, assembled around a common centre looking outwards. It has a C_3 symmetry and unlike the other trimers it is found in only one orientation (in all 30 observations), i.e. it is not found in the 60° rotated orientation. This observation is surprising, because the Cu(111) top surface layer belongs to the sixfold (D_6) point group symmetry. It is possible that this structure is sensitive to the second layer of Cu atoms. Such a symmetry breaking has been observed in 4-[trans-2-(pyrid-4-yl-vinyl)] benzoic acid (PVBA) molecules adsorbed on Cu(111) [161], where it was found that the subsurface Cu layer had an effect on the surface's local capacity to screen the dipole moment of the molecule, leading to a 47 meV energy difference between the two adsorption configurations.

A functionalized STM tip can sometimes resolve features that a clean metal tip cannot [156]. This can occur due to the presence of p- or d-orbitals at the tip apex which are sensitive to the corresponding symmetries at the sample [156]. Alternatively, an adsorbate at the tip apex can change its orientation due to its interactions with the sample, leading to a current that varies depending on how the apex molecule is oriented during the measurement [162]. In the present study, we were able to image the At-II structures with tips functionalized by unknown adsorbates (Figure 4.4). In these images, new features can be observed on the At-II structures. In Figure 4.4a the dimer appears with 14 internal lobes while only two are visible with a clean tip. The 14 lobes of the dimer might correspond to the 7 large amino acids present in each peptide. Proline is not likely to be observed as a protrusion, as it has no bulky side-chain (see Figure 4.1). On a type-A trimer, the same tip shifts the position of the brightest lobes from the corners of the triangle inwards, about 0.6 nm towards the centre of the triangle (Figure 4.4b). The C_3 symmetry of this trimer becomes more evident with this functionalized tip, which resolves 24 lobes as opposed to only 9 lobes with a clean tip. The 24 lobes of the type-A trimer may indicate the positions of the 7 large amino acids of the peptide, with three additional bright lobes possibly at the positions of Cu atoms incorporated into the structure. 18 lobes

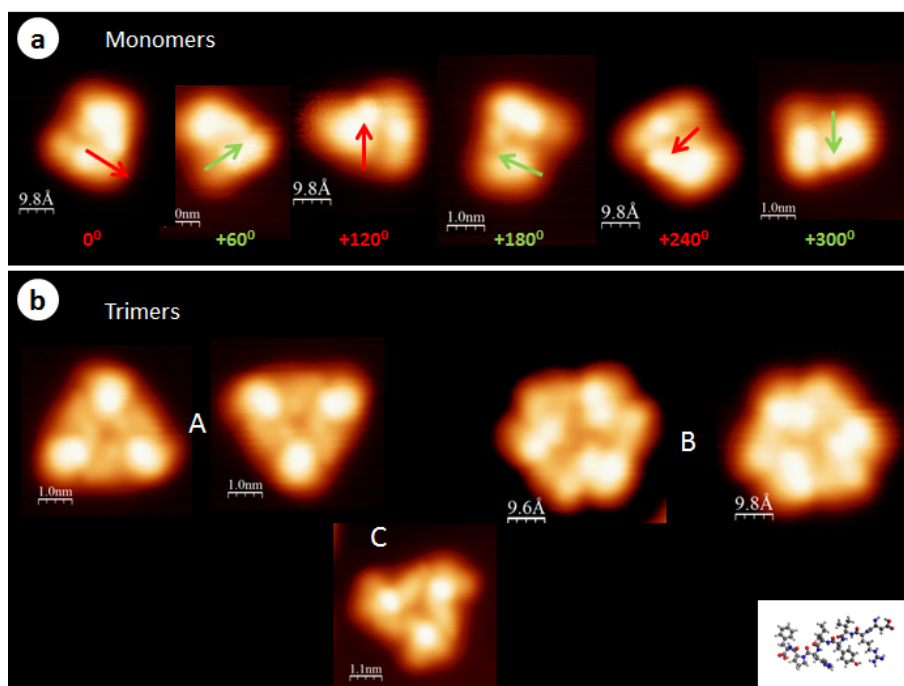


Figure 4.3 – Conformations of At-II on Cu(111) after annealing. Scan parameters for all images are $V = +1$ V, $I = 100$ pA. **(a)** Six different orientations of the monomer are rotated 60° with respect to each other. No enantiomers are found. **(b)** Type A, B and C trimers in all of the observed orientations. Inset: ball-and-stick model of At-II, to-scale with the STM images.

were observed with the same tip on a type-C trimer (Figure 4.4c), compared to 6 with a clean tip. In Figure 4.4d-e we see the monomer and a type-C trimer imaged with a different tip. These images are reminiscent of the faceted structures obtained when imaging with a CO functionalized tip [162]. At-II has a complex inner structure and, as expected, this complexity makes it impossible to correlate the observed structures directly with the structure of At-II.

dI/dV spectroscopy was performed in order to try and obtain additional information about the structures, in the hope to find a fingerprint that would identify the amino acid side chains. A few spectra are displayed in Figure 4.5a, where it can be seen the spectra are mostly featureless. Peaks observed around $V = -0.3$ V correspond to the Cu(111) surface state (a spectrum taken on Cu(111), divided by 2.5, is provided for reference). The faint shoulder at $V = -1.3$ V was not reproduced in other dimers, which might suggest it is related with the tip. It is often the case that the spectroscopic signature cannot be observed on molecules adsorbed directly onto metallic substrates [163]. The absence of discernible molecular orbitals is a result of orbital hybridization between the molecular orbitals and the dense electron bath of the metal. This causes an energetic broadening beyond recognition of the molecular orbitals, and the formation of new electronic states with mixed molecular and metallic character [164, 165]. Molecular orbitals are more readily observed when a thin decoupling layer acts as a spacer and keeps the molecule further from the metal [46].

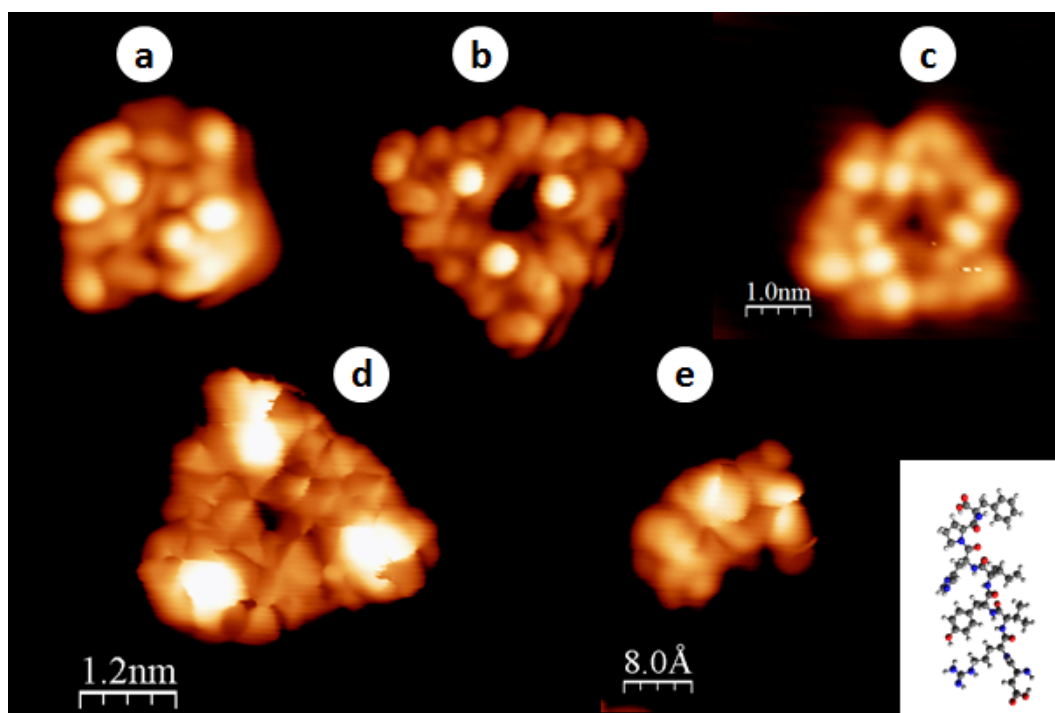


Figure 4.4 – STM measurements of At-II with functionalized tips. **(a)** At-II dimer measured with a functionalized tip, $V = +1$ V, $I = 100$ pA. **(b)** Type A trimer measured with a functionalized tip, $V = +1.5$ V, $I = 100$ pA. **(c)** Type C trimer measured with a functionalized tip, $V = -1$ V, $I = 5$ nA. **(a)-(c)** were measured with the same tip. **(d)** Type A trimer, probably measured with a CO functionalized tip, $V = +0.5$ V, $I = 1$ nA. **(e)** At-II monomer, probably measured with a CO functionalized tip, $V = -1$ V, $I = 1$ nA. Inset: ball-and-stick model of At-II, to-scale with the STM images.

4.2 Angiotensin-II on h-BN

With the goal of identifying spectroscopic fingerprint on single peptides, we seek a decoupling layer thin enough to allow sufficient tunnelling currents to perform stable STM measurements, and at the same time distance the molecules enough from the substrate to prevent orbital hybridization with the metal. Several suitable layers are known and used for this purpose in STM such as NaCl [46] and C_{60} [166], but often the weak interaction of molecules with the decoupling layer leads to high diffusion rates of the molecules at room temperature [167], and the molecules diffuse away from decoupling layer or form large aggregates [168]. h-BN/Rh(111) has shown the capacity to trap phthalocyanine molecules inside its valleys even at room temperature [136], making it the most suitable substrate for our purpose. The trapping potential is the result of lateral electrical fields due to the variation of WF between the valleys and the rims. h-BN/Rh(111) was prepared as is described in Section 3.2.1, and At-II was deposited by ES-IBD as described in Section 4.1. We focused our attention on h-BN valleys where a single, elongated object was found, some examples of which are presented

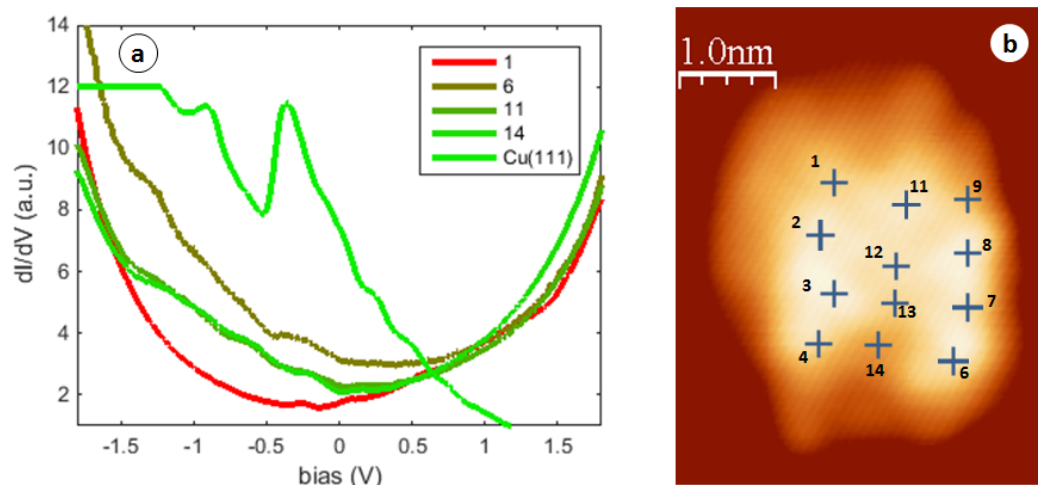


Figure 4.5 – (a) dI/dV spectra taken on an At-II dimer on Cu(111) using a lock-in amplifier. The tip was stabilized at each point at $I = 300$ pA. Modulation amplitude 50 mV, frequency 811 Hz. The spectrum taken on clean Cu was divided by 2.5 for better visibility. (b) STM topograph of the dimer, $V = +1$ V, $I = 300$ pA. The positions where the spectra were taken are indicated with crosses.

in Figure 4.6a-e. These objects exhibit an elongated body with a dominant bulge somewhere along the body, mostly at the end facing the centre of the valley. We identify these structures as At-II monomers, confirming that the trapping capacity of h-BN/Rh(111) is also well suited for small peptides at room temperature. Unlike phthalocyanines and Xe atoms [2], At-II does not show a preference to lie along the valley's perimeter, but rather across the valley's diameter, through the centre. dI/dV spectroscopy on these objects consistently gives rise to a peak near $V = +600$ mV (Figure 4.7), observed only at the central bulge. Near the central bulge, smaller peaks can be observed at $V < 0.2$ V.

The hunt for spectroscopic features is made difficult in this case by the non-flatness of the molecule and the electronic variability of the substrate. Spectra taken at a constant height are not comparable due to the varying distance from the molecule, while spectra taken while stabilizing the tip at a constant current suffer from varying proximity to the substrate [169]. On h-BN this is exacerbated by the fact that the dI/dV spectra of rims are different than those of the valleys (see Figure 3.3c). These first attempts show that spectroscopic features can be observed on At-II when it is decoupled from its metallic substrate. The central bulge of the molecule presents a distinguishable peak, which may be the signature of a specific amino acid. Further studies are needed in order to identify more spectroscopic features and identify their positions along the peptide. Better understanding of the dI/dV spectra will require a consistent background subtraction procedure, that accounts accurately for tip-substrate distance and for the tip's distance from the pore's centre.

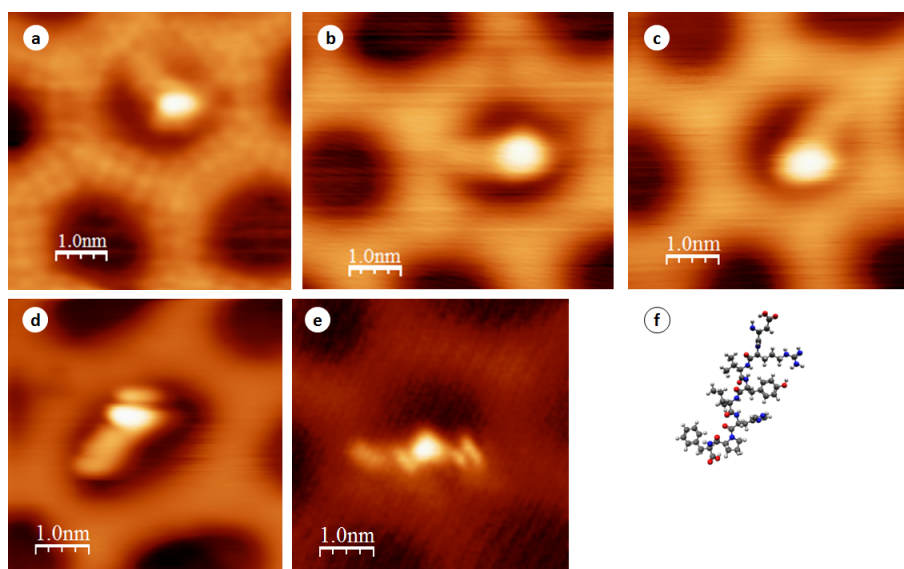


Figure 4.6 – (a)-(d) STM topographs of individual At-II molecules inside valleys of h-BN/Rh(111). All images are to scale. $V = -500\text{ mV}$, $I = 5\text{ pA}$. (e) Constant height image of an At-II molecule inside a valley of h-BN/Rh(111). $V = +50\text{ mV}$. (f) Ball and stick model of At-II molecule, to-scale with the STM images.

The high resolution images of At-II structures obtained with a functionalized STM tip (Figure 4.4) indicate it may be possible to identify amino acids in STM topographs, provided the tip is functionalized with the proper molecule. In order to functionalize the STM tip with a known molecule, we deposited pentacene [170] ($C_{22}H_{14}$, see Figure 4.8a) on h-BN/Rh(111). Pentacene was deposited by thermal sublimation at $185\text{ }^{\circ}\text{C}$ for 5 min on a h-BN/Rh(111) held at room temperature, giving a coverage of 0.01 ML . The pentacene molecules are easily observable thanks to their flat, elongated structure, and single molecules could be found in h-BN valleys (Figure 4.8b). The pentacene molecules are observed on the pore's circumference, which is known for its trapping potential due to the presence of lateral electrical fields [2]. The highest occupied molecular orbital (HOMO) and the lowest unoccupied molecular orbital (LUMO) are clearly visible in the dI/dV spectrum (Figure 4.8c). The HOMO and LUMO could be spatially imaged in constant height mode (Figure 4.8d and f as well as in constant current mode (Figure 4.8e and g). The good contrast with which the gas-phase molecular orbitals can be imaged is evidence of the successful decoupling properties of the h-BN sheet [170]. Additional proof of this property is the observation of negative differential conductivity at $V = +1.75\text{ V}$ [171]. In future experiments we will study the optimal parameters for picking up pentacene molecules. If successful we will use pentacene terminated STM tips to image At-II peptides. With the improved resolution provided by functionalized tips we hope to be able to identify the structure of the peptides.

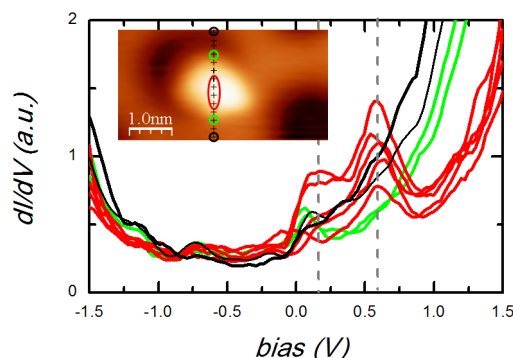


Figure 4.7 – dI/dV spectra taken on an At-II molecule in a h-BN valley. Tip positions are marked in the inset. The red curve was measured on the main protrusion of the molecular structure, the black curve on the h-BN and the other curves on different parts of the molecule. A was observed at the central bulge at $V = +663 \text{ mV}$. The tip was stabilized at each point with $V = -1.5 \text{ V}$, $I = 30 \text{ pA}$. All spectra were subtracted with the valley spectrum (black).

4.3 Outlook

The results in this chapter represent early steps towards peptide sequencing using STM. Even for a relatively large molecule, the complexity of the organization of At-II on Cu(111) is surprising. In addition to the size of the molecule and its flexibility, the structures and conformations that were observed indicate the potential incorporation of Cu adatoms, chiral selectivity and influence of the second Cu layer. On this system it was observed that spectroscopy is ineffective when the molecules are in direct contact with a metallic substrate. We also observed that functionalized tips can provide additional contrast. Our following experiments had to be performed on a decoupling layer that interacts weakly with the molecules, but which still has the capacity to trap single molecules in order to avoid aggregates. h-BN/Rh(111) has been shown to trap single phthalocyanines at room temperature [136] and our experiments demonstrate that At-II can also be isolated in the h-BN valleys. On this layer we show first attempts at using the electronic properties to identify the peptide structure. In addition, we began experimenting with pentacene on this substrate in an effort to functionalize the tip with a familiar adsorbate and obtain improved resolution of the At-II molecules. An improved topographic resolution may allow us to identify specific side chains, an identification which will then be used to correlate local electronic properties with particular side chains. Additional STM techniques may provide even further information and contrast such as WF mapping [78], which provides information about local charge transfer from the surface, and inelastic electron tunnelling spectroscopy (IETS) which provides information about vibrational modes of the molecule [172]. With the combination of these methods we hope to be able to sequence peptides, by identifying a combination of properties that uniquely identifies every amino acid. Peptide sequencing using STM will allow us to understand the organization and properties of peptides used as building blocks for on-surface self assembly.

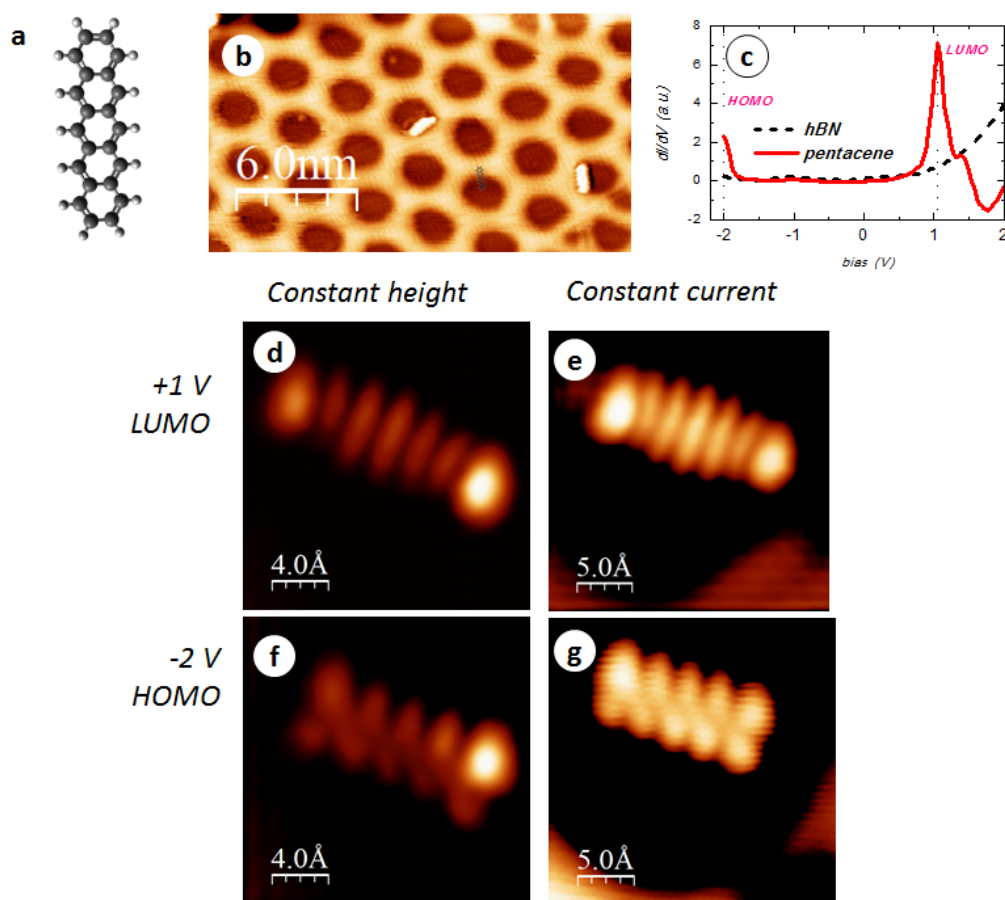


Figure 4.8 – STM and STS of pentacene on h-BN/Rh(111). (a) Ball-and-stick model of pentacene, $C_{22}H_{14}$. (b) Overview scan of pentacene on a h-BN/Rh(111) surface. (c) dI/dV measurements at the centre of a pentacene and on clean h-BN. The LUMO and HOMO are clearly visible. (d) Constant height image of pentacene on h-BN/Rh(111) at $V = +1$ V shows a clear image of the LUMO of pentacene [170]. (e) The shape of the LUMO can even be seen in a constant current mode image. (f) Constant height image of pentacene on h-BN/Rh(111) at $V = -2$ V shows a clear image of the HOMO of pentacene [170]. (g) The shape of the HOMO can even be seen in a constant current mode image.

5 Directed self-assembly of proteins on patterned substrates

5.1 Introduction

Surface chemistry and geometry provide powerful tools to immobilize small molecules at specific locations on surfaces and derive functionality from them [27]. Large molecules such as proteins require a higher degree of control due to the enormous conformational freedom that is a result of their size and flexibility. This chapter presents STM investigations of the conformations of individual proteins deposited by ES-IBD on a Cu₂N template monolayer on Cu(100). We demonstrate that this substrate can be used as a template that favours unfolded protein conformations along the exposed Cu strips. This significantly reduces their conformational freedom, leading to a discrete distribution of stretched out conformations following the Cu grid.

the observed distribution of surface conformations. For a system whose size is challenging for DFT calculations, simplified models can be used for hypothesis testing, by incorporating physical and chemical assumptions into the calculation. We use such a simplified model in order to test whether the on-surface mobility of CytC is limited by the presence of exposed lines of Cu.

5.1.1 Cytochrome-C

CytC is a protein that contains 104 amino acids (Figure 5.1) [174]. As long as it is anchored to the inner mitochondrial membrane, it is a component of the electron transport chain in the mitochondria. The electron transport chain is a series of compounds that transfer electrons from electron donors to electron acceptors via redox reactions, with the final goal of extracting energy from sunlight in photosynthesis, or from ATP in cellular respiration. As part of the electron transfer chain, the heme group of cytochrome-C accepts electrons from the bc₁ complex and transfers electrons to the complex IV (or cytochrome c oxidase) [174]. CytC is also involved in initiation of apoptosis, a form of controlled cell death used to kill cells in the process of development or in response to infection or DNA damage [175]. Once released from the inner mitochondrial membrane, it binds with additional proteins to create a protein

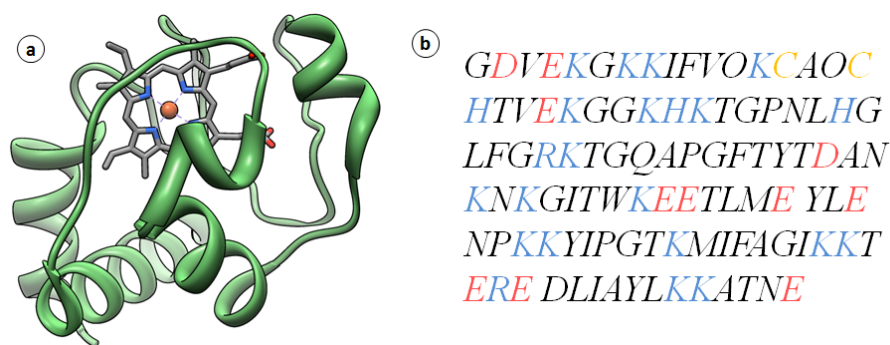


Figure 5.1 – (a) CytC protein schematic. Reproduced from [173] under CC BY-SA 3.0 license. (b) Amino acid sequence of CytC. At physiological conditions some side chains are positively charged (marked in blue) or negatively charged (marked in red). Amino acids marked in yellow have thiol bearing side chains.

complex known as an apoptosome. The apoptosome cleaves the pro-caspase protein to its active form of caspase-9, which continues a cascade of protein cleavages leading to cellular death [174]. CytC was the first protein to be identified in the predicted molten globular state [176]. In the molten globular state the protein is partially folded, its backbone having assumed its natural secondary structure, but with the side chains in random orientations.

More recently, deposition using ES-IBD has enabled high resolution STM imaging of isolated CytC deposited on clean metal surfaces [49], revealing the protein adsorption transition from globular on an unreactive surface (h-BN/Rh(111)), to flat puddles on Au(111). On still more reactive surfaces such as Cu(100), careful examination of the persistence length found that a higher charged state of the deposited protein leads to a longer persistence length of the adsorbed species [49]. This result is promising as it shows that ES-IBD provides some degree of control over the on-surface species, a degree of control that can be augmented by design of the molecules and the surface, for example by deposition on a nanopatterned surface.

5.1.2 Copper nitride on Cu(100)

Adsorption of activated N on Cu(100) was first performed in 1986 by Ibach and coworkers [177]. The system sparked a long controversy as to the exact positions of the nitrogen atoms on the Cu(100) surface and the correct interpretation of STM images [48, 178, 179, 180, 181]. The debate was only recently concluded with low temperature STM performed in the group of Jay Gupta [182]. Upon adsorption on the copper surface, nitrogen forms a $c(2 \times 2)$ lattice, resting on saddle sites in alternating rows of the top Cu layer. DFT calculations indicate there is a net charge transfer of about $1.2e$ from the Cu atoms to the N atoms (see Figure 5.2) [183]. In order to adsorb on Cu, N_2 molecules must be ionized by a hot filament [48]. At low N coverages, roughly square islands of Cu_2N are formed, exhibiting a $c(2 \times 2)$ lattice and their apparent height in STM is lower than that of the surrounding Cu surface (Figure 5.2, c), with a tendency

to group along the $\langle 001 \rangle$ directions. The islands measure approximately $5 \times 5 \text{ nm}^2$, and their size is limited due to lattice mismatch with the substrate [48]. At higher coverage the distance between the islands decreases, until at nearly full coverage they are packed into a gridlike array separated by one to two atom wide Cu ridges (Figure 5.2, d). At even higher dosage of N the islands coalesce into a quasi continuous monolayer with a different mechanism of stress relaxation, in the form of trench-like defects running in the $\langle 011 \rangle$ directions (Figure 5.2, e), caused by the absence of two atomic rows of Cu. These mechanisms of self assembly are driven by the 3% lattice mismatch between Cu_2N and the $\text{Cu}(100)$.

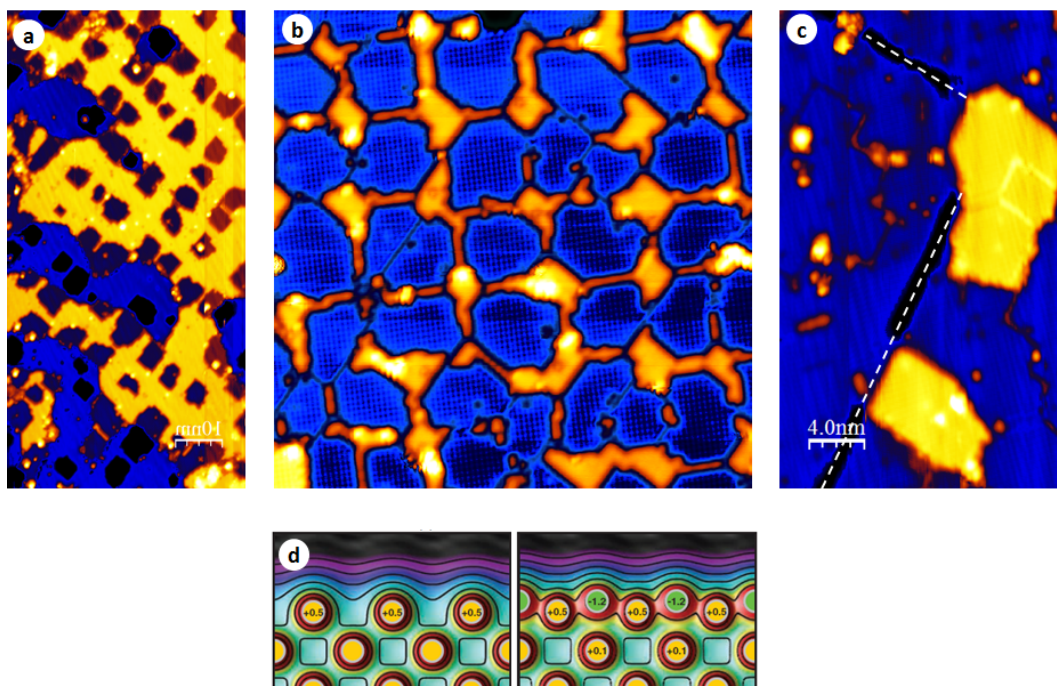


Figure 5.2 – (a) STM topograph of a low coverage of Cu_2N on $\text{Cu}(100)$. In this regime the Cu_2N forms isolated, roughly squared $5 \times 5 \text{ nm}^2$ islands imaged by STM as deeper than the surrounding Cu. (b) STM topograph of nearly full coverage $\text{Cu}_2\text{N}/\text{Cu}(100)$. The islands pack into a square tiling of the surface, separated by thin stripes of bare Cu. Atomic resolution can often be found in the islands, imaging N or Cu atoms depending on the polarity of the bias [182]. (c) STM topograph of a saturated coverage of Cu_2N on $\text{Cu}(100)$. The islands coalesce into a quasi continuous layer of Cu_2N , and a new type of defect appears in the form of trenches (indicated by dashed white lines). (d) Atomic structure of the system based on DFT calculations [183]. N atoms (green) occupy the gaps between nearest neighbour Cu atoms (yellow) in every other row. The image indicates the charge localized at each atomic position in units of electron charge. From C. F. Hirjibehedin et al., Science, 317(5842), 2007. Reprinted with permission from AAAS.

The patterning capacity of the $\text{Cu}_2\text{N}/\text{Cu}(100)$ system was recognized in the 90's where it was tested as a substrate for the self-assembly of magnetic dots suggested as candidates for information bits [8]. Metals evaporated onto the grid-like phase of $\text{Cu}_2\text{N}/\text{Cu}(100)$ nucleate at the junctions between the Cu_2N islands, creating a well ordered $5 \times 5 \text{ nm}^2$ array of magnetic dots. More recently $\text{Cu}_2\text{N}/\text{Cu}(100)$ experienced a revival being used as a substrate for decoupling single magnetic atoms and nanoengineered structures thereof from the underlying metal, in order to preserve their magnetic properties [183]. Atoms will, however, only stick to the Cu_2N islands if they are deposited on a substrate cooled below 40 K. The large difference in sticking coefficient between the bare Cu and the Cu_2N was recently found to induce interesting adsorption behavior of long aromatic molecules [184]. When deposited on a substrate cooled to 30 K some of the molecules assumed a conformation bridging across the Cu_2N island and leading to vibronically assisted tunnelling through the parts of the molecule insulated from the Cu.

5.2 Experimental procedure and initial observations

5.2.1 Sample preparation

In the MBE chamber, a Cu_2N layer was prepared on a clean $\text{Cu}(100)$ surface by sputtering N_2 at $5.7 \times 10^{-6} \text{ mbar}$ during 5 minutes at $7.4 \mu\text{A}$ and 1 kV. The surface was then heated briefly to 400 °C. The sample was then transferred to the ES-IBD chamber via UHV suitcase where CytC was deposited in the +12 and +13 charged states, at room temperature, with a deposited charge of 43.3 pAh. The sample was then returned to the low temperature STM chamber for high resolution imaging. A separate deposition was performed in order to observe ≈ 500 molecules and estimate the distribution of conformations. For this purpose, the deposition took place within the ES-IBD system, and imaged at room temperature in an Omicron STM connected to the ES-IBD.

5.2.2 Appearance of individual molecules

In the STM images (see Figure 5.3), CytC molecules on Cu_2N are imaged as long chains (Figure 5.2), 22 – 30 nm in length, 1 nm wide, with an apparent height of 0.4 nm, similar to its appearance on other substrates [49]. The broad distribution of lengths comes as a result of partial folding on the Cu lines. Ideally, a stretched out protein would have the length of 28.9 nm, obtained by multiplying the single amino acid length of 0.278 nm (from the amino N to the carboxylic O) by 104. It has been observed that the length of proteins is hard to estimate based on STM images due to partial folding. On $\text{Cu}(100)$, accurate estimates of the molecule's length can be obtained by tiling the STM image of the protein chain with discs of diameter $< 1 \text{ nm}$ [49]. Height variations can be observed along the protein, but no recurring features were found that could indicate the protein orientation. Nearly all the isolated chains follow the exposed Cu grid lines and avoid the surface of the Cu_2N islands. Adherence to the Cu

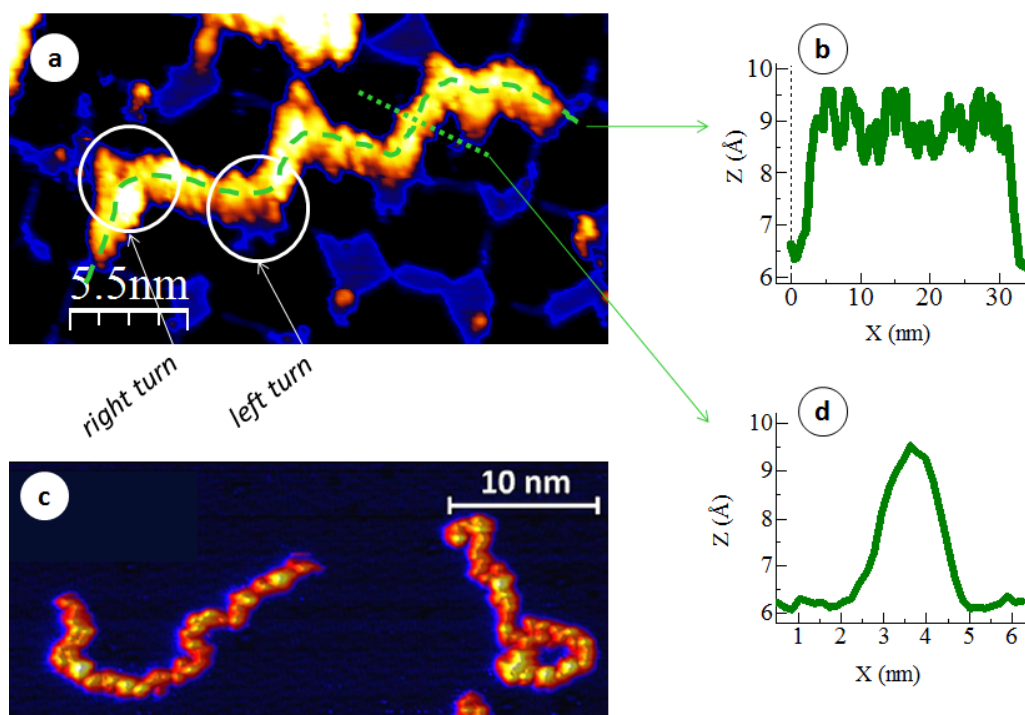


Figure 5.3 – Appearance of a single CytC protein on Cu₂N. **(a)** STM topograph of a CytC protein on Cu₂N/Cu(100). The adsorption to the square grid of exposed Cu forces the polypeptide chain into a structure of straight segments of 5 nm, separated by angles of -90° , 180° or $+90^\circ$, denominated left turns, straights and right turns. Scan parameters are $I = 100$ pA, $V = +1$ V. **(b)** Line profile along the protein. **(c)** CytC proteins on Cu(100), Reprinted with permission from Z. Deng, Nano Lett., 12(5). Copyright 2012 American Chemical Society. **(d)** Line profile across the protein.

grid means that the proteins adopt configurations made of 5 nm segments connected by 90° or 180° angles. In the following, we will refer to the places where segments are connected as joints, which can have one of three configurations: a right bend, a left bend or a straight (right and left being arbitrarily chosen). Depending on the coverage, some of the proteins are found in aggregates, making it impossible to distinguish between single proteins, and these aggregates were therefore ignored in our analysis.

5.2.3 Possible diffusion mechanisms on the surface

Adsorption on the Cu is obviously energetically preferable to the Cu₂N. In a previous study where long aromatic molecules were deposited on Cu₂N [184], the molecules occasionally formed bridges across the Cu₂N islands. This configuration was, however, only achieved when cooling the sample to 30 K during deposition. In our case, nearly no CytC molecules were observed stretched across Cu₂N islands (as illustrated in Figure 5.4). This suggests that although the molecule is eventually strongly adsorbed onto the Cu lines, diffusion does occur

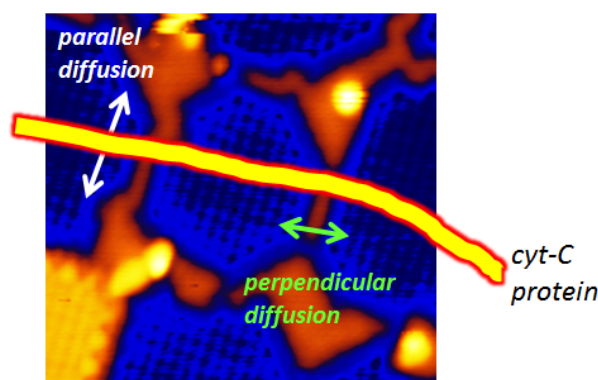


Figure 5.4 – Illustration of a CytC molecule on Cu_2N , before diffusing onto the Cu grid. Diffusion along the Cu lines (white arrow) does not change the contact area of the protein with the bare Cu, therefore the barrier for this sort of diffusion is low. Diffusion along the Cu lines ends when the peptide chain meets the Cu line parallel to it. The same contact area argument applies to diffusion across the Cu lines (green arrow), with the exception that the thiol terminated amino acids bond to Cu more strongly than others, thus acting as pinning centres for diffusion across Cu lines.

prior to the molecule's immobilization, in parallel or in perpendicular to the Cu lines. In other words, the molecular groups in contact with the Cu are not pinned to their position, they are capable of one or more of the following modes of diffusion. Diffusion along the Cu lines (parallel diffusion) can be done by sliding, rolling or reptation (a snake-like motion observed in polymers and proteins [185]). Alternatively, perpendicular diffusion consists of a sliding of the entire protein along its axis, as illustrated in Figure 5.4. Parallel diffusion is likely even in the case of thiol bearing amino acids (such as cysteine). Although thiol end groups tend to adhere strongly to Au and Cu, they have a low energy barrier for diffusion on those surfaces [186]. Because of the stronger adhesion of thiols to Cu, it is likely that perpendicular diffusion is blocked by thiol bearing side chains. However, CytC only contains two thiol bearing amino acids.

5.3 Analysis of conformation distribution and discussion

5.3.1 Characterization of surface conformations

The adherence of the CytC molecules to the exposed Cu grid between the Cu_2N islands leads to a significant reduction of the conformational freedom of the molecules, compared with molecules deposited on plain metal surfaces (for comparison see Figure 5.3a and b). This reduction makes a detailed analysis of all the possible conformations tractable. The ratio of molecule length to island length dictates that each molecule will either fully occupy 5 grid segments or fully occupy 4 segments and its edges will partially occupy 2 segments. In the former case the conformation includes 4 junctions and in the latter it includes 5. At each

5.3. Analysis of conformation distribution and discussion

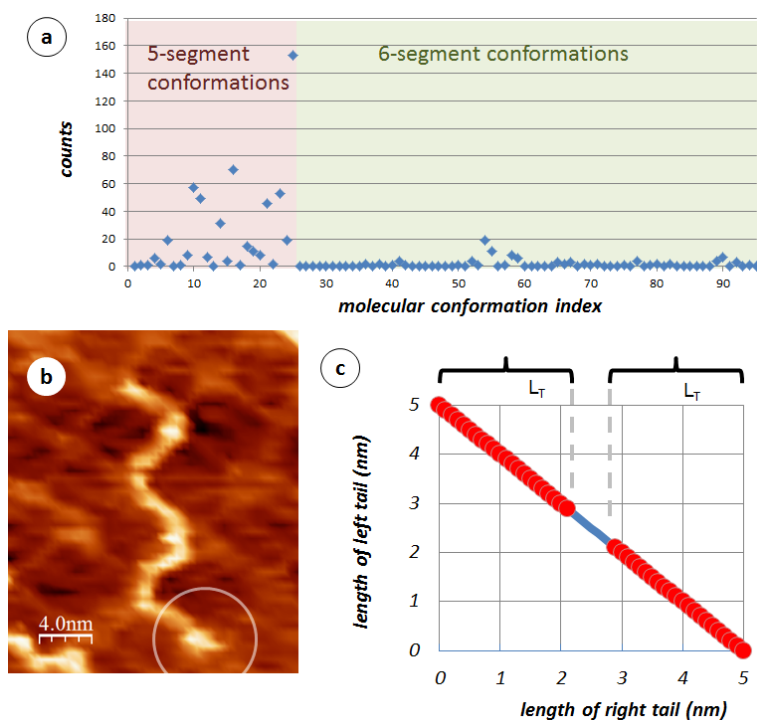


Figure 5.5 – (a) Observed distribution of conformations of CytC on $\text{Cu}_2\text{N}/\text{Cu}(100)$. (b) Possible instance of molecular edge curling. (c) Plot of left tail length vs. right tail length. The red circles indicate molecules where one of the tails is shorter than L_C , and therefore would appear as a 5-segment molecule.

junction three configurations of the segment pair are possible (right turn, straight or left turn). The molecular conformation can therefore be encoded as a number in base 3 with either 4 or 5 digits, making a total of $3^4 + 3^5 = 324$ conformations. This number is, however, larger than the number of conformations one can distinguish in STM images. Every observed molecule can be encoded into two different numbers depending whether one starts counting from the amino terminal of the molecule or from the carboxylic terminal. Since the orientation of a protein cannot be identified in STM, we can only consider the *observable* conformational space. The latter is made up of 25 5-segment conformations and 70 6-segment conformations (binning together enantiomers). In the STM images, individual molecules were analysed manually and their conformations translated into strings made of the letters 'L', 'R' and 'S', representing right, left and straight junctions. The strings were processed with a Matlab script to generate the distribution of observed conformations, binning together equivalent conformations.

5.3.2 Curling of molecule extremities

A most notable property of the distribution of observed conformations (Figure 5.5a) is that 6-segment conformations are found in very small numbers. Although the possible 6-segment conformations outnumber the possible 5-segment conformations nearly 3:1, in the observed

distribution they are outnumbered 1:6. This is a consequence of the imperfection of the Cu_2N grid, specifically of the junctions where grid lines meet. In an ideal grid these junctions would have the same width as the wires themselves, but in the Cu_2N island system the corners of the Cu_2N islands are cropped, which creates Cu rectangles with sides of $1 - 2 \text{ nm}$ (see Figure 5.2a). These will be referred to as “illes” because of their reminiscence of the chamfered street intersection style in Barcelona ¹. The illes provide areas where the ends of the molecules can curl around themselves (see example in Figure 5.5b). Each molecule has two ends, which may extend partially onto Cu_2N grid segments, and the sum of lengths of these two “tails” is 5 nm . We can assume there is a maximal length of tail that will curl (L_C), because of the limited size of the Cu illes. Figure 5.5c plots the possible lengths of the two tails of a molecule. The segments at the edges of the curve (red) represent conformations where one of the tails curls, and the conformation contains only 5 segments. The central part of the graph (blue) represents conformations where both tails are too long to curl, therefore the conformation contains 6 segments. If all the conformations represented on this plot are equally probable, the fraction of 5-segment conformations in the ensemble (C_5) should be equal to the ratio of the red segments’ length and the entire line’s length, also equal to the ratio of their projections on the x-axis. This hypothetical model leads to the relation

$$L_C = 2.5 \text{ nm} \times C_5 \quad (5.1)$$

Using the experimental observation that $C_5 = 0.86$, this analysis yields a curling length of $L_C = 2.14 \text{ nm}$. This result can be compared with the length of protein that can be fitted in an ille, calculated by dividing the average ille area ($1.5 \times 1.5 \text{ nm}^2$) by the molecule’s apparent width. The result of 2.25 nm is in good agreement with the conformations’ ratio analysis, and supports the idea that tail curling is the cause of the low rate of observed 6-segment conformations. Curling can also explain the large distribution of protein lengths ($22 - 30 \text{ nm}$) found. The vanishingly small number of counts for 6-segment conformations makes the relative error of the counting quite large, therefore we limit ourselves to the analysis of 5-segment conformations.

The observation of stable CytC proteins in room temperature STM measurements means that 5 nm segments of the protein are immobilized at room temperature. If it were not so, the last segment of a protein would have been observed flipping between two or three possible orientations. At the same time, the indirect observation that both parallel and perpendicular diffusion are possible indicates that 0.5 nm segments of the protein (the width of a Cu line) are mobile at room temperature. The ability of molecular segments to diffuse away from the Cu lines is limited by the difference in the adsorption energy between Cu(001) and Cu_2N . We denote this diffusion barrier per nm ϵ , and we can infer that $0.2K_B T < \epsilon < 2K_B T$. A better estimate can be obtained by assuming that the curling length describes the longest protein segment which is mobile at room temperature, leading to a rough estimate of the diffusion barrier of $\epsilon = 11.6 \text{ meV/nm}$, or 350 meV per protein. This result is within the same order of

¹These were conceived by architect Ildefons Cerdà, who came up with his unique octagonal block design, where the streets broaden at every intersection making for greater visibility and better ventilation.

magnitude found for the adsorption energy of CytC to polymeric beads in a chromatographic column, 120.4 *meV* [187]. 350 *meV* should, however, be considered a lower bound for the diffusion barrier, because we have no evidence that segments of 2.14 *nm* are mobile at room temperature. It is possible that curling occurs during the motion of the protein towards the Cu grid, and not after it has settled on the grid.

5.3.3 Motivation for the simulation

It is clear that the Cu stripes are energetically favourable adsorption sites and that the proteins have enough mobility to arrange themselves so that the entire length of the protein is on Cu stripes. It is, however, not clear what are the main forces driving the arrangement of the proteins on the grid. For example, is the on-surface mobility sufficient for the molecules to assume a thermodynamic distribution of conformations, where the probability of a conformation depends only on its energy? Alternatively, is the movement on the surface kinetically limited, and the distribution of on-surface conformations retains some information about the gas phase conformations? In order to address this question we performed a simulation assuming an extreme scenario where the surface mobility is strongly hindered. In this scenario, the molecules perform the minimal displacement required to bring the gas phase conformation onto the closest surface conformation. No energetic penalty on bending was imposed due to the high flexibility of protein backbones. The flexibility of a protein backbone can be illustrated using the structure of the α -helix, a common structure in proteins. In an α -helix the backbone performs a 100° turn per amino acid, over a backbone segment of 0.26 *nm* [41]. On Cu₂N, for comparison, a 90° turn is performed over a distance of 1 *nm*, i.e. the bending radius on Cu₂N is 4 times greater the bending radius found in an α -helix. The bends a protein makes in Cu₂N can therefore be considered soft compared with the typical bends found in proteins. The distribution of conformations predicted by this model was calculated using a Matlab script and is a non trivial one. The oppositely extreme scenario is one where the molecular conformations are determined exclusively by the adsorption energies of the conformations. The main contribution to the adsorption energy clearly comes from the contact area with the Cu. The energies of the different conformations are therefore very close, and this scenario would, to the lowest order, predict a uniform distribution of conformations. The next correction to the lowest order prediction would come from the inclusion of the bending energies of the conformations. However, the notion that the probability of a conformation depends on the number of bends will be excluded in the following.

5.3.4 Simulation details

The model consists mainly of 3 parts: generation of gas phase like conformations (called original conformations), generation of on-surface conformations (also called grid conformations) and comparing them to each other. Gas phase conformations are generated by random walks of 11 steps in 2 dimensions, where each step has a length of 2.5 *nm* and each step is taken in a direction of $\pm 22.5^\circ$ with respect to the previous step. The values of 2.5 *nm* and 22.5° were

chosen to produce a curvature radius of $\approx 5 \text{ nm}$, as observed by Rinke et al. [49]². These molecules can be represented by binary numbers of 10 digits, and produce 1024 different conformations, enough to approximate the full distribution of possible gas phase conformations. The reduced set of surface conformations was generated by translating all the base-3 numbers with 4 and 5 digits into grid conformations and constructing an array of equivalents: an array where each row contains all the equivalent strings. Strings are considered equivalent if they represent the same conformation encoded from tail to head, or its enantiomer. Consequently, the row indices of this array provide an (arbitrary) enumeration of the reduced set of grid conformations.

The 1024 gas phase molecules were positioned on the surface at 25 equally spaced positions within the $5 \times 5 \text{ nm}$ surface unit cell and at 4 different orientations of the starting segment, making a total of 102400 starting conformations. The following process was established by which each starting conformation "votes" for the grid conformations it is most likely to adopt. A metric called Δ was established which estimates how much an initial conformation (a gas phase conformation, represented by I) would have to displace in order to reach a specific grid conformation (a grid conformation, represented by F). We use an exponentially decreasing function of Δ in order to determine the amount of vote (V) an initial conformation will give to each grid conformation. The exponential distribution of votes introduces the decay constant k , which plays the role of inverse temperature and adds an easy way to tune the output of the simulation. By choosing a small value of k (analogous to a high temperature) the vote will be distributed among several nearly optimal conformations, simulating a "hot" environment where more transitions are possible. In the limit of $k = 0$ (infinite temperature) the distribution becomes uniform. In the limit of infinite k (zero temperature), each gas phase conformation gives its entire vote to a single grid conformation, which is considered the optimal grid conformation. The amount of vote given to the grid conformation F by the gas phase conformation I is determined by

$$V(I, F) \propto \exp(-k\Delta_{(I,F)}) \quad (5.2)$$

which is normalized to a single vote per gas phase conformation. Δ is defined as follows:

$$\Delta(I, F) = \sqrt{\sum_{i=1}^{11} (x_i^F - x_i^I)^2 + (y_i^F - y_i^I)^2} \quad (5.3)$$

In order to determine Δ for a pair of conformations, it is necessary to test various positions and rotations of the grid conformation in order to find the closest position to the gas phase

²Generating the gas phase molecules in this way strictly limits the molecular curvature, and therefore does not reproduce the distribution of moments of the worm like chain model [188] and does not have a well defined persistence length to compare with [49].

5.3. Analysis of conformation distribution and discussion

conformation. Each gas phase conformation was therefore compared with 1800 versions of each grid conformation, representing 225 shifts, 4 rotations and a reflection (for a total of 17.5 billion calculations of Δ).

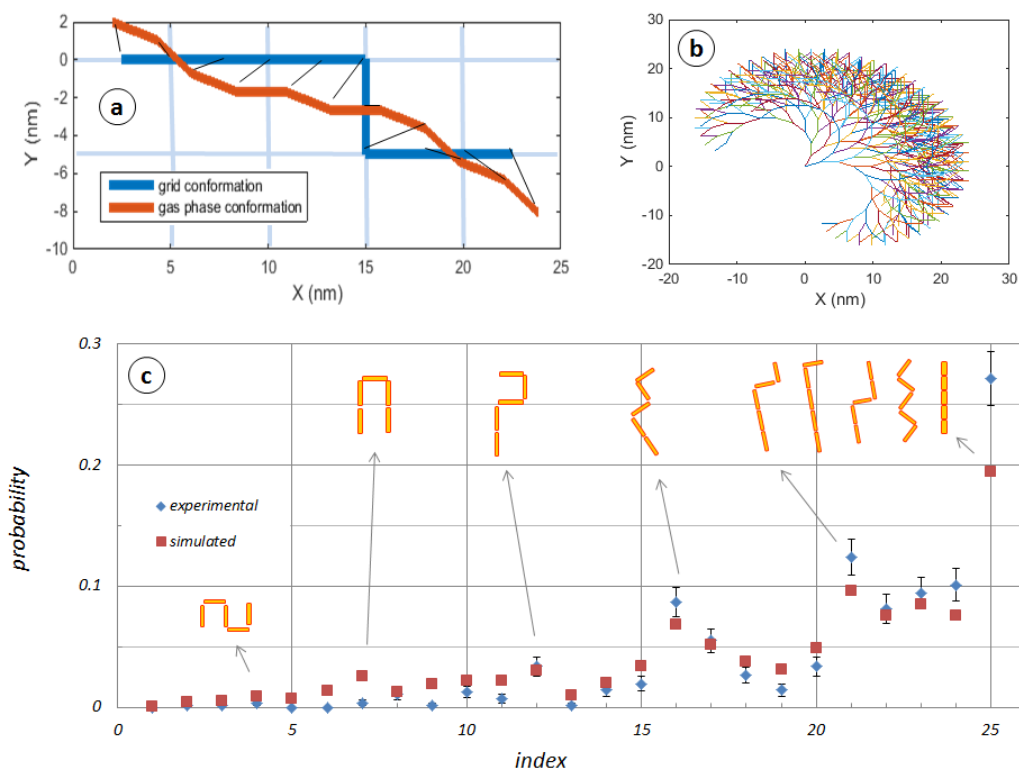


Figure 5.6 – (a) Illustration of the calculation of Δ for a specific pair of gas phase (red) and grid (blue) conformations. (b) Full set of original conformations used in the simulation. (c) Simulation predictions (red) and experimental results (blue) of the distribution of conformations of CytC on $\text{Cu}_2\text{N}/\text{Cu}(111)$. Indices are ordered according to length of corresponding conformations. Some of the grid conformations are depicted for illustration.

5.3.5 Simulation results and analysis

In Figure 5.6c, the results of the simulation for $k = 0.3 \text{ nm}^{-1}$ are compared with the observed distribution of conformations (this particular value of k is discussed below). The indices were ordered according to the maximal segment that can be fitted in the conformation. The observed distribution of conformations is far from uniform, and is well reproduced by the simulation. The rising trend indicates that both simulation and experiment favour extended conformations, due to the absence of compactly folded molecules in the gas phase. This is an indication that the conformations observed in STM retain some information about the gas phase conformations. The probability distribution of the simulation is slightly more uniform than the observed data, which can be attributed to the temperature of the simulation or to the

non-uniform distribution of the gas phase molecules in the experiment. Having 12 positive charges, extended conformations may be more common in the gas phase than the more compact ones. As a consequence, the probabilities of the longer conformations are underestimated in the simulation. The success of the simulation confirms that the exact positions of the chemically different side chains do not influence the distribution of conformations, probably due to an averaging effect. The two rightmost conformations in Figure 5.6c exclude the possibility that the frequencies of the conformations are related to bending energy. The most common conformation is the completely straight protein, while the fifth most common conformation is one who contains the maximal number of bends. If the distribution were dependent on bending energy, the molecules with a significantly different number of turns would have been observed with significantly different probabilities.

5.3.6 Choice and meaning of inverse temperature k

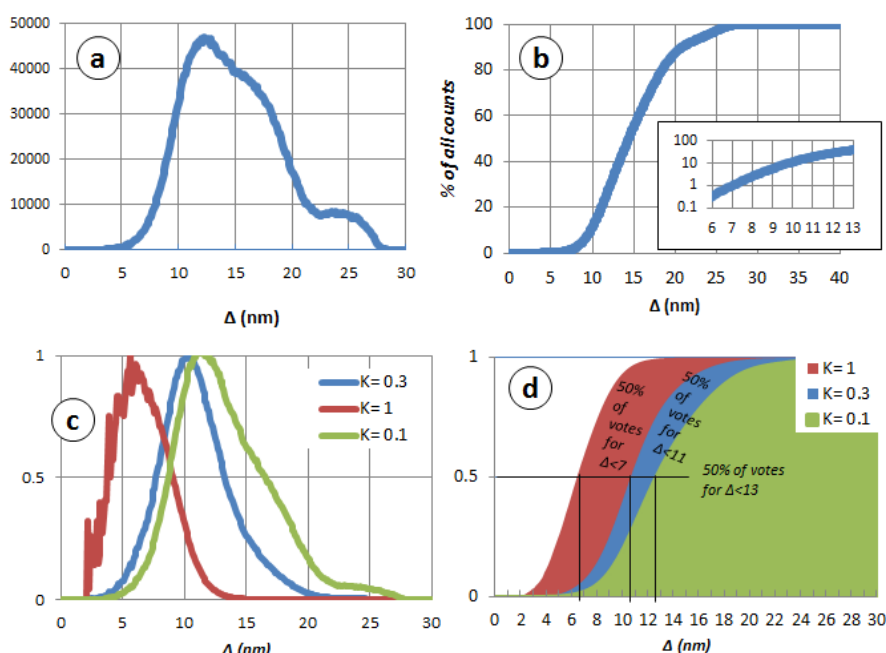


Figure 5.7 – (a) Histogram of values of Δ . (b) Cumulative histogram of values of Δ . Inset: semi logarithmic plot of the transition region. (c) Normalized participation indices plotted for $k = 0.1 \text{ nm}^{-1}$, 0.3 nm^{-1} and 1 nm^{-1} . (d) Cumulative normalized participation indices plotted for $k = 0.1 \text{ nm}^{-1}$, 0.3 nm^{-1} and 1 nm^{-1} .

As mentioned earlier, the value of k determines whether each gas phase conformation will vote for a single grid conformation (in the zero temperature limit), vote for all grid conformation equally (in the infinite temperature limit) or something in between. The ability to scan fully immobilized CytC proteins at room temperature (see Figure 5.5b) indicates that the correct limit for room temperature deposition is the low temperature limit. However, as k is a parameter that introduces disorder into the simulation, we can use it to account for

another type of disorder. The random initial velocity and angular momentum of a deposited protein may hurl it, even at zero temperature, towards a grid conformation which is not the optimal grid conformation (based on its shape). In order to capture some of this randomness, we need a value of k where a significant percentage of the vote is given to non optimal conformations. This section describes how we determine this value of k . Since the distribution of Δ is independent of k , this distribution can be used to determine of how many "nearly optimal conformations" get voted for as a function of k . In order to study this distribution, we run the simulation while saving all the values of Δ which are calculated, producing the histogram in Figure 5.7a. The following analysis of the histogram is done in order to avoid running the simulation on various values of k , as the simulation running time is very long.

Since the optimal grid conformations make up 0.052% of all grid conformations (only one optimal conformation per gas phase molecule), one might expect that they account for the lowest 0.056% values of Δ . But this is true only if optimal gas phase - grid molecule pairs yield the lowest values of Δ . Since this is not the case, we assume that the Δ values of the optimal conformations are mixed into the lowest 1% of Δ s. As can be seen in the inset of Figure 5.7b, this means that the optimal values of Δ are typically 7 nm. We now weight the histogram of the Δ s by $e^{-k\Delta}$, which gives an indication of how much of the vote each Δ will receive. This "participation index" is depicted in Figure 5.7c for $k = 0.1, 0.3$ and 1 nm^{-1} . These curves show how the higher the value of k , the more votes are concentrated in lower values of Δ . The integrated participation index (Figure 5.7d) shows which range of Δ gets 50% of the votes, depending on k . For $k = 1 \text{ nm}^{-1}$ the majority of the votes go to conformations for which $\Delta < 6 \text{ nm}$. For $k = 0.3 \text{ nm}^{-1}$, half of the votes go to conformations for which $\Delta < 10 \text{ nm}$, and for $k = 0.1 \text{ nm}^{-1}$, 50% of the votes go to conformations for which $\Delta < 13 \text{ nm}$. The inset in Figure 5.7b helps make sense these values: for $k = 1 \text{ nm}^{-1}$ half the vote goes to the bottom 0.8% of Δ s, or mostly to the optimal conformations (which we assume are among the lowest 1%). For $k = 0.3 \text{ nm}^{-1}$, half the vote goes to the bottom 10% of Δ s, so the votes are distributed also to some near optimal conformations. For $k = 0.1 \text{ nm}^{-1}$ half the vote goes to the bottom 60% of Δ , which represents a significant redistribution of votes, and demonstrates that these three values of k capture well the transition from a "frozen" system to a "hot" system. The value of $k = 0.3 \text{ nm}^{-1}$ best represents the idea of slight redistribution, where the optimal grid conformations do not get the entire vote, and this notion introduces the effects of the uncertainty in the initial velocity and angular momentum of the incoming proteins.

Because of the criteria used to determine the value of k , its value does not describe the energy barrier for molecular displacement between Cu lines. If we were to use the previously calculated diffusion energy barrier of $\epsilon = 11.6 \text{ meV/nm}$, we could estimate what is the effective temperature (T_E) that $k = 0.3 \text{ nm}^{-1}$ represents using the equation

$$k\Delta = \frac{\epsilon\Delta}{K_B T_E} \quad (5.4)$$

where K_B is the Boltzmann constant. Thus we get that $T_E = 450 \text{ K}$, 150 K hotter than room temperature. The increased temperature adds disorder to the simulation, which is designed

to compensate for the random initial velocities and angular momenta of the proteins, which are not explicitly accounted for in the simulation. According to the diffusion barrier of $\epsilon = 11.6 \text{ meV/nm}$, the accurate value of k at room temperature would be 0.45 nm^{-1} .

As we have already noticed in Figure 5.7b, the optimal conformations tend to have $\Delta < 7 \text{ nm}$. This means that on the average, every point of the protein travels 2.1 nm from the gas conformation to the grid conformation. For comparison, if the atoms of a protein were dropped one by one at random positions on the Cu_2N islands, they would travel an average of 0.83 nm before reaching the nearest Cu stripe. In our case the atoms are part of a chain, so they are not free to take the shortest path to the nearest Cu stripe, and the average movement per atom is expected to be longer.

5.3.7 Conclusions

In this chapter it was shown how a detailed observation of the molecular conformations can lead to a good understanding on the adsorption process, and even to quantitative results. The fitting of the proteins to the Cu grid suggests that parallel and perpendicular diffusion are possible at room temperature. STM measurements at room temperature suggest that 5 nm protein segments are immobile at this temperature. The minimal curling length is calculated in two different ways, yielding an estimate of the shortest molecular segment that is mobile at room temperature - 2.2 nm . This length provides a lower bound for the diffusion barrier energy, 350 meV , which is in the same order of magnitude as the adsorption energy of CytC on polymeric beads [187].

The agreement between the simulation output and the experimental results provides support for the assumptions incorporated in the model. The main assumption in the simulation is the notion that on-surface molecular mobility is strongly limited due to the attractive potential of the Cu lines. Additionally, the observed distribution of conformations can rule out that the probabilities of conformations depends on their energy. Earlier observations of CytC made on plain metal surfaces [49] have shown that the on-surface conformations of CytC deposited by ES-IBD retain some information about the gas phase. It is now evident that some information is also retained on nanopatterned surfaces. An additional assumption, implicitly incorporated into the simulation by neglecting the different chemical properties of the side-chains, is the relative homogeneity of the protein. In small molecules, chemical properties have a decisive role in determining the molecular on-surface conformation, however, the presence of so many different chemical groups appears to average out in such a large molecule. This is likely to be a statistical effect similar to the "law of large numbers". For most molecular conformations, 5-7 side chains are in contact with the Cu grid. The adsorption energy is therefore composed roughly of the sum of the adsorption energy of these 5-7 groups, plus unspecific potentials such as van der Waals. By virtue of elementary statistics, the sum of adsorption potentials of five side chains has a narrower distribution than the energy of a single side chain, making most conformations similar in energy. An additional implicit assumption is incorporated by

not imposing energetic penalties on bending. This assumption is justified by the flexibility that protein backbones display in a common structure such as the α -helix. In practice, the flexibility of proteins even varies locally, due to steric hindrance induced by large side-chains, and due to the presence of relatively stiff proline moieties. This implicit assumption suggests that the backbone is flexible enough to easily adhere to the bending radius of 1 nm imposed by the Cu_2N grid. This simulation can be the basis of more advanced simulations, as progress in the deposition of low energy ions of large molecules from the gas phase [4, 189] will create demand for improved predictions.

5.3.8 Pre-patterning effect

We have discussed the transition of molecules from their gas phase conformations to the grid conformations as a process that occurs once the molecules are on the surface. It should be noted that the surface starts to exercise electrostatic forces during the last few nanometres before the landing. For ions deposited at low energies, these forces can affect the molecule's shape already before landing and have a pre-patterning effect. One way that a surface might affect the incoming ion is through surface dipoles. If the topmost layer of atoms is charged, when the ion approaches to a distance of few nm, its closer proximity to the top layer will result in a force in the direction perpendicular to the surface, with an accelerating/decelerating effect. If the strength of the dipole layer varies laterally across the sample surface, this will result in a net attraction to certain areas, hence to lateral forces. In our present system, the top layer of Cu_2N has a net negative charge of $0.2e$ per unit cell [183], meaning it is attractive to the incoming proteins, which carry either +12 or +13 positive charges each. But pre-patterning only occurs if the Cu_2N is *more* attractive than the bare Cu. This can be deduced from WF measurements performed by Ruggiero et al. [190], where it was found that the WF is higher on Cu_2N than on Cu, suggesting it had a stronger dipole layer, and therefore a higher density of negative charge. An additional mechanism of pre-patterning arises from lateral variation of image charges' positions. The Cu_2N islands are insulating, therefore the reflection plane that defines the position of the image charge is lower on the Cu_2N islands than it is on the bare Cu. An ion hovering near a Cu_2N island will produce an image charge which is further away, and therefore less attractive, than the image charge of an ion above a clean Cu stripe (see Figure 5.8a). The result is a lateral electric field pushing ions towards the bare Cu (regardless of the ion's charge).

For the Cu_2N system, the effect of the dipole layer attracts positive ions to the Cu_2N while the image charge effect attracts ions to the Cu. For the purpose of illustrating the very idea of pre-patterning, we calculate the effect of the image charge potential alone, neglecting dipole attraction. We use a point particle with a single electron charge and the mass of CytC (12000 daltons). The electrostatic potential is presented in Figure 5.8b (yellow). The figure shows that the energy difference associated with the varying position of the image charge becomes comparable to the deposition energy during the last 1 nm of approach. This energetic

difference is used to calculate lateral force, F_x using the relation

$$F_x = \frac{dU}{dr} = \frac{U_{diff}}{z} \quad (5.5)$$

where U_{diff} is the difference between the energies of the image potentials on the Cu and on the Cu₂N, and z is the particle's distance from the surface. This leads to lateral forces rising from 1 pN to 10000 pN within the last nm of approach (5.8c). Integrating the lateral acceleration during the approach, lateral velocities are found to rise from 1 m/s to 50 m/s (5.8d). The lateral displacement is calculating by integrating the lateral velocity, and amounts to 1.2 nm (5.8e), which indicates that this effect can be significant. Many of these forces will cancel each other out when they are applied to charges along a chain, but the net effect is to funnel the molecule towards the Cu stripes even before they come into contact with the surface. Interestingly, pre-patterning due to image charges should be a general phenomenon, which occurs on any metal at step edges. It would be more easily quantified by depositing small ions, such as single atoms or small molecules, on a highly reactive metal and observing the distribution of positions below and above a step edge, as a function of distance from the step.

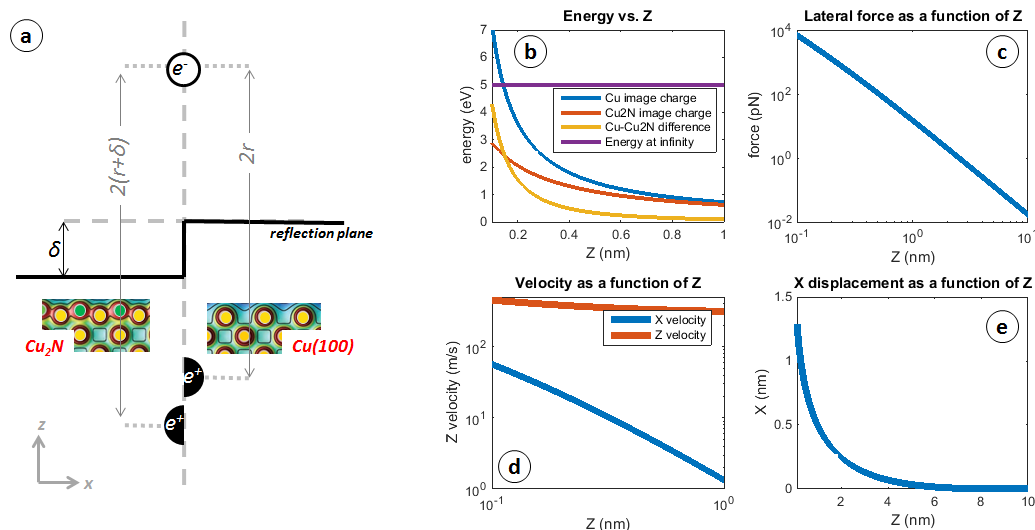


Figure 5.8 – (a) positions of image charges of an incoming ion on the metal, where the image plane is higher (right), and on the Cu₂N where the image plane is lower (left). (b) Energy vs. distance plot of the image charge on Cu (blue), on Cu₂N (red) and the difference (yellow). The plot shows that at the last nm of approach, the energy difference between the two areas becomes comparable to the deposition energy (purple). The last \AA is not included as the image potential saturates at this distance [191]. (c) The lateral force as a function of distance increases by four orders of magnitude during the last 10 nm of approach. (d) Lateral (blue) and perpendicular (red) velocities as a function of distance z from the sample. The lateral velocity can be seen in the range of several m/s during the last nm of approach. z speed also increases due to attraction to the image charge. (e) Lateral displacement as a function of distance reaches 1.2 nm at the last \AA before impact.

6 Summary and Outlook

This chapter presents a summary of the previous chapters, together with suggestions for follow-up experiments in the near future, as well as an outlook for the development of experiments on the long run.

6.1 Prospects for the STM

The second chapter of this thesis describes the constructions of a STM operating in UHV at liquid helium temperature, combined with an UHV chamber for sample preparation and MBE. The finished STM was shown to operate successfully and provide atomic resolution topographic images as well as spectroscopic measurements. The vibration level achieved is sufficient for imaging and spectroscopy. Most characteristics of this STM are on par with the state of the art, while the cables were designed to sustain *GHz* frequencies in order to provide time resolution of few nanoseconds using the electrical pump-probe technique [1]. The cabling developed meets our UHF, low temperature, low vibration specifications. However, high frequency signals are not able to reach the tunnel junction due to the presence of home made coaxial connectors, which have not yet been replaced with panel-mounted SMA connectors. All the necessary preparations for this modification have been done, and they will be implemented in the next few months.

The STM is still under construction in other respects. Small modifications such as the introduction of a sample carousel and fixing the He cryostat to the N₂ cryostat, in order to reduce the vibration, will be carried out in the near future. The setup was also designed to support in-situ sample illumination with a laser. This will still require the installation of adequate windows on the chamber and the radiation shields, and modifying the STM head with mirrors and holes along the path of the laser. The laser will be used to study optically induced switching of single molecules and molecular assemblies. The parts required for this modification are under construction. Similar modifications are required in order to allow in-situ evaporation of atoms and molecules while the sample is in the STM head, at 5K. The latter is a practical way to immobilize small molecules on the surface in order to address individual molecules, which

tend to aggregate at elevated temperatures. On the longer run, plans are under way to build an alternative STM head with a combined STM-AFM capability, thanks to recent advances in non-contact AFM [192] that allow a reliable cantilever deflection readout without the use of a laser. The UHF capabilities are not compatible with the use of a cantilever, however, the system is highly modular and allows STM heads to be exchanged easily. The additional scan head will give the machine access to high resolution imaging techniques based on a CO functionalized AFM tip [193]. Additionally, the measurement of force is useful for the identification of molecular subunits according to their stiffness.

6.2 Local WF variation measurements on h-BN/Rh(111)

The third chapter of this thesis takes a deep look into WF variations and FER lifetimes on h-BN/Rh(111). This is a fairly well understood system [3] which is an ideal template for STM studies of molecules, thanks to the combination of electronic decoupling from the metallic substrate [137] and its capacity to isolate molecules in its valleys [136]. In order to use this system as a platform for studying molecules, a better understanding of its electronic properties is needed. It is therefore necessary to reach experimental and theoretical agreement regarding the WF variations, due to their role in the trapping capacity of this surface. Our results support previous experimental results [2] and highlight the challenge that even tunnelling based methods face when probing WF variations on such a small scale, on a highly corrugated layer. Analysis of FER spectra shows surprising complexity with the appearance of a second standing wave mode in the valleys.

FER peak width analysis provides only a lower bound for FER lifetime, and yet these lower bounds match the longest known lifetimes of IPSs on h-BN/Ni(111) [142]. Based on comparison of graphene IPS lifetimes on metals to the lifetimes of IPSs on h-BN, it appears that the insulating layers promote IPS lifetimes. Observations made on other systems [145, 111, 107, 88] suggest that FER lifetimes are prolonged in laterally confined structures, and we offer a qualitative argument for this phenomenon. Theory as well as 2PPE experiments could resolve the exact lifetime of these states and elucidate the origin of the extended lifetimes. These observations open the way to intentional IPS lifetime engineering. If lifetimes exceeding 1 ps can be engineered by tailoring the size and shape of nanostructures, then the FER lifetime can be measured not only through the peak width but also through the current dependence of the heights (z) where FERs are observed. At these time scales, Coulomb blockade could be reached, depending on the current set point that is used, and the onset of Coulomb blockade would provide an additional indication of the FER lifetime. If lifetimes could be increased by three orders of magnitude, the time scale of FER states would become accessible to the electrical pump-probe technique mentioned earlier [1]. This would make an ideal system for this technique as it provides a strong contrast, and endlessly repeatable experiments. This would be easier to achieve using the higher FERs whose lifetimes are significantly longer [194].

Lastly, a new stable phase of h-BN/Rh(111) is observed and its potential origin is discussed. The new phase will be studied to determine its exact structure, the conditions required to produce it, its stability and potential functionality. h-BN is useful as a passivating layer on metals [195], however controlled defects could enhance its capacity to trap and immobilize adsorbates, while still conserving their magnetic and electronic properties [137]. Periodic arrays of immobilized adsorbates can even lead to the emergence of new optical properties [196], potentially making it a multifunctional coating. We will therefore test the effect of variations in the growth parameters on the abundance of the new phase, as well as its reactivity towards exposure to various gases. Theory as well as XPS measurements will hopefully allow us to determine the structure of the layer.

6.3 Peptide sequencing

The fourth chapter of this thesis presents ongoing experiments towards peptide sequencing by means of STM. Initial experiments of At-II/Cu(111) show that the size and flexibility of the peptides lead to a complex adsorption behaviour, strongly influenced by the substrate. Monomers, dimers and three types of trimers were observed, some potentially incorporating Cu atoms. All structures exhibit a clear chiral preference. An effect of the second Cu layer is affecting the distribution of conformations of the C-type trimer. However, understanding the conformational arrangement of peptides viewed by STM is extremely challenging without knowing the positioning of the amino acids, or even the orientation of the peptide. Peptide sequencing, or even partial sequencing, would therefore be tremendously advantageous. In this work we observe that dI/dV spectroscopy shows no peaks for molecules deposited on Cu(111), but a peak at the main bulge of the molecule can be observed for At-II/h-BN/Rh(111). This is an encouraging sign that the electronic states of At-II can be detected when the peptide is properly isolated from the metallic substrate, and that an electronic feature can be correlated with a structural feature.

Peptides pose a challenge to the well established technique of STS, mainly due to the irregular shapes that the peptides adopt. On a flat molecule, spectra taken at different parts of the molecule can be compared, provided that they were measured with the tip at a constant height. If the molecular aspect is not flat, it is not clear whether features are intensified due to the tip proximity to the molecule or to a high LDOS. Similarly, if the tip is stabilized at a constant current on different parts of the molecule, then the effect of the substrate varies from spectrum to spectrum. This difficulty can be addressed with a combination of experimental procedure and data analysis. For example, the substrate spectrum can be weighted by the tip height before it is subtracted. dI/dV maps can be divided by the simultaneously acquired I , in order to neutralize effects of proximity. Such procedures should however be demonstrated on benchmarked systems first.

Naturally, other modes of operating the STM can provide complementary information. IETS could be correlated with known vibrations of specific bonds [138] or side chains, although this technique is significantly more demanding than STS. WF maps could be used to identify charged side chains. STM with functionalized tips could provide a different contrast mechanism. The implementation of non-contact AFM would introduce local stiffness as an additional way to distinguish amino acids, while CO terminated AFM tips have been shown to provide excellent contrast on flat molecules [193].

As mentioned earlier, the ease with which peptides can be designed and synthesized can work to our advantage. If the high flexibility of the peptides and their irregular shapes pose a challenge to the identification of amino acids, peptides may be engineered where these problems are alleviated, and a few possible paths are proposed. Proline is known to make stiffer peptide bonds than the rest of the amino acids [174], therefore peptides with a high proportion of prolines would show less flexibility. It is perhaps possible to deposit proteins with polyproline helices [174], which are some of the stiffest structures made of amino acids. Alternatively, peptides can be designed to lay flat on the surface and thus facilitate spectroscopic measurements. Aromatic and sulphur containing side chains (such as in phenylalanine [174]) would provide a strong attraction to the surface [163] and thus pull the peptide to lay flat on the surface. The steric hindrance caused by a series of large side chains [174] could be overcome by introducing small spacers between the phenylalanine residues, such as the small amino acid glycine. The use of WF maps to identify amino acids could benefit from the incorporation of amino acids with a high electron affinity, which are negatively charged at physiological conditions, such as aspartic acid [174], or amino acids with a low electron affinity such as arginine [174]. Purposefully engineering peptide structures to facilitate STS is in itself a step towards understanding and controlling the self assembly of peptides. Peptide sequences that can test the ideas presented here have already been acquired and will soon be deposited using the ES-IBD and examined by STM.

6.4 Modeling the adsorption of large molecules on nanostructures

The fifth chapter of this thesis shows an example of using the Cu_2N , a self-assembled square island pattern known from surface science [48], for the patterning of large proteins, namely CytC. We find that the attractive potential of the exposed Cu lines between the Cu_2 islands draws the proteins to adhere to the grid and remain stable at room temperature. The diffusion mechanisms can be inferred from a detailed observation of the molecular conformations. The molecular adsorption energy can be estimated using an argument based on counting 6-segment and 5-segment conformations. The result, 350 *meV*, is in the same order of magnitude of the adsorption of CytC on polymeric beads (120 *meV* [187]).

6.4. Modeling the adsorption of large molecules on nanostructures

A rudimentary simulation was devised in order to explain the experimentally observed distribution of conformations. From the surprisingly fit we conclude that the on-surface mobility of the molecules is strongly limited by the attractive potential of the Cu grid, thus retaining some information about the gas phase conformations. In addition, the simulation results suggest that the chemical and mechanical properties of individual amino acid side chains have no significant influence on the conformations adopted by the proteins.

The model will benefit from a few elaborations. For one, the gas phase conformations can be generated by self-avoiding random walks rather than the tree-style process currently in use. This will better reproduce the statistical properties of the worm-like chain model [188] and allow the tuning of their persistence length. Additionally, the gas phase molecules are not necessarily equally probable, and their contribution can be weighted by a Boltzmann distribution of their electrostatic energy.

The model for CytC adsorption on Cu₂N presented in this work demonstrates the ability of a simplified, tailor made simulation to capture the main characteristics of a complex system with enormous conformational freedom. Hopefully, the need for such models will diminish with the increasing computational power and the increasing sophistication of modeling software [197]. For large systems with low symmetries, tailor-made models still provide the best opportunity for hypothesis testing. The relevance of the model evaluated in this work is not limited to proteins or Cu₂N, but could be applied to any flexible polymer, transitioning from the gas phase to a periodic nanostructure. Although this scenario is not commonly found in polymers, where solution processing is the norm, developments in ES-IBD based preparation methods [4, 198, 199] will require simulations of this kind in order to rationalize and predict their observations.

Bibliography

- [1] Sebastian Loth, Markus Etzkorn, Christopher P Lutz, D M Eigler, and Andreas J Heinrich. Measurement of fast electron spin relaxation times with atomic resolution. *Science (New York, N.Y.)*, 329(5999):1628–30, September 2010.
- [2] Hugo Dil, Jorge Lobo-Checa, Robert Laskowski, Peter Blaha, Simon Berner, Jürg Osterwalder, and Thomas Greber. Surface trapping of atoms and molecules with dipole rings. *Science (New York, N.Y.)*, 319(5871):1824–6, March 2008.
- [3] Jaime Gómez Díaz, Yun Ding, Ralph Koitz, Ari P. Seitsonen, Marcella Iannuzzi, and Jürg Hutter. Hexagonal boron nitride on transition metal surfaces. *Theoretical Chemistry Accounts*, 132(4):1350, February 2013.
- [4] Stephan Rauschenbach, Ralf Vogelgesang, N Malinowski, Jürgen W Gerlach, Mohamed Benyoucef, Giovanni Costantini, Zhitao Deng, Nicha Thontasen, and Klaus Kern. Electrospray ion beam deposition: soft-landing and fragmentation of functional molecules at solid surfaces. *ACS nano*, 3(10):2901–10, October 2009.
- [5] Zhitao Deng, Nicha Thontasen, Nikola Malinowski, Gordon Rinke, Ludger Harnau, Stephan Rauschenbach, Klaus Kern, Ludger Harnau, Stephan Rauschenbach, and Klaus Kern. A close look at proteins: Submolecular resolution of two- and three-dimensionally folded cytochrome c at surfaces. *Nano Letters*, 12(5):2452–2458, May 2012.
- [6] Jean-Marie Lehn. Perspectives in Supramolecular Chemistry—From Molecular Recognition towards Molecular Information Processing and Self-Organization. *Angewandte Chemie International Edition in English*, 29(11):1304–1319, November 1990.
- [7] J B Pendry, D Schurig, and D R Smith. Controlling electromagnetic fields. *Science (New York, N.Y.)*, 312(5781):1780–2, June 2006.
- [8] S. L. Silva, C. R. Jenkins, S. M. York, and F. M. Leibsle. Fabricating nanometer-scale Co dot and line arrays on Cu(100) surfaces. *Applied Physics Letters*, 76(9):1128, February 2000.
- [9] Stuart S P Parkin, Masamitsu Hayashi, and Luc Thomas. Magnetic domain-wall racetrack memory. *Science (New York, N.Y.)*, 320(5873):190–4, April 2008.

Bibliography

- [10] Hong Xiao. *Introduction to Semiconductor Manufacturing Technology*. Prentice Hall, 2001.
- [11] T Ito and S Okazaki. Pushing the limits of lithography. *Nature*, 406(6799):1027–31, August 2000.
- [12] Vitor R Manfrinato, Lihua Zhang, Dong Su, Huigao Duan, Richard G Hobbs, Eric A Stach, and Karl K Berggren. Resolution limits of electron-beam lithography toward the atomic scale. *Nano letters*, 13(4):1555–8, April 2013.
- [13] G. Whitesides, J. Mathias, and C. Seto. Molecular self-assembly and nanochemistry: a chemical strategy for the synthesis of nanostructures. *Science*, 254(5036):1312–1319, November 1991.
- [14] Joona Bang, Unyong Jeong, Du Yeol Ryu, Thomas P Russell, and Craig J Hawker. Block copolymer nanolithography: translation of molecular level control to nanoscale patterns. *Advanced materials (Deerfield Beach, Fla.)*, 21(47):4769–92, December 2009.
- [15] Gérard Férey. Hybrid porous solids: past, present, future. *Chemical Society reviews*, 37(1):191–214, January 2008.
- [16] Ryan J. Kuppler, Daren J. Timmons, Qian-Rong Fang, Jian-Rong Li, Trevor A. Makal, Mark D. Young, Daqiang Yuan, Dan Zhao, Wenjuan Zhuang, and Hong-Cai Zhou. Potential applications of metal-organic frameworks. *Coordination Chemistry Reviews*, 253(23-24):3042–3066, December 2009.
- [17] Stephan Förster and Markus Antonietti. Amphiphilic Block Copolymers in Structure-Controlled Nanomaterial Hybrids. *Advanced Materials*, 10(3):195–217, February 1998.
- [18] Yiyong Mai and Adi Eisenberg. Self-assembly of block copolymers. *Chemical Society reviews*, 41(18):5969–85, September 2012.
- [19] Job Boekhoven and Samuel I Stupp. 25th anniversary article: supramolecular materials for regenerative medicine. *Advanced materials (Deerfield Beach, Fla.)*, 26(11):1642–59, March 2014.
- [20] Markus Antonietti, Eckhard Wenz, Lyudmila Bronstein, and Mariana Seregina. Synthesis and characterization of noble metal colloids in block copolymer micelles. *Advanced Materials*, 7(12):1000–1005, December 1995.
- [21] Roman Glass, Martin Müller, and Joachim P Spatz. Block copolymer micelle nanolithography. *Nanotechnology*, 14(10):1153–1160, October 2003.
- [22] Thomas Tarring, Niels V Voigt, Jeanette Nangreave, Hao Yan, and Kurt V Gothelf. DNA origami: a quantum leap for self-assembly of complex structures. *Chemical Society reviews*, 40(12):5636–46, December 2011.

-
- [23] Quan Li, Gad Fuks, Emilie Moulin, Mounir Maaloum, Michel Rawiso, Igor Kulic, Justin T Foy, and Nicolas Giuseppone. Macroscopic contraction of a gel induced by the integrated motion of light-driven molecular motors. *Nature nanotechnology*, 10(2):161–5, February 2015.
- [24] Euan R Kay, David A Leigh, and Francesco Zerbetto. Synthetic molecular motors and mechanical machines. *Angewandte Chemie (International ed. in English)*, 46(1-2):72–191, January 2007.
- [25] Johannes A A W Elemans, Shengbin Lei, and Steven De Feyter. Molecular and supramolecular networks on surfaces: from two-dimensional crystal engineering to reactivity. *Angewandte Chemie (International ed. in English)*, 48(40):7298–332, January 2009.
- [26] Artur Ciesielski, Carlos-Andres Palma, Massimo Bonini, and Paolo Samorì. Towards supramolecular engineering of functional nanomaterials: pre-programming multi-component 2D self-assembly at solid-liquid interfaces. *Advanced materials (Deerfield Beach, Fla.)*, 22(32):3506–20, August 2010.
- [27] Johannes V Barth, Giovanni Costantini, and Klaus Kern. Engineering atomic and molecular nanostructures at surfaces. *Nature*, 437(7059):671–9, September 2005.
- [28] Tibor Kudernac, Shengbin Lei, Johannes A A W Elemans, and Steven De Feyter. Two-dimensional supramolecular self-assembly: nanoporous networks on surfaces. *Chemical Society reviews*, 38(2):402–21, February 2009.
- [29] Johannes V. Barth. Fresh perspectives for surface coordination chemistry. *Surface Science*, 603(10-12):1533–1541, June 2009.
- [30] Sebastian Stepanow, Magalí Lingenfelder, Alexandre Dmitriev, Hannes Spillmann, Erik Delvigne, Nian Lin, Xiaobin Deng, Chengzhi Cai, Johannes V Barth, and Klaus Kern. Steering molecular organization and host-guest interactions using two-dimensional nanoporous coordination systems. *Nature materials*, 3(4):229–33, April 2004.
- [31] Svetlana Klyatskaya, Florian Klappenberger, Uta Schlickum, Dirk Kühne, Matthias Marschall, Joachim Reichert, Régis Decker, Wolfgang Krenner, Giorgio Zoppellaro, Harald Brune, Johannes V. Barth, and Mario Ruben. Surface-Confined Self-Assembly of Di-carbonitrile Polyphenyls. *Advanced Functional Materials*, 21(7):1230–1240, April 2011.
- [32] Pietro Gambardella, Sebastian Stepanow, Alexandre Dmitriev, Jan Honolka, Frank M F de Groot, Magalí Lingenfelder, Subhra Sen Gupta, D D Sarma, Peter Bencok, Stefan Stanescu, Sylvain Clair, Stéphane Pons, Nian Lin, Ari P Seitsonen, Harald Brune, Johannes V Barth, and Klaus Kern. Supramolecular control of the magnetic anisotropy in two-dimensional high-spin Fe arrays at a metal interface. *Nature materials*, 8(3):189–193, March 2009.

Bibliography

- [33] Doris Grumelli, Benjamin Wurster, Sebastian Stepanow, and Klaus Kern. Bio-inspired nanocatalysts for the oxygen reduction reaction. *Nature communications*, 4:2904, January 2013.
- [34] Arie Aviram and Mark A. Ratner. Molecular rectifiers. *Chemical Physics Letters*, 29(2):277–283, November 1974.
- [35] G. Schmid and W. Hofheinz. Total synthesis of qinghaosu. *Journal of the American Chemical Society*, 105(3):624–625, February 1983.
- [36] Jin-Feng Jia, Xucun Ma, Xi Chen, T Sakurai, and Qi-Kun Xue. STM and MBE: one of the best combinations. *Journal of Physics D: Applied Physics*, 44(46):464007, November 2011.
- [37] Kenneth Whitten, Raymond Davis, Larry Peck, and George Stanley. *Chemistry*. Cengage Learning, 2013.
- [38] Elba Gomar-Nadal, Josep Puigmartí-Luis, and David B Amabilino. Assembly of functional molecular nanostructures on surfaces. *Chemical Society reviews*, 37(3):490–504, March 2008.
- [39] S. Voss, M. Fonin, U. Rüdiger, M. Burgert, U. Groth, and Yu. S. Dedkov. Electronic structure of Mn 12 derivatives on the clean and functionalized Au surface. *Physical Review B*, 75(4):045102, January 2007.
- [40] Steffen Kahle, Zhitao Deng, Nikola Malinowski, Charlene Tonnoir, Alicia Forment-Aliaga, Nicha Thontasen, Gordon Rinke, Duy Le, Volodymyr Turkowski, Talat S Rahman, Stephan Rauschenbach, Markus Ternes, and Klaus Kern. The quantum magnetism of individual manganese-12-acetate molecular magnets anchored at surfaces. *Nano letters*, 12(1):518–21, January 2012.
- [41] Jeremy M Berg, John L Tymoczko, and Lubert Stryer. *Biochemistry*, 2002.
- [42] R. B. Merrifield. Solid Phase Peptide Synthesis. I. The Synthesis of a Tetrapeptide. *Journal of the American Chemical Society*, 85(14):2149–2154, July 1963.
- [43] Robert Bruce Merrifield. Solid Phase Synthesis (Nobel Lecture). *Angewandte Chemie International Edition in English*, 24(10):799–810, October 1985.
- [44] J. Wintterlin, J. Wiechers, H. Brune, T. Gritsch, H. Höfer, and R. J. Behm. Atomic-Resolution Imaging of Close-Packed Metal Surfaces by Scanning Tunneling Microscopy. *Physical Review Letters*, 62(1):59–62, January 1989.
- [45] Francesca Moresco, Gerhard Meyer, Karl-Heinz Rieder, Hao Tang, André Gourdon, and Christian Joachim. Conformational Changes of Single Molecules Induced by Scanning Tunneling Microscopy Manipulation: A Route to Molecular Switching. *Physical Review Letters*, 86(4):672–675, January 2001.

- [46] Jascha Repp, Gerhard Meyer, Sladjana M. Stojković, André Gourdon, and Christian Joachim. Molecules on insulating films: Scanning-tunneling microscopy imaging of individual molecular orbitals. *Physical Review Letters*, 94(January):1–4, January 2005.
- [47] Jorge Lobo-Checa, Manfred Matena, Kathrin Müller, Jan Hugo Dil, Fabian Meier, Lutz H Gade, Thomas A Jung, and Meike Stöhr. Band formation from coupled quantum dots formed by a nanoporous network on a copper surface. *Science (New York, N.Y.)*, 325(5938):300–3, July 2009.
- [48] F.M. Leibsle, S.S. Dhesi, S.D. Barrett, and A.W. Robinson. STM observations of Cu(100) c(2 × 2)N surfaces: evidence for attractive interactions and an incommensurate c(2 × 2) structure. *Surface Science*, 317(3):309–320, October 1994.
- [49] Gordon Rinke, Stephan Rauschenbach, Ludger Harnau, Alyazan Albarghash, Matthias Pauly, and Klaus Kern. Active conformation control of unfolded proteins by hyperthermal collision with a metal surface. *Nano letters*, 14(10):5609–15, October 2014.
- [50] Tomihiro Hashizume, K. Motai, X. D. Wang, H. Shinohara, Y. Saito, Y. Maruyama, K. Ohno, Y. Kawazoe, Y. Nishina, H. W. Pickering, Y. Kuk, and T. Sakurai. Intramolecular structures of C₆₀ molecules adsorbed on the Cu(111)-(1 × 1) surface. *Physical Review Letters*, 71(18):2959–2962, November 1993.
- [51] P.M. Echenique and J.B. Pendry. Theory of image states at metal surfaces. *Progress in Surface Science*, 32(2):111–159, January 1989.
- [52] RONALD W. GURNEY and EDW. U. CONDON. Wave Mechanics and Radioactive Disintegration. *Nature*, 122(3073):439–439, September 1928.
- [53] Rabi Majumdar. *QUANTUM MECHANICS IN PHYSICS AND CHEMISTRY WITH APPLICATIONS TO BIOLOGY*. Phi Learning Pvt. Ltd., 2014.
- [54] D. A. Muller, T. Sorsch, S. Moccio, F. H. Baumann, K. Evans-Lutterodt, and G. Timp. The electronic structure at the atomic scale of ultrathin gate oxides. *Nature*, 399(6738):758–761, June 1999.
- [55] J. Geerk, X. X. Xi, and G. Linker. Electron tunneling into thin films of YBa₂Cu₃O₇. *Zeitschrift für Physik B Condensed Matter*, 73(3):329–336, September 1988.
- [56] G. Binnig, H. Rohrer, Ch. Gerber, and E. Weibel. (111) facets as the origin of reconstructed Au(110) surfaces. *Surface Science Letters*, 131(1):L379–L384, August 1983.
- [57] Gerd Binnig and Heinrich Rohrer. Scanning Tunneling Microscopy—from Birth to Adolescence(Nobel Lecture). *Angewandte Chemie International Edition in English*, 26(7):606–614, July 1987.
- [58] Ernst Ruska. The Development of the Electron Microscope and of Electron Microscopy(Nobel Lecture). *Angewandte Chemie International Edition in English*, 26(7):595–605, July 1987.

Bibliography

- [59] Ernst Meyer, Hans Josef Hug, and Roland Bennewitz. *Scanning Probe Microscopy*. Advanced Texts in Physics. Springer Berlin Heidelberg, Berlin, Heidelberg, 2004.
- [60] J. Tersoff and D. R. Hamann. Theory of the scanning tunneling microscope. *Physical Review B*, 31(2):805–813, January 1985.
- [61] M F Crommie, C P Lutz, and D M Eigler. Confinement of electrons to quantum corrals on a metal surface. *Science (New York, N.Y.)*, 262(5131):218–20, October 1993.
- [62] C. Domke, Ph. Ebert, M. Heinrich, and K. Urban. Microscopic identification of the compensation mechanisms in Si-doped GaAs. *Physical Review B*, 54(15):10288–10291, October 1996.
- [63] L. Bartels, G. Meyer, and K.-H. Rieder. Controlled vertical manipulation of single CO molecules with the scanning tunneling microscope: A route to chemical contrast. *Applied Physics Letters*, 71(2):213, July 1997.
- [64] P. Wahl, M. A. Schneider, L. Diekhöner, R. Vogelgesang, and K. Kern. Quantum Coherence of Image-Potential States. *Physical Review Letters*, 91(10):106802, September 2003.
- [65] J. Segner, C.T. Campbell, G. Doyen, and G. Ertl. Catalytic oxidation of CO on Pt(111): The influence of surface defects and composition on the reaction dynamics. *Surface Science*, 138(2-3):505–523, March 1984.
- [66] J. Bardeen. Tunnelling from a Many-Particle Point of View. *Physical Review Letters*, 6(2):57–59, January 1961.
- [67] Bert Voigtländer. *Scanning Probe Microscopy*. NanoScience and Technology. Springer Berlin Heidelberg, Berlin, Heidelberg, 2015.
- [68] A J Heinrich, C P Lutz, J A Gupta, and D M Eigler. Molecule cascades. *Science (New York, N.Y.)*, 298(5597):1381–7, November 2002.
- [69] SPECS. SPECS STM 150 Aarhus HT, 2015.
- [70] Christoph Grosse, Markus Etzkorn, Klaus Kuhnke, Sebastian Loth, and Klaus Kern. Quantitative mapping of fast voltage pulses in tunnel junctions by plasmonic luminescence. *Applied Physics Letters*, 103(18):183108, October 2013.
- [71] Jean-Paul Collin, Isabelle M. Dixon, Jean-Pierre Sauvage, J. A. Gareth Williams, Francesco Barigelli, and Lucia Flamigni. Synthesis and Photophysical Properties of Iridium(III) Bisterpyridine and Its Homologues. *Journal of the American Chemical Society*, 121(21):5009–5016, June 1999.
- [72] John B Fenn. Electrospray wings for molecular elephants (Nobel lecture). *Angewandte Chemie (International ed. in English)*, 42(33):3871–94, August 2003.

- [73] Andreas Premstaller, Herbert Oberacher, Wolfgang Walcher, Anna Maria Timperio, Lello Zolla, Jean-Pierre Chervet, Nukhet Cavusoglu, Alain van Dorsselaer, and Christian G. Huber. High Performance Liquid Chromatography. *Analytical Chemistry*, 73(11):2390–2396, June 2001.
- [74] J. Fenn, M Mann, C. Meng, S. Wong, and C. Whitehouse. Electrospray ionization for mass spectrometry of large biomolecules. *Science*, 246(4926):64–71, October 1989.
- [75] Christian R. Ast, Daniela Pacilé, Luca Moreschini, Mihaela C. Falub, Marco Papagno, Klaus Kern, Marco Grioni, Jürgen Henk, Arthur Ernst, Sergey Ostanin, and Patrick Bruno. Spin-orbit split two-dimensional electron gas with tunable Rashba and Fermi energy. *Physical Review B - Condensed Matter and Materials Physics*, 77:3–6, 2008.
- [76] Frederick Terman. *Radio engineers' handbook*. McGraw-Hill Book Co., New York ;London, 1943.
- [77] P. Wissmann. Thin Metal Films and Gas Chemisorption, 1987.
- [78] Lucia Vitali, Giacomo Levita, Robin Ohmann, Alessio Comisso, Alessandro De Vita, and Klaus Kern. Portrait of the potential barrier at metal-organic nanocontacts. *Nature materials*, 9(4):320–323, 2010.
- [79] Sushobhan Joshi, Felix Bischoff, Ralph Koitz, David Ecija, Knud Seufert, Ari Paavo Seitsonen, Jürg Hutter, Katharina Diller, José I Urgel, Hermann Sachdev, Johannes V Barth, and Willi Auwärter. Control of molecular organization and energy level alignment by an electronically nanopatterned boron nitride template. *ACS nano*, 8(1):430–42, January 2014.
- [80] Hans-Christoph Ploigt, Christophe Brun, Marina Pivetta, François Patthey, and Wolf-Dieter Schneider. Local work function changes determined by field emission resonances. *Physical Review B*, 76(19):195404, November 2007.
- [81] Sushobhan Joshi, David Ecija, Ralph Koitz, Marcella Iannuzzi, A.P Seitsonen, J Hutter, H Sachdev, S Vijayaraghavan, Bischoff F, K Seufert, J.V Barth, and Auwarter W. Boron Nitride on Cu (111): An Electronically Corrugated Monolayer. *Nano Letters*, 12(11):5821–5828, 2012.
- [82] Charles Kittel. *Introduction to solid state physics*. New York, Wiley, 1971.
- [83] A. W. Dweydari and C. H. B. Mee. Work function measurements on (100) and (110) surfaces of silver. *Physica Status Solidi (a)*, 27(1):223–230, January 1975.
- [84] N. Lang and W. Kohn. Theory of Metal Surfaces: Work Function. *Physical Review B*, 3(4):1215–1223, February 1971.
- [85] P. Ruffieux, K. Ait-Mansour, A. Bendounan, R. Fasel, L. Patthey, P. Gröning, and O. Gröning. Mapping the Electronic Surface Potential of Nanostructured Surfaces. *Physical Review Letters*, 102(8):086807, February 2009.

Bibliography

- [86] B. Borca, S. Barja, M. Garnica, D. Sánchez-Portal, V. M. Silkin, E. V. Chulkov, C. F. Hermanns, J. J. Hinarejos, a. L. Vázquez De Parga, a. Arnau, P. M. Echenique, R. Miranda, B. Borca, S. Barja, M. Garnica, and D Sa. Potential energy landscape for hot electrons in periodically nanostructured graphene. *Physical Review Letters*, 105(3):1–4, July 2010.
- [87] M. R. C. Hunt, S. Modesti, P. Rudolf, and R. E. Palmer. Charge transfer and structure in C 60 adsorption on metal surfaces. *Physical Review B*, 51(15):10039–10047, April 1995.
- [88] B. Borca, S. Barja, M. Garnica, D. Sánchez-Portal, V. M. Silkin, E. V. Chulkov, C. F. Hermanns, J. J. Hinarejos, A. L. Vázquez de Parga, A. Arnau, P. M. Echenique, and R. Miranda. Potential Energy Landscape for Hot Electrons in Periodically Nanostructured Graphene. *Physical Review Letters*, 105(3):036804, July 2010.
- [89] Toshio Sakurai, T.Sakurai and Yousuke Watanabe. *Advances in Scanning Probe Microscopy*, volume 2 of *Advances in Materials Research*. Springer Berlin Heidelberg, Berlin, Heidelberg, 2000.
- [90] P. M. Echenique, F. Flores, and F. Sols. Lifetime of Image Surface States. *Physical Review Letters*, 55(21):2348–2350, November 1985.
- [91] P.M. Echenique and M.E. Uranga. Image potential states at surfaces. *Surface Science*, 247(2-3):125–132, May 1991.
- [92] K. Schubert, A. Damm, S. V. Ereameev, M. Marks, M. Shibuta, W. Berthold, J. Güdde, A. G. Borisov, S. S. Tsirkin, E. V. Chulkov, and U. Höfer. Momentum-resolved electron dynamics of image-potential states on Cu and Ag surfaces. *Physical Review B*, 85(20):205431, May 2012.
- [93] N. Garcia, B. Reihl, K. H. Frank, and A. R. Williams. Image States: Binding Energies, Effective Masses, and Surface Corrugation. *Physical Review Letters*, 54(6):591–594, February 1985.
- [94] V. Dose, W. Altmann, A. Goldmann, U. Kolac, and J. Rogozik. Image-Potential States Observed by Inverse Photoemission. *Physical Review Letters*, 52(21):1919–1921, May 1984.
- [95] W. Berthold, U. Höfer, P. Feulner, E. V. Chulkov, V. M. Silkin, and P. M. Echenique. Momentum-Resolved Lifetimes of Image-Potential States on Cu(100). *Physical Review Letters*, 88(5):056805, January 2002.
- [96] S. Crampin. Lifetimes of Stark-Shifted Image States. *Physical Review Letters*, 95(4):046801, July 2005.
- [97] R. Fischer, Th. Fauster, and W. Steinmann. Three-dimensional localization of electrons on Ag islands. *Physical Review B*, 48(20):15496–15499, November 1993.

-
- [98] J. I. Pascual, C. Corriol, G. Ceballos, I. Aldazabal, H.-P. Rust, K. Horn, J. M. Pitarke, P. M. Echenique, and A. Arnau. Role of the electric field in surface electron dynamics above the vacuum level. *Physical Review B*, 75(16):165326, April 2007.
- [99] J. Kroger, L. Limot, H. Jensen, R. Berndt, and P. Johansson. Stark effect in Au(111) and Cu(111) surface states. *Physical Review B - Condensed Matter and Materials Physics*, 70:1–4, 2004.
- [100] A. G. Borisov, T. Hakala, M. J. Puska, V. M. Silkin, N. Zabala, E. V. Chulkov, and P. M. Echenique. Image potential states of supported metallic nanoislands. *Physical Review B*, 76(12):121402, September 2007.
- [101] Fabian Craes, Sven Runte, Jürgen Klinkhammer, Marko Kralj, Thomas Michely, and Carsten Busse. Mapping Image Potential States on Graphene Quantum Dots. *Physical Review Letters*, 111(5):056804, July 2013.
- [102] K. Schouteden and C. Van Haesendonck. Lateral Quantization of Two-Dimensional Electron States by Embedded Ag Nanocrystals. *Physical Review Letters*, 108(7):076806, February 2012.
- [103] S. Stepanow, A. Mugarza, G. Ceballos, P. Gambardella, I. Aldazabal, A. G. Borisov, and A. Arnau. Localization, splitting, and mixing of field emission resonances induced by alkali metal clusters on Cu(100). *Physical Review B*, 83(11):115101, March 2011.
- [104] D Niesner, Th Fauster, J I Dadap, N Zaki, K R Knox, P Yeh, R Bhandari, R M Osgood, and M Petrovi. Trapping surface electrons on graphene layers and islands. *Physical Review B*, 081402:1–5, 2012.
- [105] D. Velic, A. Hotzel, M. Wolf, and G. Ertl. Electronic states of the C[sub 6]H[sub 6]/Cu{111} system: Energetics, femtosecond dynamics, and adsorption morphology. *The Journal of Chemical Physics*, 109(20):9155, November 1998.
- [106] Gregory Dutton, Jingzhi Pu, Donald G. Truhlar, and X.-Y. Zhu. Lateral confinement of image electron wave function by an interfacial dipole lattice. *The Journal of Chemical Physics*, 118(10):4337, February 2003.
- [107] Emile D. L. Rienks, Niklas Nilius, Hans-Peter Rust, and Hans-Joachim Freund. Surface potential of a polar oxide film: FeO on Pt(111). *Physical Review B*, 71(24):241404, June 2005.
- [108] Bo Wang, Marco Caffio, Catherine Bromley, Herbert Früchtl, and Renald Schaub. Coupling epitaxy, chemical bonding, and work function at the local scale in transition metal-supported graphene. *ACS nano*, 4(10):5773–82, October 2010.
- [109] N. Armbrust, J. GÜdde, P. Jakob, and U. Höfer. Time-Resolved Two-Photon Photoemission of Unoccupied Electronic States of Periodically Rippled Graphene on Ru(0001). *Physical Review Letters*, 108(5):056801, January 2012.

Bibliography

- [110] Ryota Yamamoto, Takashi Yamada, Masataka Taguchi, Keisuke Miyakubo, Hiroyuki S Kato, and Toshiaki Munakata. Dispersions of image potential states on surfaces of clean graphite and lead phthalocyanine film. *Physical chemistry chemical physics : PCCP*, 14(27):9601–5, July 2012.
- [111] Fabian Schulz, Robert Drost, Sampsa K. Hämäläinen, Thomas Demonchaux, Ari P. Seitsonen, and Peter Liljeroth. Epitaxial hexagonal boron nitride on Ir(111): A work function template. *Physical Review B*, 89(23):235429, June 2014.
- [112] Benjamin W. Caplins, Alex J. Shearer, David E. Suich, Eric A. Muller, and Charles B. Harris. Measuring the electronic corrugation at the metal/organic interface. *Physical Review B*, 89(15):155422, April 2014.
- [113] M. Roth, M. Pickel, J. Wang, M. Weinelt, and Th Fauster. Image potential states on stepped Cu(100) surfaces. *Applied Physics B: Lasers and Optics*, 74(7-8):661–664, March 2002.
- [114] Eric A. Muller, James E. Johns, Benjamin W. Caplins, and Charles B. Harris. Quantum confinement and anisotropy in thin-film molecular semiconductors. *Physical Review B*, 83(16):165422, April 2011.
- [115] Ralph H. Fowler. *Statistical Mechanics: The Theory of the Properties of Matter in Equilibrium*. Statistical Mechanics: The Theory of the Properties of Matter in Equilibrium, 1966.
- [116] M. Nonnenmacher, M. P. O’Boyle, and H. K. Wickramasinghe. Kelvin probe force microscopy. *Applied Physics Letters*, 58(25):2921, June 1991.
- [117] K S Novoselov, A K Geim, S V Morozov, D Jiang, Y Zhang, S V Dubonos, I V Grigorieva, and A A Firsov. Electric field effect in atomically thin carbon films. *Science (New York, N.Y.)*, 306(5696):666–9, October 2004.
- [118] Jian-Hao Chen, Chaun Jang, Shudong Xiao, Masa Ishigami, and Michael S Fuhrer. Intrinsic and extrinsic performance limits of graphene devices on SiO₂. *Nature nanotechnology*, 3(4):206–9, April 2008.
- [119] Changgu Lee, Xiaoding Wei, Jeffrey W Kysar, and James Hone. Measurement of the elastic properties and intrinsic strength of monolayer graphene. *Science (New York, N.Y.)*, 321(5887):385–8, July 2008.
- [120] F. Bonaccorso, Z. Sun, T. Hasan, and A. C. Ferrari. Graphene photonics and optoelectronics. *Nature Photonics*, 4(9):611–622, August 2010.
- [121] Chuhei Oshima and Ayato Nagashima. Ultra-thin epitaxial films of graphite and hexagonal boron nitride on solid surfaces. *Journal of Physics: Condensed Matter*, 9(1):1–20, January 1997.

- [122] Oded Hod. Graphite and Hexagonal Boron-Nitride have the Same Interlayer Distance. Why? *Journal of Chemical Theory and Computation*, 8(4):1360–1369, April 2012.
- [123] Yang Xu, Zhendong Guo, Huabin Chen, You Yuan, Jiechao Lou, Xiao Lin, Haiyuan Gao, Hongsheng Chen, and Bin Yu. In-plane and tunneling pressure sensors based on graphene/hexagonal boron nitride heterostructures. *Applied Physics Letters*, 99(13):133109, September 2011.
- [124] L Britnell, R V Gorbachev, R Jalil, B D Belle, F Schedin, A Mishchenko, T Georgiou, M I Katsnelson, L Eaves, S V Morozov, N M R Peres, J Leist, A K Geim, K S Novoselov, and L A Ponomarenko. Field-effect tunneling transistor based on vertical graphene heterostructures. *Science (New York, N.Y.)*, 335(6071):947–50, February 2012.
- [125] C R Dean, L Wang, P Maher, C Forsythe, F Ghahari, Y Gao, J Katoch, M Ishigami, P Moon, M Koshino, T Taniguchi, K Watanabe, K L Shepard, J Hone, and P Kim. Hofstadter's butterfly and the fractal quantum Hall effect in moiré superlattices. *Nature*, 497(7451):598–602, May 2013.
- [126] L A Ponomarenko, R V Gorbachev, G L Yu, D C Elias, R Jalil, A A Patel, A Mishchenko, A S Mayorov, C R Woods, J R Wallbank, M Mucha-Kruczynski, B A Piot, M Potemski, I V Grigorieva, K S Novoselov, F Guinea, V I Fal'ko, and A K Geim. Cloning of Dirac fermions in graphene superlattices. *Nature*, 497(7451):594–7, May 2013.
- [127] A K Geim and I V Grigorieva. Van der Waals heterostructures. *Nature*, 499(7459):419–25, July 2013.
- [128] C R Dean, A F Young, I Meric, C Lee, L Wang, S Sorgenfrei, K Watanabe, T Taniguchi, P Kim, K L Shepard, and J Hone. Boron nitride substrates for high-quality graphene electronics. *Nature nanotechnology*, 5(10):722–6, October 2010.
- [129] Robert T. Paine and Chaitanya K. Narula. Synthetic routes to boron nitride. *Chemical Reviews*, 90(1):73–91, January 1990.
- [130] A. Nagashima, N. Tejima, Y. Gamou, T. Kawai, and C. Oshima. Electronic dispersion relations of monolayer hexagonal boron nitride formed on the Ni(111) surface. *Physical Review B*, 51(7):4606–4613, February 1995.
- [131] Fabrizio Orlando, Rosanna Larciprete, Paolo Lacovig, Ilan Boscarato, Alessandro Baraldi, and Silvano Lizzit. Epitaxial Growth of Hexagonal Boron Nitride on Ir(111). *The Journal of Physical Chemistry C*, 116(1):157–164, January 2012.
- [132] A. Nagashima, N. Tejima, Y. Gamou, T. Kawai, and C. Oshima. Electronic states of monolayer hexagonal boron nitride formed on the metal surfaces. *Surface Science*, 357-358:307–311, June 1996.
- [133] Frank Müller, Stefan Hübner, Hermann Sachdev, Robert Laskowski, Peter Blaha, and Karlheinz Schwarz. Epitaxial growth of hexagonal boron nitride on Ag(111). *Physical Review B*, 82(11):113406, September 2010.

Bibliography

- [134] A.B. Preobrajenski, A.S. Vinogradov, and N. Martensson. Monolayer of h-BN chemisorbed on Cu(111) and Ni(111): The role of the transition metal 3d states. *Surface Science*, 582(1-3):21–30, May 2005.
- [135] Martina Corso, Willi Auwärter, Matthias Muntwiler, Anna Tamai, Thomas Greber, and Jürg Osterwalder. Boron nitride nanomesh. *Science (New York, N.Y.)*, 303(5655):217–20, January 2004.
- [136] Simon Berner, Martina Corso, Roland Widmer, Oliver Groening, Robert Laskowski, Peter Blaha, Karlheinz Schwarz, Andrii Goriachko, Herbert Over, Stefan Gsell, Matthias Schreck, Hermann Sachdev, Thomas Greber, and Jürg Osterwalder. Boron nitride nanomesh: functionality from a corrugated monolayer. *Angewandte Chemie (International ed. in English)*, 46(27):5115–9, January 2007.
- [137] Iván Brihuega, Christian Heinrich Michaelis, Jian Zhang, Sangita Bose, Violetta Sessi, Jan Honolka, M. Alexander Schneider, Axel Enders, and Klaus Kern. Electronic decoupling and templating of Co nanocluster arrays on the boron nitride nanomesh. *Surface Science*, 602(14):L95–L99, July 2008.
- [138] Peter Atkins and Julio de Paula. *Elements of Physical Chemistry*. OUP Oxford, 2012.
- [139] Yongqiang Xue, Supriyo Datta, and Mark A. Ratner. Charge transfer and “band lineup” in molecular electronic devices: A chemical and numerical interpretation. *The Journal of Chemical Physics*, 115(9):4292, September 2001.
- [140] David Jeffery Griffiths. *Introduction to Quantum Mechanics*. Pearson Prentice Hall; 2nd edition (April 10, 2004), 2005.
- [141] S Koch, M Langer, S Kawai, E Meyer, and Th Glatzel. Contrast inversion of the h-BN nanomesh investigated by nc-AFM and Kelvin probe force microscopy. *Journal of physics. Condensed matter : an Institute of Physics journal*, 24(31):314212, August 2012.
- [142] Matthias Muntwiler, Matthias Hengsberger, Andrei Dolocan, Hansjorg Neff, Thomas Greber, and Jurg Osterwalder. Energetics and dynamics of unoccupied electronic states. *Physical Review B*, 75(7):075407, February 2007.
- [143] Sushobhan Joshi, David Eciija, Ralph Koitz, Marcella Iannuzzi, Ari P Seitsonen, Jürg Hutter, Hermann Sachdev, Saranyan Vijayaraghavan, Felix Bischoff, Knud Seufert, Johannes V Barth, and Willi Auwärter. Boron nitride on Cu(111): an electronically corrugated monolayer. *Nano letters*, 12(11):5821–8, November 2012.
- [144] Ralph Koitz, Ari P Seitsonen, Marcella Iannuzzi, and Jürg Hutter. Structural and electronic properties of a large-scale Moiré pattern of hexagonal boron nitride on Cu(111) studied with density functional theory. *Nanoscale*, 5(12):5589–95, June 2013.
- [145] Marina Pivetta, François Patthey, Massimiliano Stengel, Alfonso Baldereschi, and Wolf-Dieter Schneider. Local work function Moiré pattern on ultrathin ionic films: NaCl on Ag(100). *Physical Review B*, 72(11):115404, September 2005.

-
- [146] R.L. Lingle, N.-H. Ge, R.E. Jordan, J.D. McNeill, and C.B. Harris. Femtosecond studies of electron tunneling at metal-dielectric interfaces. *Chemical Physics*, 205(1-2):191–203, April 1996.
- [147] Tobias Herden. Combined Scanning Tunneling and Atomic Force Microscopy and Spectroscopy on Molecular Nanostructures, 2014.
- [148] K. Oura, M. Katayama, A. V. Zotov, V. G. Lifshits, and A. A. Saranin. *Surface Science*. Advanced Texts in Physics. Springer Berlin Heidelberg, Berlin, Heidelberg, 2003.
- [149] N Ooi, A Rairkar, L Lindsley, and J B Adams. Electronic structure and bonding in hexagonal boron nitride. *Journal of Physics: Condensed Matter*, 18(1):97–115, January 2006.
- [150] Huanyao Cun, Marcella Iannuzzi, Adrian Hemmi, Jürg Osterwalder, and Thomas Greber. Two-nanometer voids in single-layer hexagonal boron nitride: formation via the "can-opener" effect and annihilation by self-healing. *ACS nano*, 8(7):7423–31, July 2014.
- [151] Jannik C Meyer, Andrey Chuvilin, Gerardo Algara-Siller, Johannes Biskupek, and Ute Kaiser. Selective sputtering and atomic resolution imaging of atomically thin boron nitride membranes. *Nano letters*, 9(7):2683–9, July 2009.
- [152] Federico Rosei, Michael Schunack, Yoshitaka Naitoh, Ping Jiang, André Gourdon, Erik Laegsgaard, Ivan Stensgaard, Christian Joachim, and Flemming Besenbacher. Properties of large organic molecules on metal surfaces. *Progress in Surface Science*, 71(5-8):95–146, June 2003.
- [153] P. H. Lippel, R. J. Wilson, M. D. Miller, Ch. Wöll, and S. Chiang. High-Resolution Imaging of Copper-Phthalocyanine by Scanning-Tunneling Microscopy. *Physical Review Letters*, 62(2):171–174, January 1989.
- [154] Joe Otsuki. STM studies on porphyrins. *Coordination Chemistry Reviews*, 254(19-20):2311–2341, October 2010.
- [155] Hiroyuki Tanaka and Tomoji Kawai. Partial sequencing of a single DNA molecule with a scanning tunnelling microscope. *Nature nanotechnology*, 4(8):518–22, August 2009.
- [156] Leo Gross, Nikolaj Moll, Fabian Mohn, Alessandro Curioni, Gerhard Meyer, Felix Hanke, and Mats Persson. High-Resolution Molecular Orbital Imaging Using a p -Wave STM Tip. *Physical Review Letters*, 107(8):086101, August 2011.
- [157] Richard A. Preston. Age-Race Subgroup Compared With Renin Profile as Predictors of Blood Pressure Response to Antihypertensive Therapy. *JAMA*, 280(13):1168, October 1998.
- [158] N. Basso and N. A. Terragno. History About the Discovery of the Renin-Angiotensin System. *Hypertension*, 38(6):1246–1249, December 2001.

Bibliography

- [159] Robert S.; Ingle Dweight J. Harris. *VITAMINS AND HORMONES, Band 18*. Academic Press Inc., 1961.
- [160] S. Rauschenbach. Private communication. 2015.
- [161] Robin Ohmann, Giacomo Levita, Lucia Vitali, Alessandro De Vita, and Klaus Kern. Influence of subsurface layers on the adsorption of large organic molecules on close-packed metal surfaces. *ACS Nano*, 5(2):1360–1365, February 2011.
- [162] Prokop Hapala, Georgy Kichin, Christian Wagner, F Stefan Tautz, Ruslan Temirov, and Pavel Jelínek. Mechanism of high-resolution STM/AFM imaging with functionalized tips. *Physical Review B*, 90(8):085421, August 2014.
- [163] G Heimel, S Duhm, I Salzmann, A Gerlach, A Strozecka, J Niederhausen, C Bürker, T Hosokai, I Fernandez-Torrente, G Schulze, S Winkler, A Wilke, R Schlesinger, J Frisch, B Bröker, A Vollmer, B Detlefs, J Pflaum, S Kera, K J Franke, N Ueno, J I Pascual, F Schreiber, and N Koch. Charged and metallic molecular monolayers through surface-induced aromatic stabilization. *Nature chemistry*, 5(3):187–94, March 2013.
- [164] Roald Hoffmann. A chemical and theoretical way to look at bonding on surfaces. *Reviews of Modern Physics*, 60(3):601–628, July 1988.
- [165] Hasmik Harutyunyan, Martin Callsen, Tobias Allmers, Vasile Caciuc, Stefan Blügel, Nicolae Atodiresei, and Daniel Wegner. Hybridisation at the organic-metal interface: a surface-scientific analogue of Hückel’s rule? *Chemical communications (Cambridge, England)*, 49(53):5993–5, July 2013.
- [166] Theresa Lutz, Christoph Grosse, Christian Dette, Alexander Kabakchiev, Frank Schramm, Mario Ruben, Rico Gutzler, Klaus Kuhnke, Uta Schlickum, and Klaus Kern. Molecular orbital gates for plasmon excitation. *Nano letters*, 13(6):2846–50, June 2013.
- [167] S A Burke, J M Topple, and P Grütter. Molecular dewetting on insulators. *Journal of physics. Condensed matter : an Institute of Physics journal*, 21(42):423101, October 2009.
- [168] Jeffrey M Mativetsky, Sarah A Burke, Shawn Fostner, and Peter Grutter. Templated growth of 3,4,9,10-perylene-tetracarboxylic dianhydride molecules on a nanostructured insulator. *Nanotechnology*, 18(10):105303, March 2007.
- [169] Wolfgang Krenner, Dirk Kühne, Florian Klappenberger, and Johannes V Barth. Assessment of scanning tunneling spectroscopy modes inspecting electron confinement in surface-confined supramolecular networks. *Scientific reports*, 3(111):1454, January 2013.
- [170] W. H. Soe, C. Manzano, a. De Sarkar, N. Chandrasekhar, and C. Joachim. Direct observation of molecular orbitals of pentacene physisorbed on Au(111) by scanning tunneling microscope. *Physical Review Letters*, 102(May):100–103, 2009.

- [171] K. J. Franke, G. Schulze, N. Henningsen, I. Fernández-Torrente, J. I. Pascual, S. Zarwell, K. Rück-Braun, M. Cobian, and N. Lorente. Reducing the Molecule-Substrate Coupling in C 60 -Based Nanostructures by Molecular Interactions. *Physical Review Letters*, 100(3):036807, January 2008.
- [172] B. C. Stipe. Single-Molecule Vibrational Spectroscopy and Microscopy. *Science*, 280(5370):1732–1735, June 1998.
- [173] Vossman. Cytochrome C, 2011.
- [174] Geoffrey Moore and Graham W. Pettigrew. *Cytochromes c: Evolutionary, Structural and Physicochemical Aspects*. Springer-Verlag Berlin Heidelberg, 2012.
- [175] Douglas R. Green. *Means to an End: Apoptosis and Other Cell Death Mechanisms*. Cold Spring Harbor Laboratory Press, 2011.
- [176] Yutaka Kuroda, Shun-ichi Kidokoro, and Akiyoshi Wada. Thermodynamic characterization of cytochrome c at low pH. *Journal of Molecular Biology*, 223(4):1139–1153, February 1992.
- [177] M. Wuttig, R. Franchy, and H. Ibach. The Rayleigh phonon dispersion curve on Cu(100) in the direction. *Solid State Communications*, 57(6):445–447, February 1986.
- [178] J.T. Hoeft, M. Polcik, M. Kittel, R. Terborg, R.L. Toomes, J.-H. Kang, and D.P. Woodruff. Photoelectron diffraction structure determination of Cu(100)c(2×2)-N. *Surface Science*, 492(1-2):1–10, October 2001.
- [179] Martin Aeschlimann, Michael Bauer, Daniela Bayer, Tobias Brixner, F. Javier García De Abajo, Walter Pfeiffer, Martin Rohmer, Christian Spindler, and Felix Steeb. Adaptive sub-wavelength control of nanoscopic fields. *Conference on Quantum Electronics and Laser Science (QELS) - Technical Digest Series*, 446(7133):301–4, March 2007.
- [180] T.E Wofford, S.M York, and F.M Leibsle. Properly interpreting scanning tunneling microscopy images: the Cu()-c(2×2)N surface revisited. *Surface Science*, 522(1-3):47–54, January 2003.
- [181] S.M. Driver and D.P. Woodruff. Comment on “Properly interpreting scanning tunneling microscopy images: the Cu(100)-c(2×2)N surface revisited” by T.E. Wofford, S.M. York and F.M. Leibsle [Surf. Sci. 522 (2003) 47]. *Surface Science*, 539(1-3):182–185, August 2003.
- [182] T. Choi, C. D. Ruggiero, and J. A. Gupta. Incommensurability and atomic structure of c (2 × 2) N / Cu (100) : A scanning tunneling microscopy study. *Physical Review B*, 78(3):035430, July 2008.

Bibliography

- [183] Cyrus F Hirjibehedin, Chiung-Yuan Lin, Alexander F Otte, Markus Ternes, Christopher P Lutz, Barbara A Jones, and Andreas J Heinrich. Large magnetic anisotropy of a single atomic spin embedded in a surface molecular network. *Science (New York, N.Y.)*, 317(5842):1199–203, August 2007.
- [184] Shiyong Wang, Weihua Wang, Yuning Hong, Ben Zhong Tang, and Nian Lin. Vibronic state assisted resonant transport in molecules strongly anchored at an electrode. *Physical Review B*, 83(11):115431, March 2011.
- [185] Z Bu, J Cook, and D J Callaway. Dynamic regimes and correlated structural dynamics in native and denatured alpha-lactalbumin. *Journal of molecular biology*, 312(4):865–73, September 2001.
- [186] Robin L. McCarley, David J. Dunaway, and Robert J. Willicut. Mobility of the alkanethiol-gold (111) interface studied by scanning probe microscopy. *Langmuir*, 9(11):2775–2777, November 1993.
- [187] Joseph A. Gerstner, Jeffrey A. Bell, and Steven M. Cramer. Gibbs free energy of adsorption for biomolecules in ion-exchange systems. *Biophysical Chemistry*, 52(2):97–106, October 1994.
- [188] Michael Rubinstein and Ralph H. Colby. *Polymer Physics*. Oxford University Press, 2003.
- [189] Zheng Ouyang, Zoltán Takáts, Thomas A Blake, Bogdan Gologan, Andy J Guymon, Justin M Wiseman, Justin C Oliver, V Jo Davisson, and R Graham Cooks. Preparing protein microarrays by soft-landing of mass-selected ions. *Science (New York, N.Y.)*, 301(5638):1351–4, September 2003.
- [190] C. D. Ruggiero, T. Choi, and J. A. Gupta. Tunneling spectroscopy of ultrathin insulating films: CuN on Cu(100). *Applied Physics Letters*, 91(25):253106, December 2007.
- [191] J. A. Appelbaum and D. R. Hamann. Variational Calculation of the Image Potential near a Metal Surface. *Physical Review B*, 6(4):1122–1130, August 1972.
- [192] Franz J. Giessibl. Advances in atomic force microscopy. *Reviews of Modern Physics*, 75(3):949–983, July 2003.
- [193] Leo Gross, Fabian Mohn, Nikolaj Moll, Peter Liljeroth, and Gerhard Meyer. The chemical structure of a molecule resolved by atomic force microscopy. *Science (New York, N.Y.)*, 325(5944):1110–4, August 2009.
- [194] Klaus Duncker, Mario Kiel, and Wolf Widdra. Surface Science Momentum-resolved lifetimes of image-potential states on Ag (001). *Surface Science*, 606(21-22):L87–L90, 2012.
- [195] Liwei Liu, Kai Yang, Yuhang Jiang, Boqun Song, Wende Xiao, Linfei Li, Haitao Zhou, Yeliang Wang, Shixuan Du, Min Ouyang, Werner a Hofer, Antonio H Castro Neto, and

- Hong-Jun Gao. Reversible single spin control of individual magnetic molecule by hydrogen atom adsorption. *Scientific reports*, 3(111):1210, 2013.
- [196] C. Ye, Tobin J. Marks, J. Yang, and G. K. Wong. Synthesis of molecular arrays with nonlinear optical properties: second-harmonic generation by covalently functionalized glassy polymers. *Macromolecules*, 20(9):2322–2324, September 1987.
- [197] Chris A. Mack. Fifty Years of Moore’s Law. *IEEE Transactions on Semiconductor Manufacturing*, 24(2):202–207, May 2011.
- [198] Thomas A Blake, Zheng Ouyang, Justin M Wiseman, Zoltán Takáts, Andrew J Guymon, Sameer Kothari, and R Graham Cooks. Preparative linear ion trap mass spectrometer for separation and collection of purified proteins and peptides in arrays using ion soft landing. *Analytical chemistry*, 76(21):6293–305, November 2004.
- [199] Chr Hamann, R Woltmann, I-Po Hong, N Hauptmann, S Karan, and R Berndt. Ultrahigh vacuum deposition of organic molecules by electrospray ionization. *The Review of scientific instruments*, 82(3):033903, March 2011.

Curriculum Vitae

Name Daniel Pablo Rosenblatt

Date of Birth 23.05.1981

Nationality Israel / Uruguay

2015 Phd thesis: "Construction of a low temperature STM and studies of large molecular systems".

2011 - 2015 Research Assistant in the Prof. Dr. Klaus Kern's group at Max-Planck-Institute for Solid State Research, Stuttgart, Germany.

2009 M.Sc. thesis: "Extraordinary Hall effect measurements in Co/Pd thin films".

2006 – 2009 M.Sc. in physics, supervised by Prof. Alexander Gerber, Tel-Aviv University (Israel).

2002 – 2006 B.Sc. in physics and Computer science (with honors) at Tel-Aviv University (Israel).